HAC REF F3358

MERCURY ION THRUSTER TECHNOLOGY

J.R. Beattie and J.N. Matossian

Hughes Research Laboratories
3011 Malibu Canyon Road
Malibu, California 90265

March 1989

NAS3-23775
Final Report
18 February 1983 through 18 October 1984

Sponsored By
NATIONAL AERONAUTICS AND SPACE ADMINISTRATION
Lewis Research Center
2100 Brookpark Road
Cleveland, OH 44135

NASA
National Aeronautics and Space Administration

Report Documentation Page

1. Report No.	2. Government Accession No.	3. Recipient's Catalog No.
NASA CR-174974		

4. Title and Subtitle	5. Report Date
Mercury Ion Thruster Technology	March 1989
	6. Performing Organization Code

7. Author(s)	8. Performing Organization Report No.
J.R. Beattie and J.N. Matossian	
	10. Work Unit No.

9. Performing Organization Name and Address	11. Contract or Grant No.
Hughes Research Laboratories 3011 Malibu Canyon Road Malibu, CA 90265	NAS 3-23775
	13. Type of Report and Period Covered
12. Sponsoring Agency Name and Address	Final Report 2/83 - 10/84
National Aeronautics and Space Administration Lewis Research Center 21000 Brookpark Road Cleveland, OH 44135	14. Sponsoring Agency Code

15. Supplementary Notes

Project Manager: V.K. Rawlin, NASA Lewis Research Center
Cleveland, Ohio

16. Abstract

The Mercury Ion Thruster Technology program was an investigation for improving the understanding of state-of-the-art mercury ion thrusters. Emphasis was placed on optimizing the performance and simplifying the design of the 30-cm-diameter ring-cusp discharge chamber. Thruster performance was improved considerably; the baseline beam-ion-production cost of the optimized configuration was reduced to $\epsilon_i \simeq 130$ eV/ion. At a discharge propellant-utilization efficiency of 95%, the beam ion-production cost was reduced to about 155 eV/ion, representing a reduction of about 40 eV/ion over the corresponding value for the 30-cm-diameter J-series thruster. Comprehensive Langmuir-probe surveys were obtained and compared with similar measurements for a J-series thruster. A successful volume-averaging scheme was developed to correlate thruster performance with the dominant plasma processes that prevail in the two thruster designs. The average Maxwellian-electron temperature in the optimized ring-cusp design is as much as 1 eV higher than it is in the J-series thruster. Advances in ion-extraction-electrode fabrication technology were made by improving materials-selection criteria, hydroforming and stress-relieving tooling, and fabrications procedures. An ion-extraction performance study was conducted to assess the effect of screen aperture size on ion-optics performance and to verify the effectiveness of a beam-vectoring model for three-grid ion optics. An assessment of the technology readiness of the J-series thruster was completed, and operation of an 8-cm IAPS thruster using a simplified power processor was demonstrated.

17. Key Words (Suggested by Author(s))	18. Distribution Statement
Electric Propulsion 30-cm Ion Thruster Ion Optics Ion Propulsion	Unclassified - Unlimited

19. Security Classif. (of this report)	20. Security Classif. (of this page)	21. No. of pages	22. Price
Unclassified	Unclassified	162	

TABLE OF CONTENTS

TABLE OF CONTENTS (Continued)

LIST OF ILLUSTRATIONS

LIST OF ILLUSTRATIONS (Continued)

LIST OF ILLUSTRATIONS (Continued)

LIST OF ILLUSTRATIONS (Continued)

LIST OF TABLES

FOREWORD

The work described in this report was performed in the Plasma Physics Department of Hughes Research Laboratories, which is managed by Dr. J. Hyman. The Hughes program manager and principal investigator was Dr. J.R. Beattie. The NASA contract monitor was Mr. V.K. Rawlin of Lewis Research Center. Major technical contributions to this effort were made by:

J.R. Beattie	Program manager and principal investigator
J.N. Matossian	Discharge-chamber and ion-optics studies
R.L. Poeschel	J-series-thruster technology assessment, ion-optics fabrication technology
G.H. Fehlhauer and S. Kami	Ion-optics design, fabrication, and assembly
C.R. Dulgeroff and D.J. Hancock	Simplified power processor evaluation
G.A. Saenz	Thruster testing and technical assistance
D.R. Deane and R.L. Maheux	Thruster and hardware fabrication, assembly, and instrumentation

SUMMARY

The Mercury Ion Thruster Technology program was an investigation for improving the understanding of state-of-the-art mercury-ion-thruster systems. This was accomplished by comparing and contrasting the performance characteristics of the present-generation ring-cusp thruster with the performance characteristics of the more-mature J-series thruster. Emphasis was placed on optimizing the performance and simplifying the design of the ring-cusp discharge chamber. The dominant attributes characterizing the high performance of the ring-cusp thruster were identified, interpreted, and compared with those of the J-series thruster. Additional emphasis was placed on improving ion-optics fabrication technology. A study was conducted to identify the effect of aperture size and displacement on ion-optics performance and thrust-vectoring characteristics. An assessment of the technology readiness of the J-series thruster was completed, and a simplified power processor was successfully used to operate an 8-cm-diameter thruster that is functionally equivalent to the Ion Auxiliary Propulsion System (IAPS) thrusters.

The design of the ring-cusp discharge chamber was greatly simplified. A significant reduction in thruster mass was realized by eliminating the cathode magnet assembly and several magnet rings from the original thruster design. Along with the design simplifications and reduction in mass, thruster performance was improved considerably; the baseline beam-ion-production cost of the optimized configuration was reduced to $\epsilon_i \simeq 130$ eV/ion. At a discharge propellant-utilization efficiency of 95%, the beam-ion-production cost was reduced to about 155 eV/ion, representing a reduction of about 40 eV/ion over the corresponding value for the J-series thruster.

Comprehensive Langmuir-probe surveys were obtained to identify and correlate the performance characteristics of the ring-cusp thruster with the prevailing plasma processes occurring within its discharge chamber. These results were compared with similar measurements for the J-series thruster. A volume-averaging scheme was developed for analyzing the large volume of numerical data produced by Langmuir-probe surveys, allowing a quantitative and meaningful correlation of thruster performance with specific plasma processes characterizing the two thruster designs. Good correlation was obtained between thruster performance and the average Maxwellian-electron temperature of the discharge plasma. The average Maxwellian-electron temperature in the ring-cusp thruster was found to be as much as 1 eV higher than it is in the J-series thruster.

Significant advances were made in the materials-selection criteria, hydroforming and stress-relieving tooling, and fabrication procedures for ion-extraction assemblies. An ion-optics performance study was conducted to explore the influence of screen aperture size on ion-optics performance and to verify the effectiveness of a beam-vectoring model for three-grid ion optics.

An assessment of the technology readiness of the J-series thruster concluded that the major remaining technology issue is baffle and pole piece erosion, with subsequent deposition of material onto the cathode keeper and its supporting structure. Cathode-heater reliability was judged tractable through adequate quality-control procedures.

We successfully demonstrated the use of a simplified power processor to operate an 8-cm-diameter thruster that was functionally equivalent to the Ion Auxiliary Propulsion System (IAPS) thruster.

SECTION 1

INTRODUCTION

The goal of the Mercury Ion Thruster Technology program was to improve the understanding of mercury-ion-thruster systems, with primary consideration toward improving the technology and reliability of the state-of-the-art 30-cm-diameter J-series thruster. The present program extends the work that was performed under a previous investigation (NASA Contract NAS 3-21943), in which preliminary performance-characterization and plasma-diagnostic measurements were conducted using a high-performance thruster that utilizes a ring-cusp magnetic-confinement geometry. Because of its inherent simplicity and demonstrated performance capability, the ring-cusp design is perceived as a candidate for a new generation of ion thrusters that offers a significant performance advantage over the present J-series thruster.

The work performed under this program was conducted at Hughes Research Laboratories in Malibu, California. Appendix A describes the vacuum test facilities, instrumentation, and thruster diagnostics used in the thruster performance evaluations. Performance testing and plasma-diagnostic measurements were performed using a 30-cm-diameter laboratory-model ring-cusp discharge chamber, in addition to a J-series thruster (S/N J2). Details of these thruster designs are presented in Section 2 of this report.

1.1 PROGRAM GOALS

Emphasis was placed on optimizing the performance and simplifying the design of the ring-cusp discharge chamber. To aid in this effort, we performed detailed documentation of the performance, discharge characteristics, and plasma properties in several ring-cusp chamber geometries. Similar measurements were performed in a J-series thruster for comparison with the ring-cusp results. The objective was to understand the mechanisms

that prevail in the high-performance ring-cusp discharge chamber, with an eye toward incorporating those attributes of the ring-cusp design that result in its high performance into the more-mature J-series thruster. Other objectives were to improve ion-optics fabrication technology and to demonstrate the operation of a flight-type thruster using a simplified power processor. Both areas have direct impact on improving the reliability of the J-series thruster, as well as on future thruster designs.

1.2 PROGRAM ACCOMPLISHMENTS

The design of the ring-cusp discharge chamber was greatly simplified through the elimination of its cathode magnet and several of the original magnet rings.[2-1] Along with the design simplifications and reduction in mass, the performance of the discharge chamber was improved considerably. The baseline beam-ion-production cost of the optimized configuration was reduced to $\epsilon_i \simeq 130$ eV/ion. At a discharge-propellant-utilization efficiency of $(\eta_{md})_{unc} = 95\%$, the beam-ion-production cost was reduced to about 155 eV/ion, representing a reduction of about 40 eV/ion over the corresponding value for the J-series thruster.

Comprehensive Langmuir-probe surveys were conducted for the first time in a J-series thruster. The plasma properties derived from these measurements, along with similar results obtained from the ring-cusp thruster, provided valuable insight into the dominant ion-production processes that prevail in their discharge chambers. Both plasmas were found to be characterized by a two-group distribution of electrons, and average values of the electron energies and densities were defined in such a manner as to make them useful in comparing the performance characteristics of the two thrusters.

The technology for fabricating ion-extraction electrodes was improved considerably. Materials specifications have been determined which should ensure successful and reproducible fabrication of electrodes. The hydroforming and stress-relieving fixtures that are used in fabricating electrodes for both two-

and three-grid ion-optics assemblies were modified to ensure better results during these critical operations. Procedures for dishing and assembling electrodes were refined and documented. As a result of the advances in these three areas (materials-selection criteria, hydroforming and stress-relieving tooling, and fabrication procedures), Hughes was able to make a critical commitment to develop an ion-propulsion system for the International Telecommunications Satellite Organization (INTELSAT) that utilizes a three-grid ion-extraction assembly.

An assessment of the technology readiness of the J-series thruster concluded that the major remaining technology issue is baffle and pole piece erosion with subsequent deposition of material onto the cathode keeper and its supporting structure. Other minor issues, such as cathode-heater reliability, were judged to be tractable through adequate design and quality-control procedures.

A simplified power processor (that was developed under a Hughes IR&D project) was used to operate an 8-cm-diameter thruster that is functionally equivalent to the Ion Auxiliary Propulsion System (IAPS) thrusters. Steady-state performance measurements obtained while operating the thruster with a standard power processor and the simplified unit were essentially identical. Application of at least some of the technology used in the simplified approach has been use in a power processor that Hughes developed for use under the INTELSAT development program.

SECTION 2

RING-CUSP DISCHARGE-CHAMBER TECHNOLOGY

As a result of its high level of performance and inherent simplicity, the ring-cusp thruster is perceived as a potential replacement for other well-optimized designs such as the divergent-field J-series thruster. In the remainder of this section, we present the results of an in-depth investigation of the original ring-cusp configuration[2-1] to optimize its performance and better understand its operating characteristics.

2.1 DESIGN FEATURES

The ring-cusp and J-series thrusters differ primarily in the design and performance of their discharge chambers. Major differences include the magnetic-field distribution used to confine the discharge-chamber plasma, as well as the distribution of anode- and cathode-potential surfaces that define the discharge-chamber boundary. A detailed description of the evolution of the 30-cm-diameter ring-cusp thruster described herein is presented in Appendix B. Figure 2-1 shows a schematic diagram of the laboratory-model thruster. For comparison, a schematic of the 30-cm-diameter J-series thruster[2-2, 2-3] is also presented.

The ring-cusp discharge chamber is constructed of a cylindrical sidewall and circular endwall, both of which are magnetic and maintained at anode potential. The cathode and screen electrode are the only electrodes operated at cathode potential. In addition, the cathode and cathode keeper are positioned in the discharge chamber with no protective structure surrounding them. The discharge chamber of the J-series thruster, by contrast, is comprised of two non-magnetic metal parts; a circular endwall and a cylindrical outer shell which are operated at cathode potential, and an inner cylindrical liner

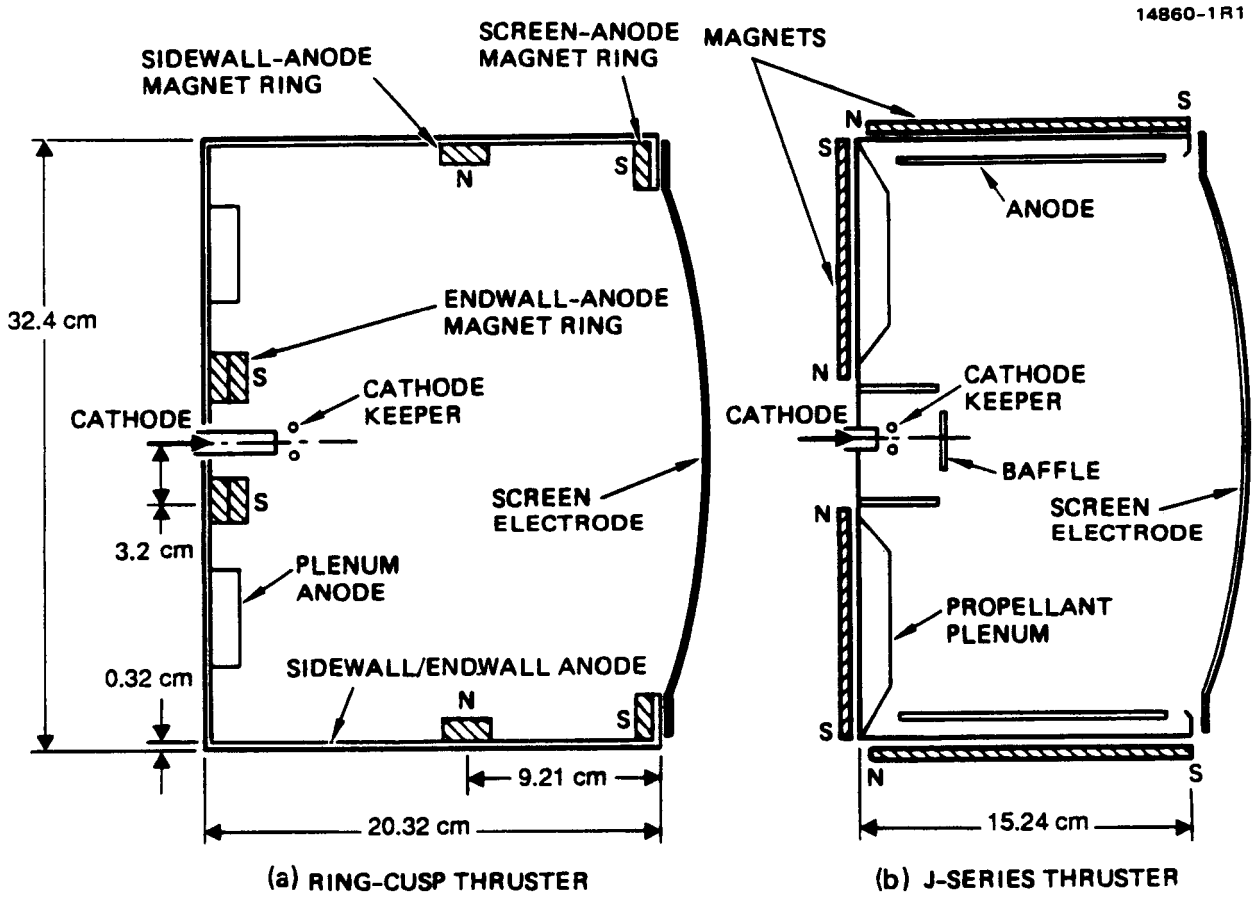

FIGURE 2-1. Schematic diagram of NASA/Hughes 30-cm-diameter ring-cusp and J-series thruster discharge chambers.

which is operated at anode potential. The cathode is surrounded by a magnetic-baffle coil that can be energized to control the current-flow impedance between the cathode and main-discharge plasmas. The entire cathode assembly (consisting of the cathode and cathode keeper) is located within a baffle/pole-piece assembly which isolates the cathode and main-discharge plasmas.

The magnetic-field distribution within the ring-cusp discharge chamber is generated by three samarium-cobalt ($SmCo_5$) permanent-magnet rings; two rings on the cylindrical sidewall and a circular ring on the endwall. In the laboratory-model thruster, the two sidewall magnet rings consist of a single layer of magnets, while the endwall ring has a double layer to increase the magnetic field strength. The individual magnets are rectangular in shape (1.9-cm-long by 1.27-cm-wide by 0.5-cm-high, and magnetized along the short dimension) and are held in place only by the magnetic attraction to the soft-iron boundary of the discharge chamber. The magnetic field at the surface of the magnets is about 2.5 kG, and their maximum operating temperature is about 300°C (above this operating temperature, irreversible loss of field strength occurs). The soft-iron chamber boundary provides a low-reluctance path for closing the magnetic-flux lines.

The magnetic-field distribution within the J-series discharge chamber is generated by axial and radial permanent magnets arranged along the outside of the chamber. The maximum operating temperature of the Alnico magnets used in the J-series thruster is much higher ($\simeq$750°C) than it is for the $SmCo_5$ magnets used in the ring-cusp thruster. However, the magnetic-field strength near the Alnico magnet faces is significantly lower ($\simeq$100 G). In addition, the discharge-chamber boundary of the J-series thruster serves as a structural member and is not a part of the magnetic circuit.

Documentation of the magnetic-field distribution within the ring-cusp discharge chamber included measurements of the vector components of the field, as well as the shape of the flux lines. The scalar field was obtained by measuring the axial and the radial components (B_z and B_r) of the magnetic field in the centerline plane of the discharge chamber, and then computing the scalar magnitude as $(B_z^2 + B_r^2)^{1/2}$ for each measurement point. The vector nature of the magnetic field was documented by using powdered iron to trace out the lines-of-force in the field.

Figure 2-2 compares the scalar-magnetic-field distribution for the ring-cusp and J-series thrusters. These results indicate that the most significant feature of the ring-cusp design is the existence of strong magnetic fields along the boundaries of its discharge chamber. By contrast, the J-series thruster exhibits a much weaker and nearly uniform scalar magnetic-field distribution.

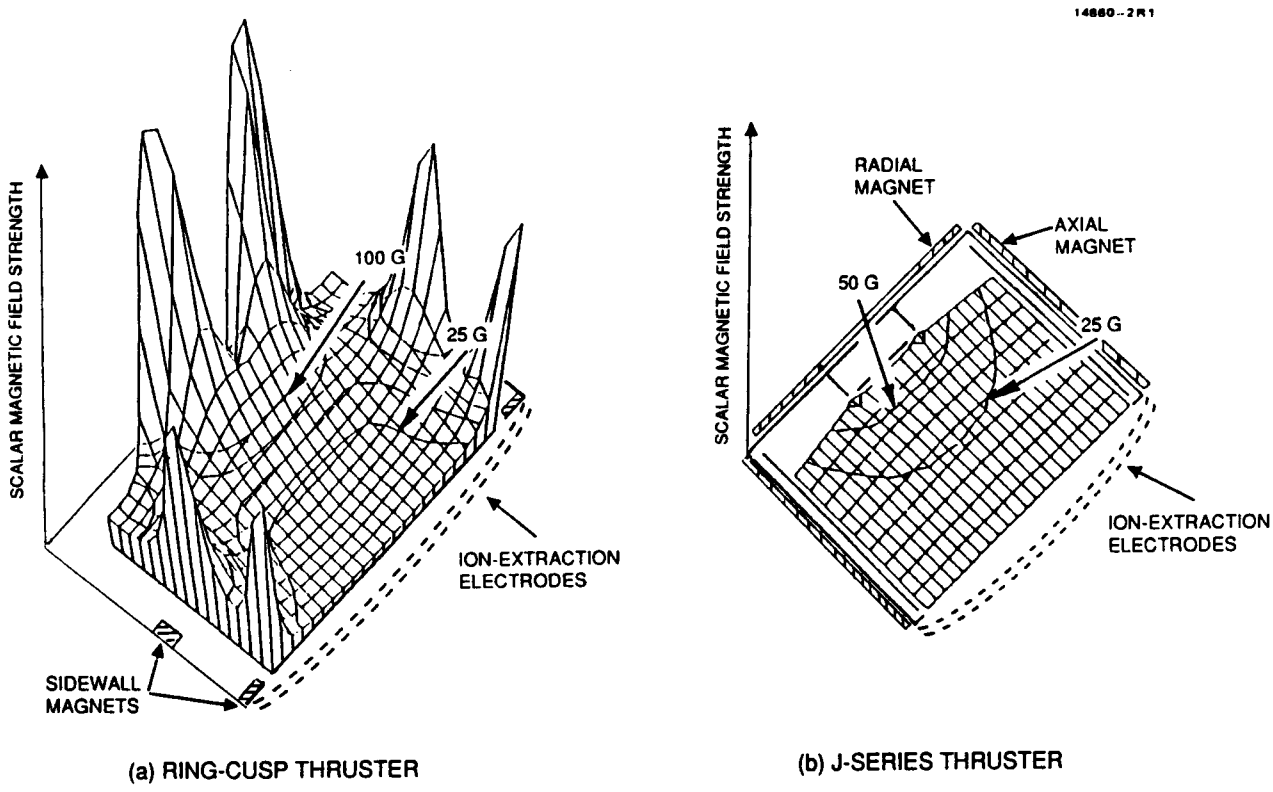

FIGURE 2-2. Scalar magnetic field distribution comparison.

The vector-magnetic-field distributions indicated by iron filing patterns in Figure 2-3 demonstrate the cusp nature of the magnetic-field distribution within the ring-cusp thruster and the divergent nature of the magnetic-field distribution within the J-series thruster. The cathode in the ring-cusp thruster is located in the endwall-cusp region, with a magnetic-field strength at the cathode orifice on the order of 100 G. By comparison, in the J-series thruster the cathode is located in a nearly magnetic-field-free region. Discharge-chamber design criteria determining the shape and magnitude of the magnetic field required for optimum performance of the ring-cusp thruster were explored in detail and the results are reported under a separate research program.[2-4]

2.2 PERFORMANCE CHARACTERISTICS

Figure 2-4 presents the performance of the 30-cm-diameter mercury ring-cusp thruster for a beam current of 2 A and a discharge voltage of 32 V (the standard operating conditions for the results presented in this report). The discharge-propellant-utilization efficiency has not been corrected for doubly charged ions. For comparison, similar measurements obtained for a 30-cm-diameter J-series thruster (S/N J2) are also presented to show the significant performance improvement that has been achieved with the optimized ring-cusp thruster. Figure 2-4 shows a performance improvement of about 40 eV/ion for the ring-cusp thruster operating at a propellant-utilization efficiency of 95%.

2.3 OPERATING CHARACTERISTICS

The strong magnetic fields at the boundary of the ring-cusp discharge chamber (see Figure 2-2) inhibit energetic electrons from reaching the anode-potential surfaces anywhere except in the cusp regions of the magnetic field defined by the three magnet rings. Energetic electrons are prevented from crossing the magnetic-flux lines that connect adjacent magnet

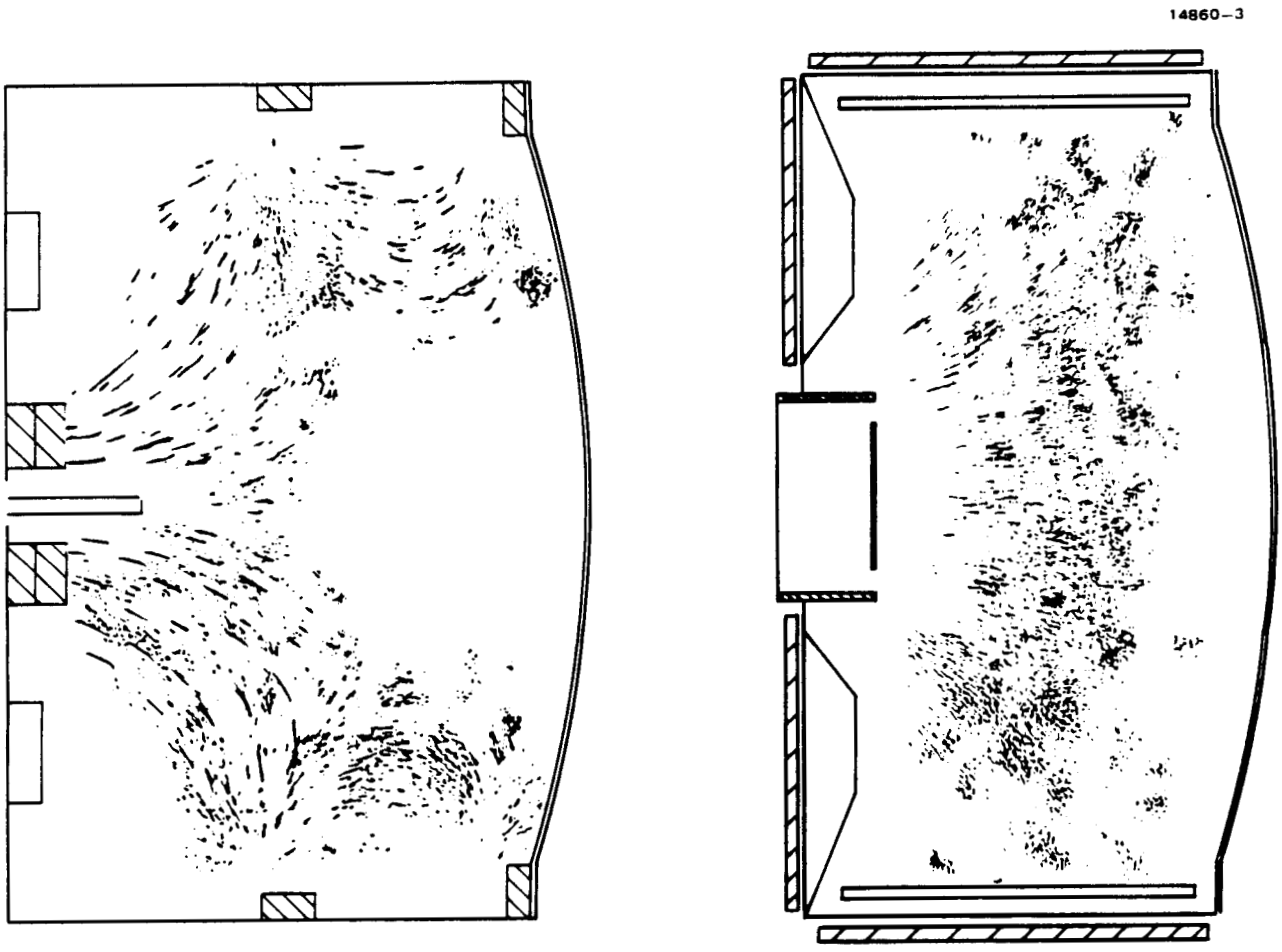

(a) RING-CUSP THRUSTER

(b) J-SERIES THRUSTER

FIGURE 2-3. Iron filings map of magnetic field.

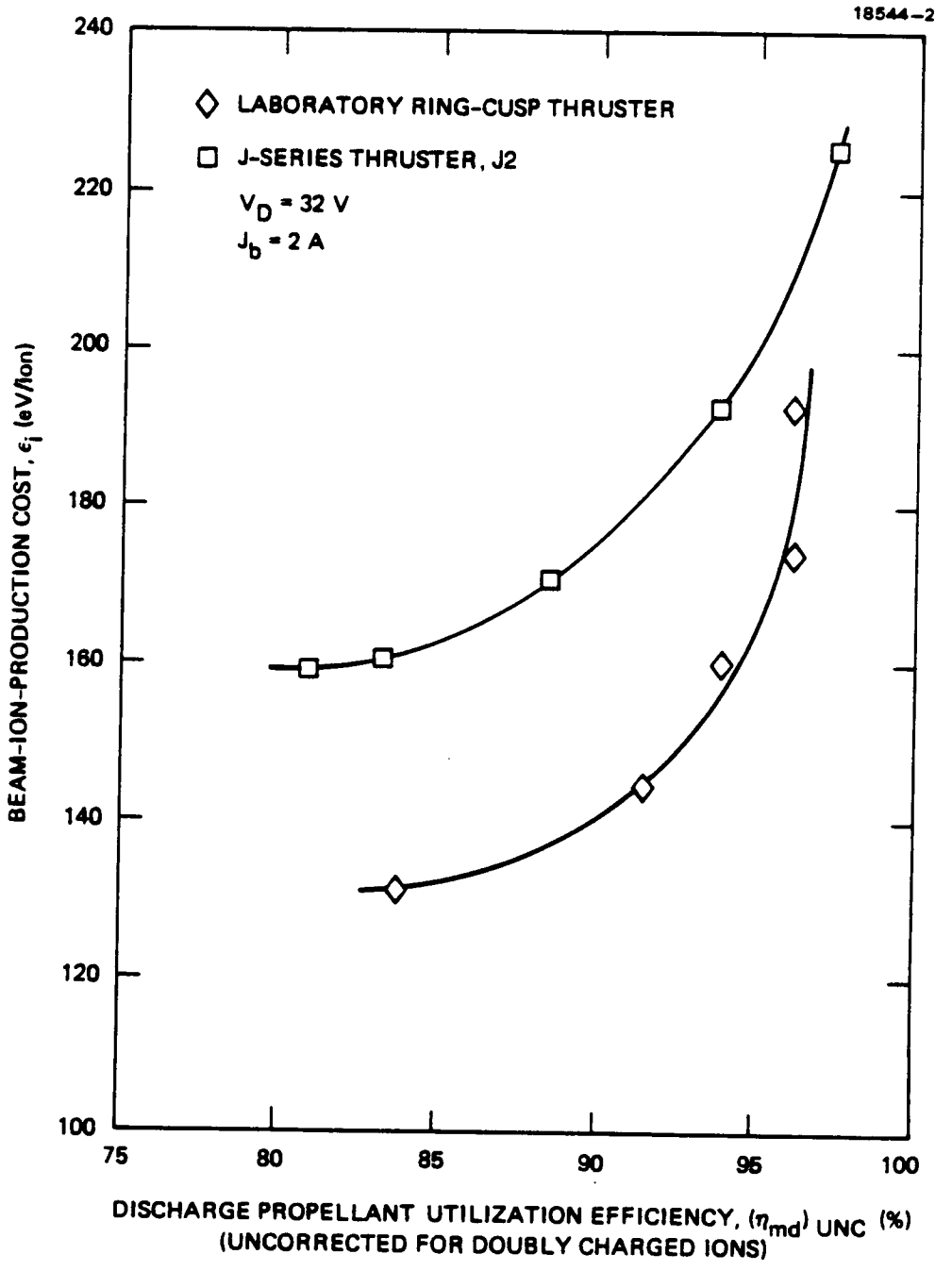

FIGURE 2-4. Thruster performance comparison.

rings by the large values of $\int Bdl$ (typically on the order of 1000 Gauss-cm).[2-5,2-6,2-7] Low-energy electrons cross the field lines more readily due to their much higher coulomb-collision cross section.

The electron current that sustains the discharge is influenced by the strong fields and small dimensions of the magnet cusps. It has been shown experimentally [2-8,2-9,2-10] that the effective area for electron collection at the cusps of the magnets is larger for low-energy electrons than it is for high-energy primaries. The ratio of these areas is found to agree with the ratio of the hybrid cyclotron radius, $(r_e r_i)^{1/2}$, to the primary-electron cyclotron radius, r_p. Therefore, the low-energy electrons tend to be preferentially "filtered out" in the magnetic cusps. The net result in the ring-cusp thruster is that plasma electrons bound to magnetic field lines that intersect the anode are reflected from the magnetic cusps due to mirror effects and limited conduction area. In this manner, the efficient confinement of ionizing plasma electrons is obtained.

Ions produced in the discharge chamber preferentially drift to the ion-extraction assembly at the ion-acoustic or Bohm velocity.[2-11,2-12] The magnetically shielded anode-potential surfaces within the discharge chamber limit the amount of ion loss. Both analytical[2-13] and experimental[2-13,2-14] investigations have shown that the ion-arrival rate at these surfaces is consistent with the ions having a velocity close to that of the slow-moving neutrals. With nearly all the discharge-chamber volume bounded by magnetically shielded anode-potential surfaces, ion loss within the ring-cusp discharge chamber is relatively low.

By comparison, the plasma in the J-series thruster is confined by a divergent magnetic field. Electrons must diffuse across magnetic field lines before being collected by the anode. Furthermore, electrons bound to magnetic-field lines that intersect the anode will be lost at that surface.

The discharge-chamber configuration in the J-series thruster is similar to conventional Penning discharge chambers, comprised of a combination of cathode-potential surfaces and magnetically shielded anode-potential surfaces. The endwall surface is a magnetically shielded cathode-potential surface and represents a substantial fraction of the total surface area of the discharge chamber. Magnetically shielded cathode-potential surfaces in general represent a greater loss-mechanism for ions than do magnetically shielded anode-potential surfaces.[2-13] This can account for higher ion-loss rates within the J-series discharge chamber and an accompanying reduction in thruster performance.

The description given above of ring-cusp thruster operation was verified by comprehensive measurements of the discharge-chamber plasma properties and current-flow measurements to the anode- and cathode-potential surfaces defining the discharge-chamber boundary. These results are presented in the material that follows.

2.3.1 Plasma Properties

Under this program, we developed a technique for correlating the dominant plasma processes occurring within the discharge chamber with observed thruster performance. Average values of the Maxwellian-electron temperature and density, as well as the primary-electron energy and density, were computed and correlated with thruster performance. A detailed description of this technique, including a comparison of the average plasma properties for the ring-cusp and J-series thrusters is presented in Reference 2-15.

Figure 2-5 shows the variation of the average primary-electron fraction (ratio of primary-electron density to plasma density) with beam-ion-production cost for both the ring-cusp and J-series thrusters. For comparison, performance measurements for these thrusters are also shown. (The propellant-utilization data of Figure 2-5 have been corrected for doubly charged ions, since the theory developed to compute the volume-averaged plasma properties does not account for multiply ionized atoms.)

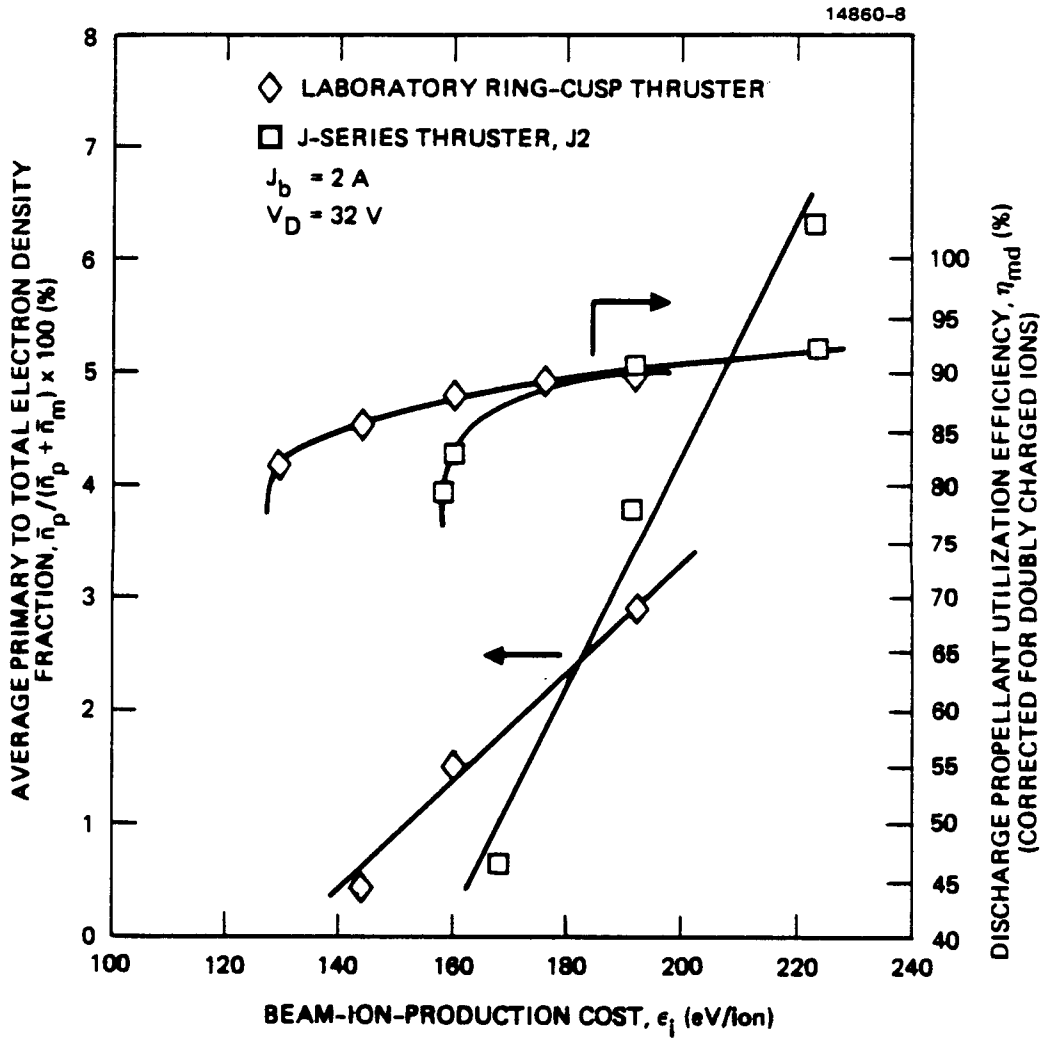

FIGURE 2-5. Volume-averaged primary electron density fractions.

The ring-cusp thruster maintains a higher primary-electron fraction than the J-series thruster as the beam-ion-production cost is lowered, demonstrating its superiority in confining primary electrons. Although the density of primary electrons is low (varying from 1% to 3%), it can be shown that the primaries are responsible for about 15% of the total ion production.[2-15]

The Maxwellian electrons are responsible for the balance of the ion production. Figure 2-6 shows measurements of the spatially varying Maxwellian-electron temperature for the ring-cusp and J-series thrusters. The electron temperature is constant along the magnetic-field lines[2-16,2-17] in both thrusters, and the isotherms have very nearly the same shape as the magnetic-field lines. This suggests that there is good plasma confinement for both thrusters. However, the electron temperature in the ring-cusp thruster is significantly higher. Figure 2-7 shows the variation of the average Maxwellian-electron temperature with beam-ion-production cost for both the ring-cusp and J-series thrusters. These results indicate that as the beam-ion-production cost is reduced, the ring-cusp thruster maintains an average Maxwellian-electron temperature that is about 1 eV higher than it is in the J-series thruster. The 1-eV increase evident in Figure 2-7 is substantial, especially considering that it represents an increase over the total volume of the ion-production region. A higher Maxwellian-electron temperature indicates more-efficient confinement of this species.

The results shown in Figures 2-6 and 2-7 indicate that the ring-cusp discharge chamber is more efficient in confining plasma, and this helps to explain the performance improvement over the J-series thruster. Calculations of the ion-production rate (ionization collision frequency) within the discharge chamber further demonstrate the effectiveness of the ring-cusp design in confining the discharge plasma. Figure 2-8 shows contours of the ionization collision frequencies (accounting for

14860-11

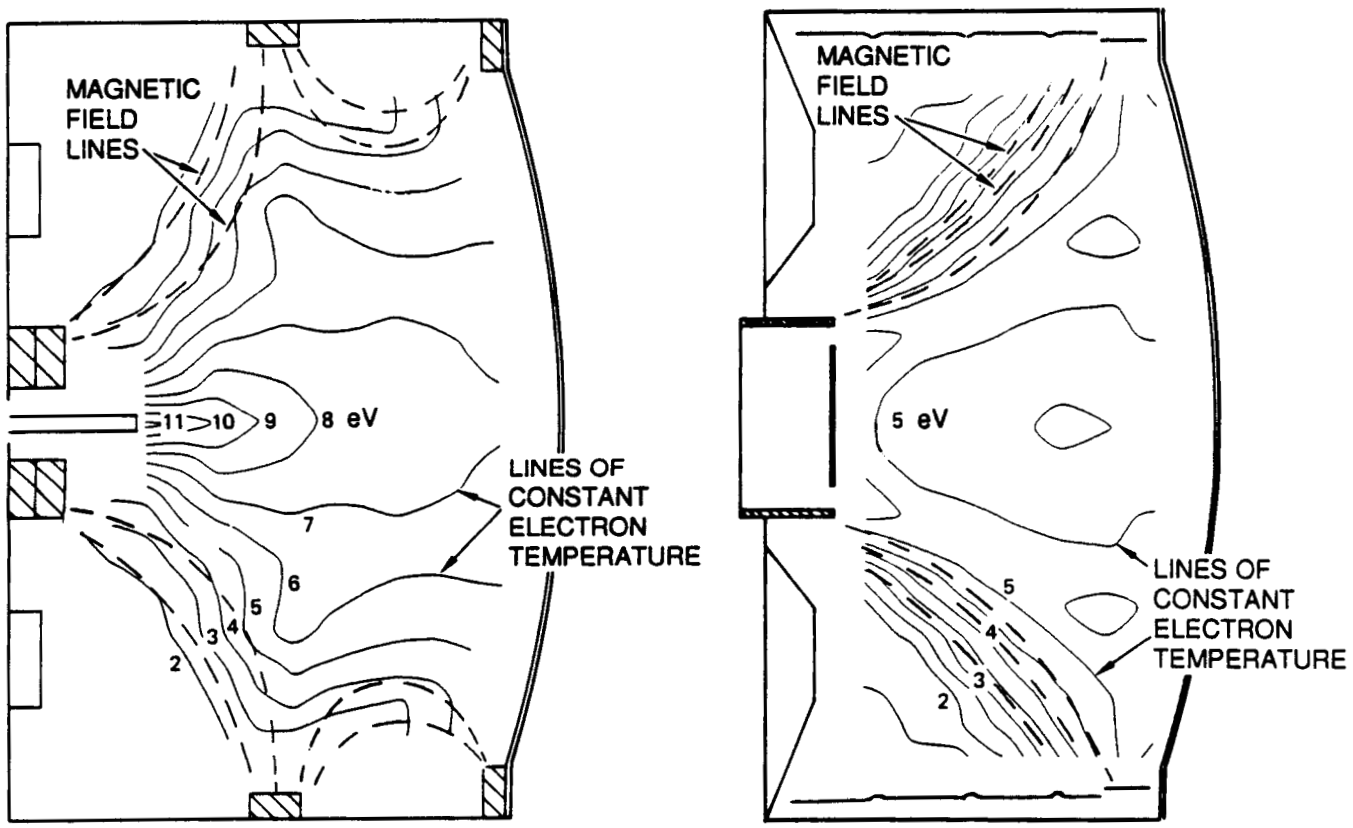

FIGURE 2-6. Spatially varying Maxwellian electron temperature.

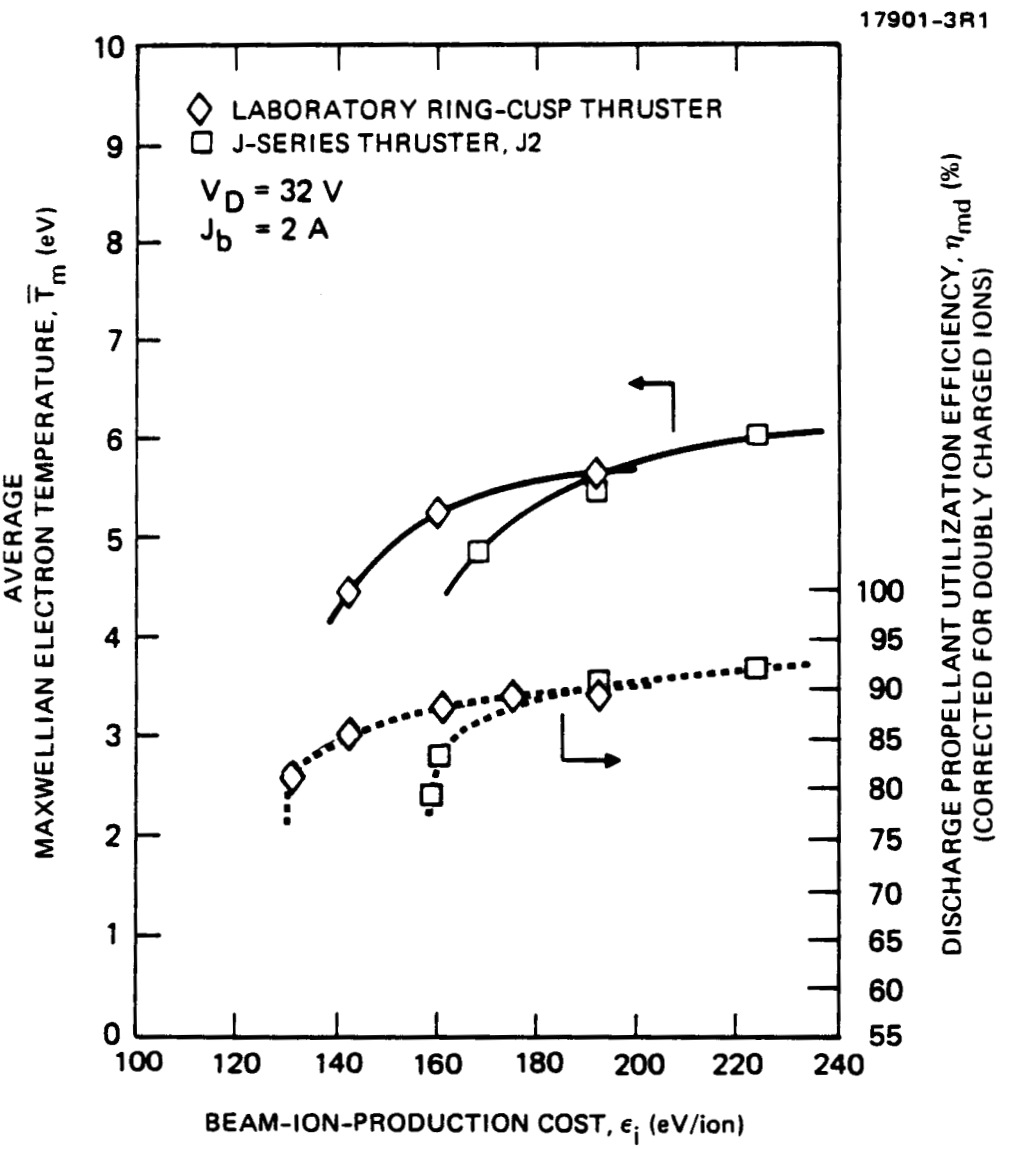

FIGURE 2-7. Volume-averaged Maxwellian electron temperature predictions.

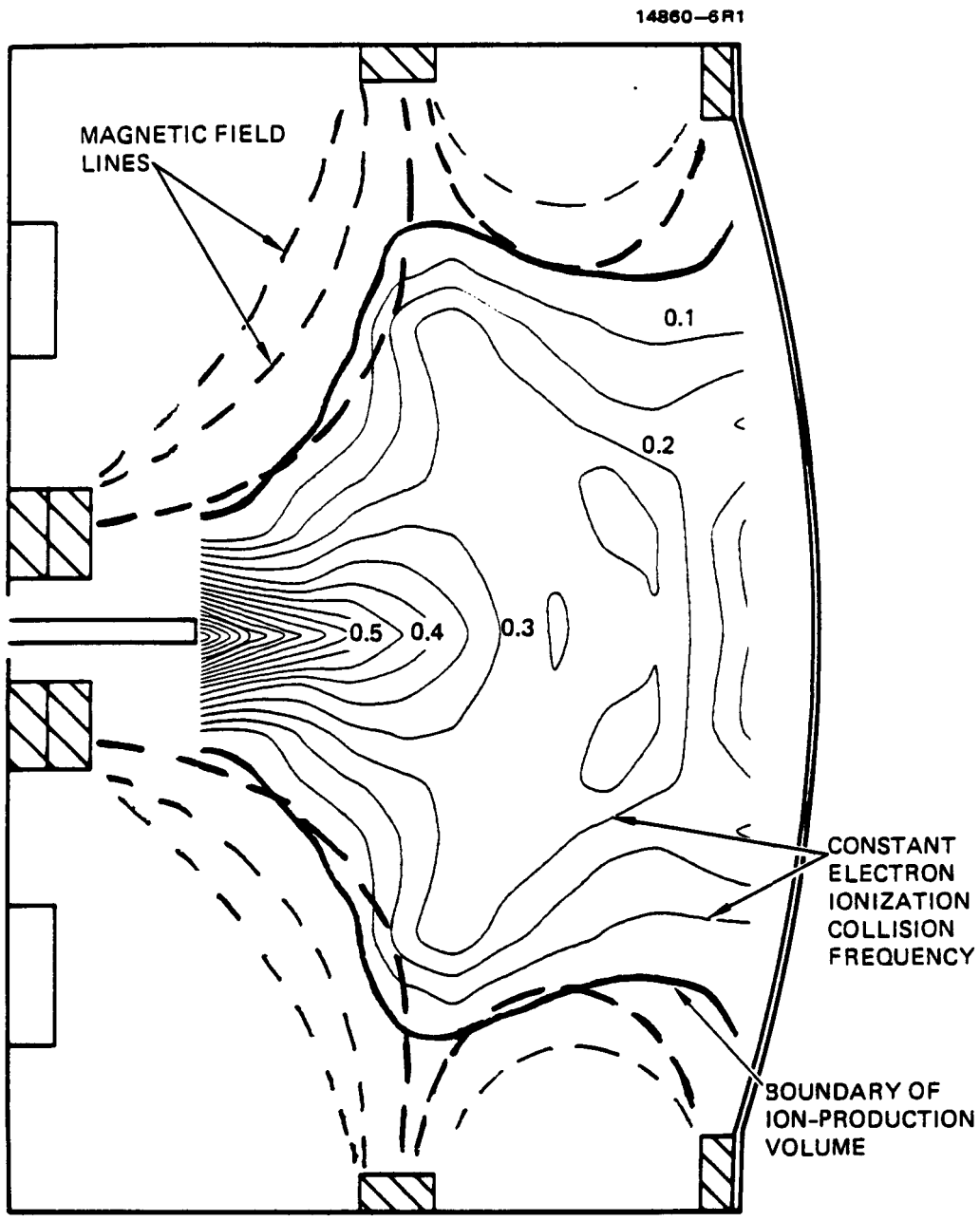

FIGURE 2-8. Normalized electron ionization collision frequency contours in ring-cusp thruster. ϵ_i = 160 eV/ion.

both Maxwellian and primary electrons) calculated from plasma properties measured in the ring-cusp discharge chamber. The contour lines have been normalized with respect to the maximum collision frequency. The solid line represents the boundary of the ion-production region, which is defined as the contour line that encloses 95% of the total ionization occurring within the discharge chamber.[2-16] This boundary also has very nearly the same shape as the magnetic-field lines (shown by dotted lines) used to confine the plasma.

The ion-production region is seen to be defined by the three magnet rings. The region of highest ion production extends from the axial location of the sidewall magnet ring to the axial location of the magnet ring nearest the ion-extraction assembly. Very little ion production occurs near the upstream location of the endwall magnet ring or near the magnetically shielded anode-potential sidewall/endwall boundary surfaces.

Having established where ions are produced, the plasma-potential distribution can be used to infer the direction of ion flow within the discharge chamber. Because of their large cyclotron radii, ions are influenced more by electric fields than they are by magnetic fields, with the electric fields produced by gradients in the plasma potential. Figure 2-9 shows contours of the plasma potential; there is about a 3 V drop in plasma potential between the region of highest ion production (cf. Figure 2-8) and the ion-extraction assembly. It is possible to infer from this gradient the presence of ion-accelerating potentials that result in directed ion transport away from regions of maximum ion production.

The concept of directed ion transport at the Bohm velocity has been studied and verified by several researchers.[2-11,2-12,2-14] We explored the concept of directed ion transport to the ion-extraction assembly by correlating the measured beam profile (as inferred by measurements obtained by sweeping a Faraday probe through the ion beam) with the calculated ion flux to the screen electrode of the ion-extraction assembly. The ion

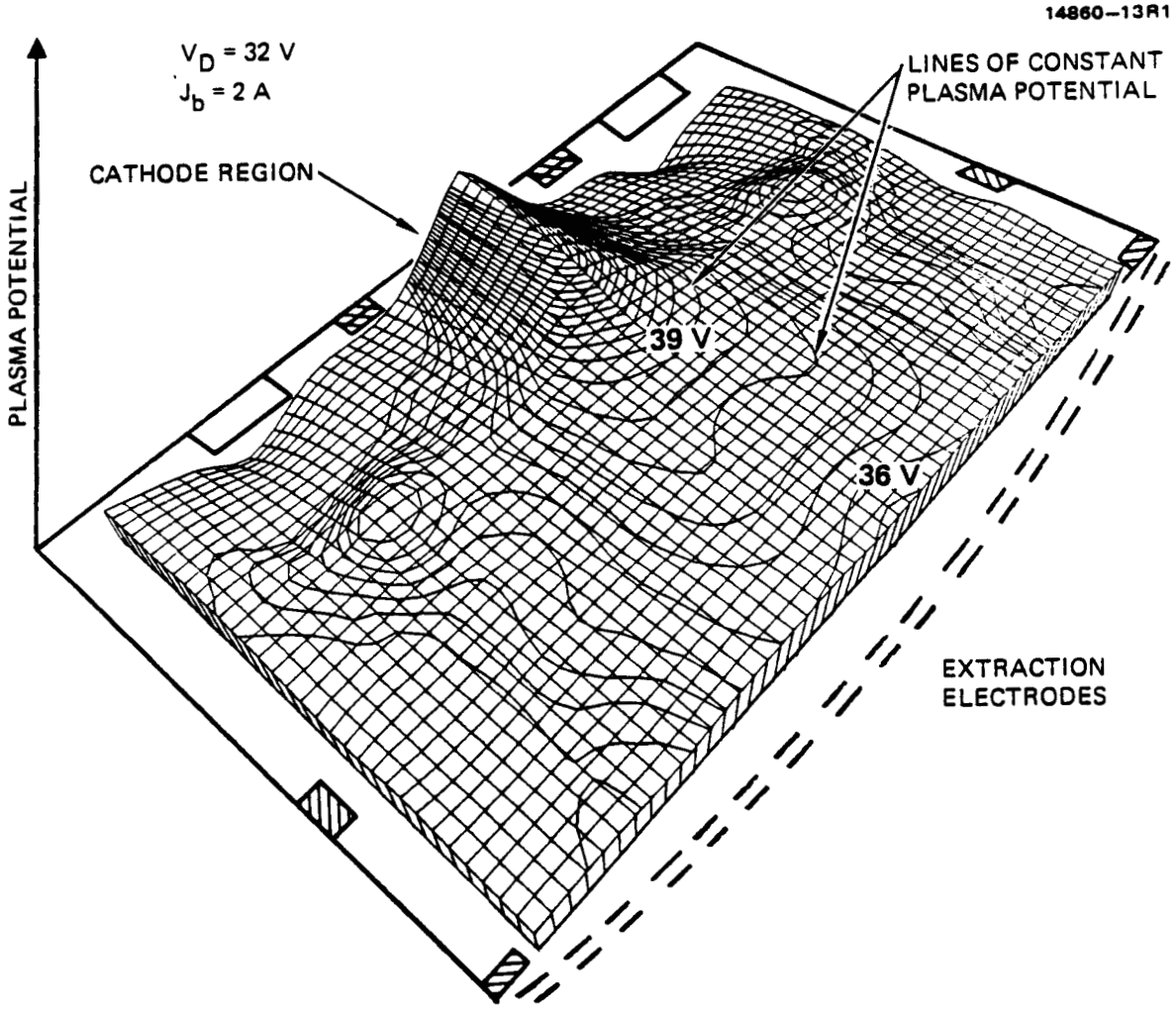

FIGURE 2-9. Three-dimensional plasma potential contours.

flux was obtained using the locally measured electron density and temperature, and invoking the assumption that the ions approach the ion-extraction assembly with the Bohm velocity. The calculated ion flux to the screen electrode is plotted along with a (typical) measured ion-beam profile in Figure 2-10; good correlation is indicated.

The ion-beam profile was found to decrease in uniformity as the beam-ion-production cost was increased. Figure 2-11 presents measured beam profiles that show a decrease in ion-beam uniformity as the ion-production cost increases. This effect is consistent with plasma properties measured within the discharge chamber, which indicate that the ion-production rate in the center of the discharge chamber increases with beam-ion-production cost.

It should be noted here that plasma potentials negative of anode potential were not observed in any operating mode of the ring-cusp thruster; the locally measured plasma potential was always positive of anode potential.

2.3.2 Current Distribution

The ion and electron currents flowing to the anode- and cathode-potential surfaces of the discharge chamber were measured and correlated with thruster operation. Each magnet ring was covered by a thin isolated cover that permitted the current collected by each cusp to be monitored. A diagram showing the measurement location of various electrode currents and voltages is shown in Figure 2-12. A list of symbols and definitions is provided in Table 2-1.

2.3.2.1 Anode-Potential Electrodes. The anode-potential interior of the discharge chamber shown in Figure 2-12 consists of five separate surfaces to which electron and ion currents can flow. Anodes labeled screen, sidewall, and endwall are the current-collecting surfaces for the screen, sidewall, and endwall magnet rings, respectively. The plenum and the sidewall/endwall comprise the remainder of the anode-potential surfaces. The cathode-potential interior of the discharge chamber consists of the cathode and screen electrode.

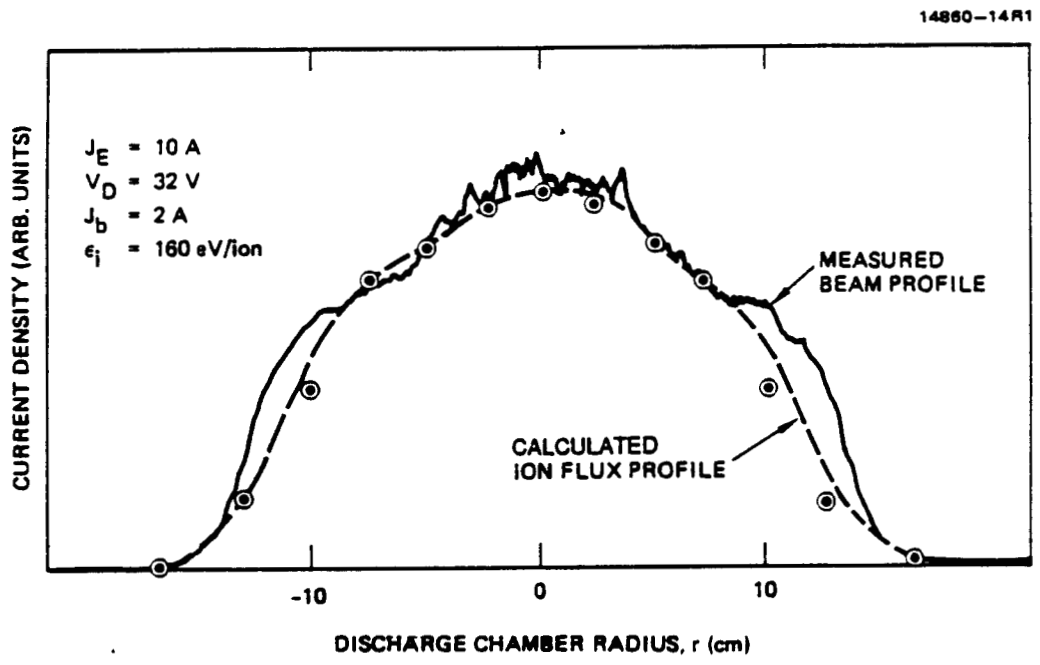

FIGURE 2-10. Measured beam profile and calculated ion flux profile.

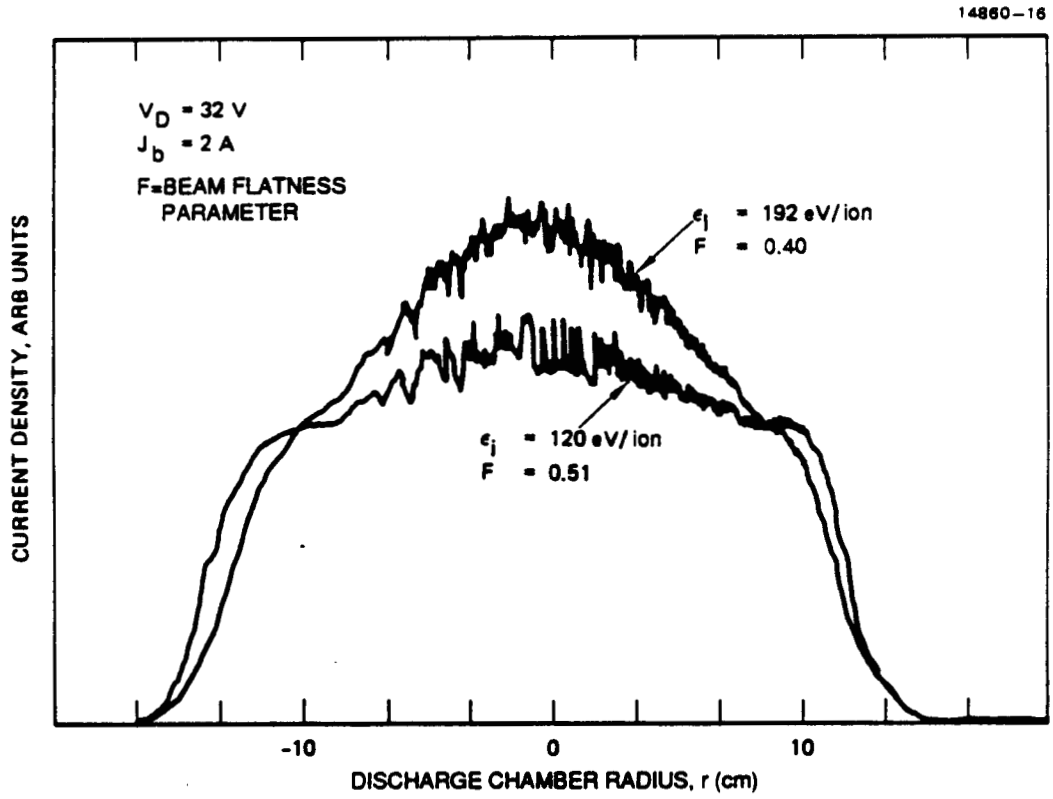

FIGURE 2-11. Behavior of measured beam profile.

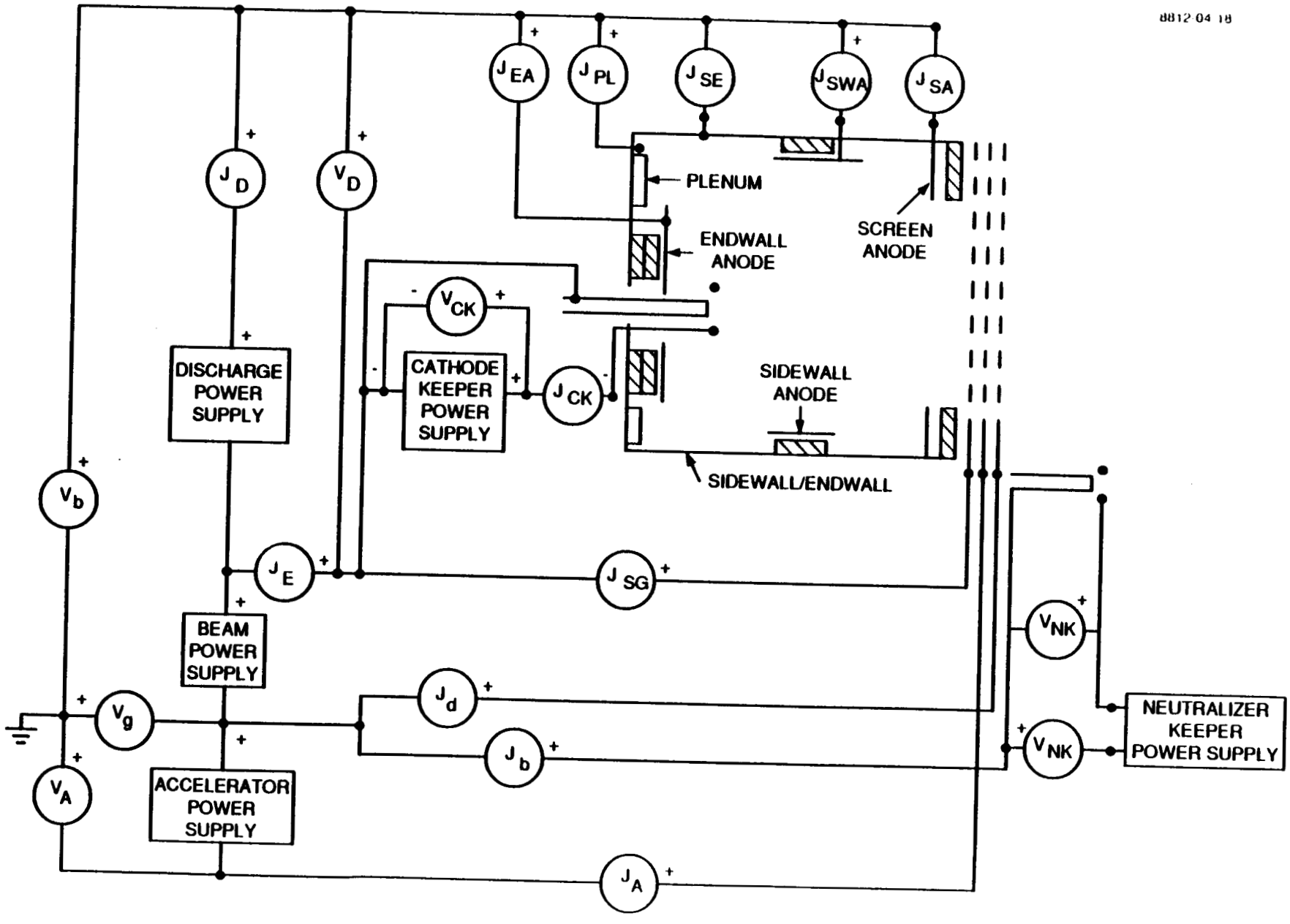

FIGURE 2-12. Schematic diagram of current and voltage measurements.

TABLE 2-1. Definitions of Symbols

V_b	Beam Voltage
J_b	Beam Current
V_A	Accelerator Voltage
J_A	Accelerator Current
J_d	Decelerator Electrode Current
J_E	Cathode Emission Current
J_{PI}	Current Collected by Plenum
J_{SG}	Current Collected by Screen Grid
J_{SA}	Current Collected by Screen Anode
J_{SWA}	Current Collected by Sidewall Anode
J_{SE}	Current Collected by Sidewall/Endwall
J_{EA}	Current Collected by Endwall Anode
V_D	Discharge Voltage
V_g	Neutralizer Coupling Voltage
V_{NK}	Neutralizer Keeper Voltage
J_{NK}	Neutralizer Keeper Current
V_{CK}	Cathode Keeper Voltage
J_{CK}	Cathode Keeper Current
$\epsilon_i = J_E V_D / J_b$	Beam-Ion-Production Cost
η_{md}	Discharge Propellant-Utilization Efficiency (Corrected for Doubly Charged Ions)
$(\eta_{md})_{unc}$	Discharge Propellant-Utilization Efficiency (Uncorrected for Doubly Charged Ions)

Figure 2-13 shows the variation of the net currents collected by the five anode-potential surfaces as a function of cathode-emission current. The variation of total anode current (the sum of the individual anode currents) is also presented, showing good agreement with the variation of the sum of the beam and cathode-emission currents; all net currents are satisfactorily accounted for.

The plenum and sidewall/endwall each collect a small ion current, which is on the order of 10 mA for the plenum and 70 mA for the sidewall/endwall. For clarity, the sum of these two currents is shown in Figure 2-13. By contrast, the screen, sidewall, and endwall anodes collect net-electron current. These results suggest excellent electron confinement to the three magnet rings that define the cusp regions of the magnetic field. The screen and sidewall anodes collect the majority ($\simeq$80%) of the electron current, independent of the cathode-emission current. This is due to the location of these two electrodes within the ion-production region; the axial location of the sidewall anode coincides with the region of highest ion production (cf. Figure 2-8), while the axial location of the screen anode coincides with the downstream end of the ion-production region near the ion-extraction assembly. For all but the screen anode, the net-electron current increases with cathode-emission current.

The net-ion current collected by the sidewall/endwall and plenum surfaces was determined by simultaneously biasing these surfaces negative with respect to the remaining anode-potential surfaces. The results are shown in Figure 2-14, indicating that the net-ion current flowing to the combined sidewall/endwall-plenum surface varies from about 140 mA to 150 mA as the cathode-emission current decreases from 12 A to 9 A, while the net-electron current varies from about 70 mA to 80 mA. The ion current saturates at a relatively low value of applied bias voltage ($\simeq$ 2 V), confirming that the electrons flowing to the sidewall/endwall-plenum surface have low energy.

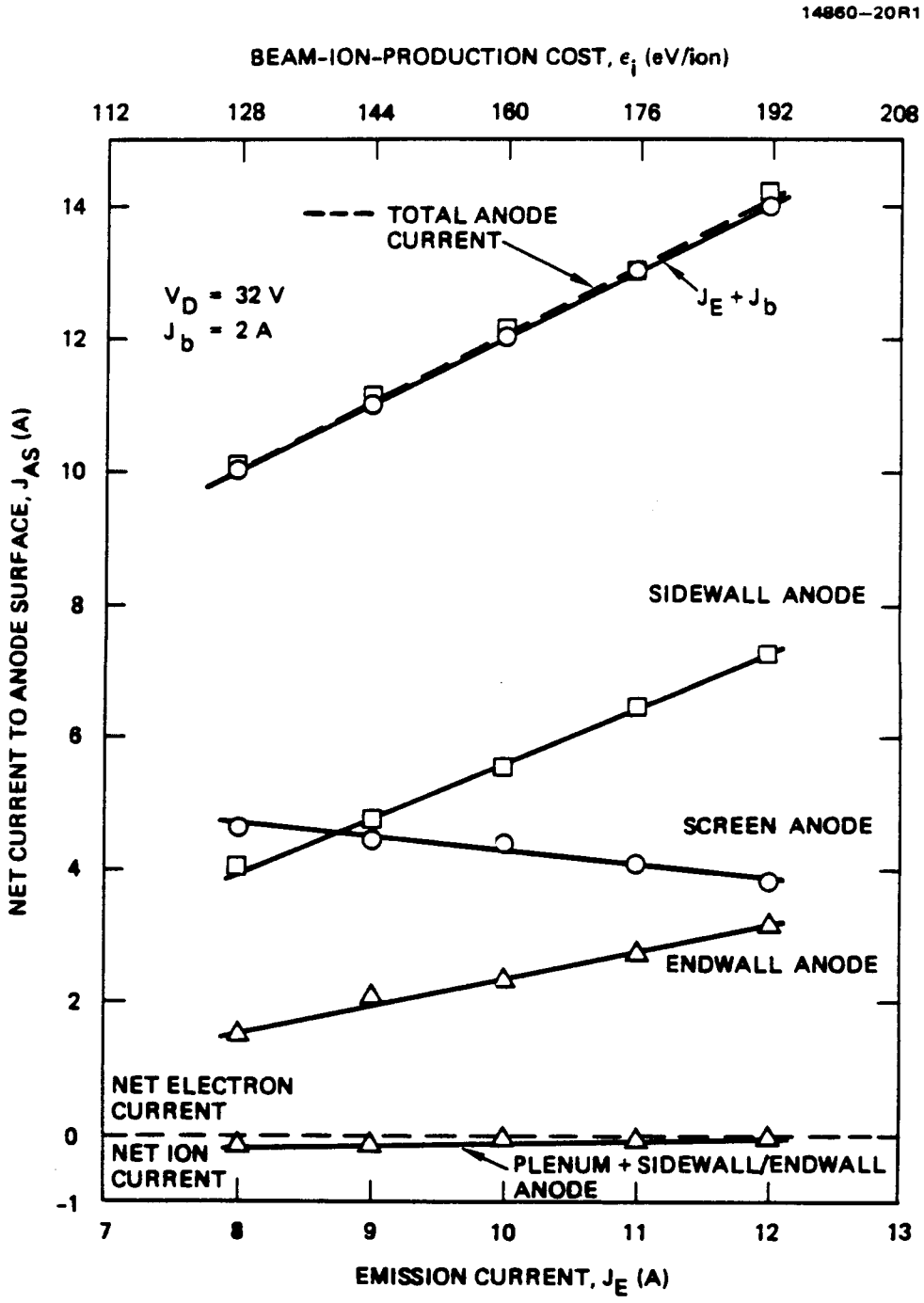

FIGURE 2-13. Net current collected by anode potential surfaces.

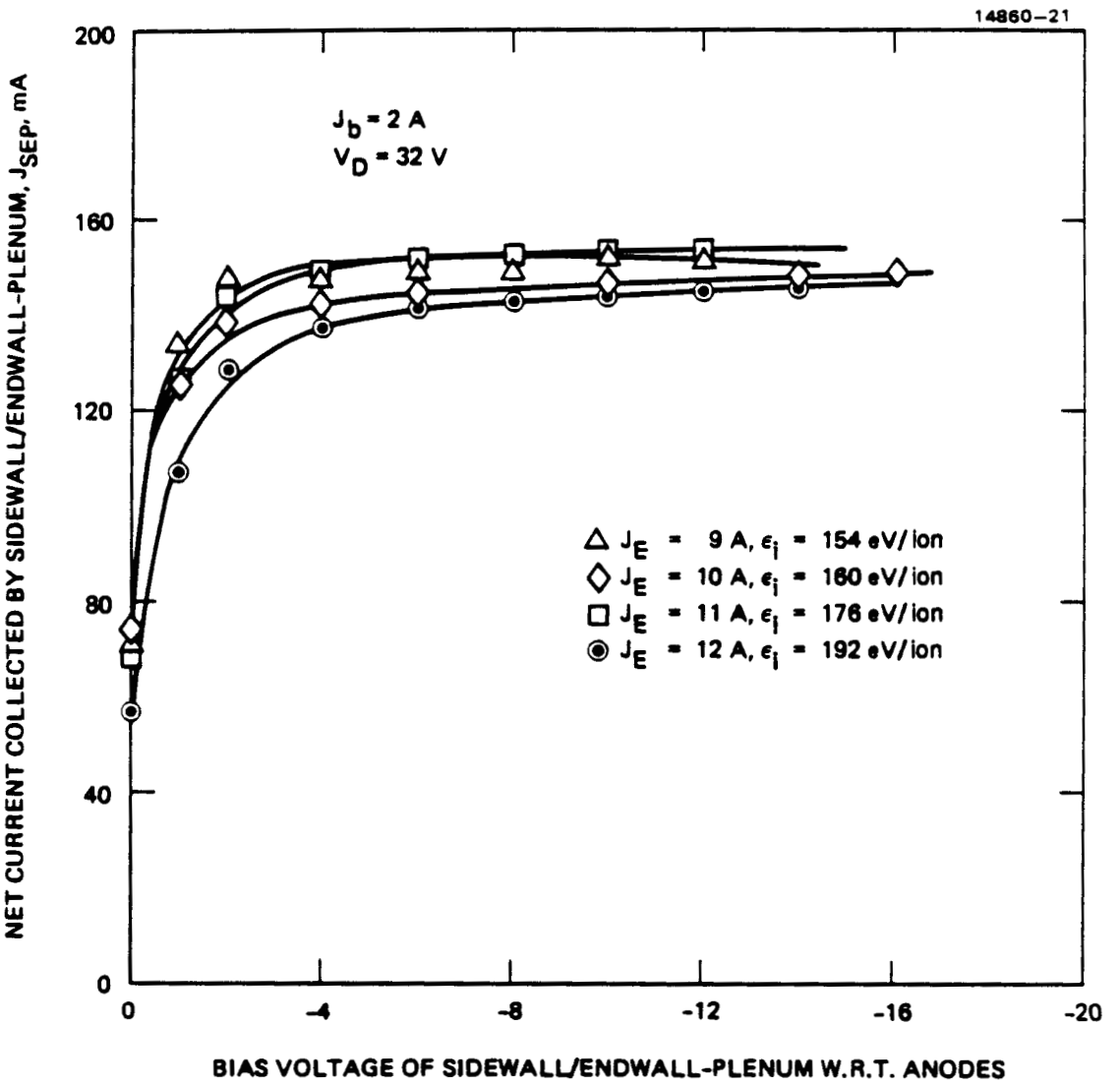

FIGURE 2-14. Saturated ion current collected by sidewall/ endwall plenum.

The sidewall/endwall-plenum satisfies the definition of a magnetically shielded anode-potential surface. The small current of low-energy electrons collected by this surface affirms the confinement of high-energy electrons to the cusp regions of the magnetic field. The small ion current collected by this surface is consistent with the concept of reduced ion transport to a magnetically shielded anode-potential surface.[2-13] Although we did not measure the ion loss to the three magnet-ring covers, Kaufman's model of reduced ion transport to magnetically shielded anode-potential surfaces can still be used to infer a small ion loss to the cusps as well.

2.3.2.2 Cathode-Potential Electrodes. The cathode and screen electrode are the only cathode-potential surfaces within the discharge chamber. The screen electrode is a loss surface for ions as well as energetic electrons capable of overcoming the potential difference between it and the plasma.

The ion current flowing to the screen electrode was determined by biasing it negative with respect to the cathode. The saturated ion current measured in this manner was 500 mA when the beam current was 2 A, implying an ion transmission of 80% for the particular ion-extraction assembly used in the test (S/N 914). The beam and accel electrode voltages were +1200 V and -350 V, respectively.

Measurements of the variation of net screen-electrode current with cathode-emission current (beam-ion-production cost) were obtained with the screen electrode connected to cathode through an ammeter. Figure 2-15 shows that as the cathode-emission current is reduced, the current collected by the screen electrode undergoes a transition from net-electron current to net-ion current. (For comparison, calculations of the volume-averaged Maxwellian-electron temperature shown previously in Figure 2-7 are included also). This behavior can be understood by considering the Maxwellian energy-distribution functions for electron temperatures corresponding to thruster operation above

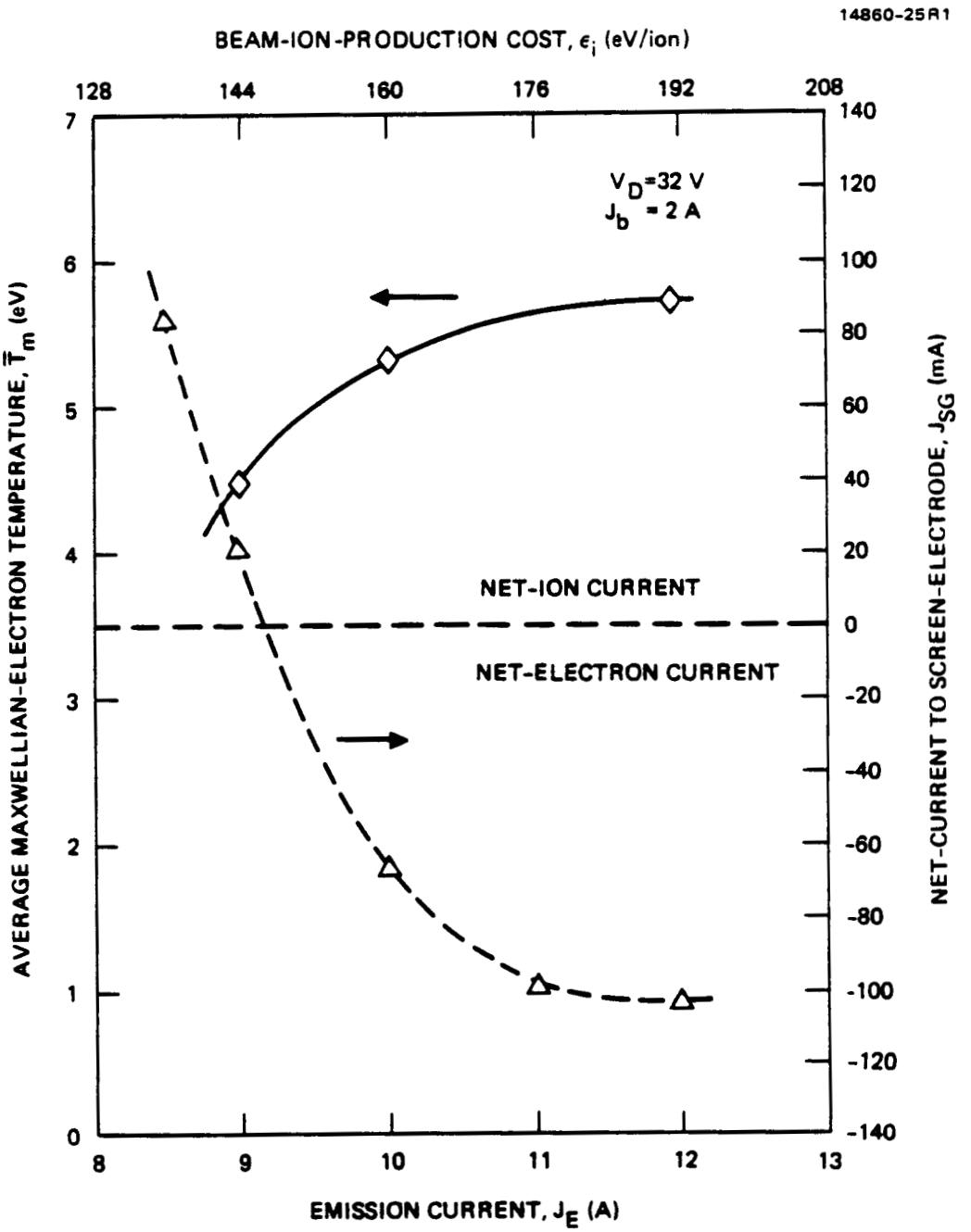

FIGURE 2-15. Net current collected by screen electrode.

and below the current-collection transition point shown in Figure 2-15. The energy-distribution functions for various electron temperatures are shown in Figure 2-16; by integrating the distribution function over the appropriate limits, one can compute the fraction of electrons having energies in excess of a specified value. For our purposes, we specify this value as 30-eV; approximately the plasma potential within the discharge chamber. Figure 2-17 presents results of calculations to show (as a function of temperature) the fraction of electrons that have energies in excess of 30 eV; this fraction increases from less than 1% for a 5-eV temperature to about 4% for a 7-eV temperature. Therefore, the transition from net-ion to net-electron current collection by the cathode-potential screen electrode can be understood to occur when the cathode-emission current is increased to the point that the electron temperature near the screen electrode exceeds about 4 eV. The volume-averaged electron temperatures presented in Figure 2-15 support this argument.

Correlation of the net current collected by the screen electrode with the Maxwellian-electron temperature suggests that this measurement can be used as a simple and fast diagnostic to compare the Maxwellian-electron temperature for different operating conditions. We utilize this technique in the sections that follow.

2.4 ANODE EFFECTS

We extended our study of current collection to the anode-potential surfaces within the discharge chamber by exploring the effect each anode surface has on influencing thruster performance. This was accomplished by allowing each separate anode surface to electrically float by disconnecting it from the discharge power supply. In this manner, the electron current collection could be redistributed to the various anode surfaces, in an attempt to effect a redistribution of the ion-production volume.

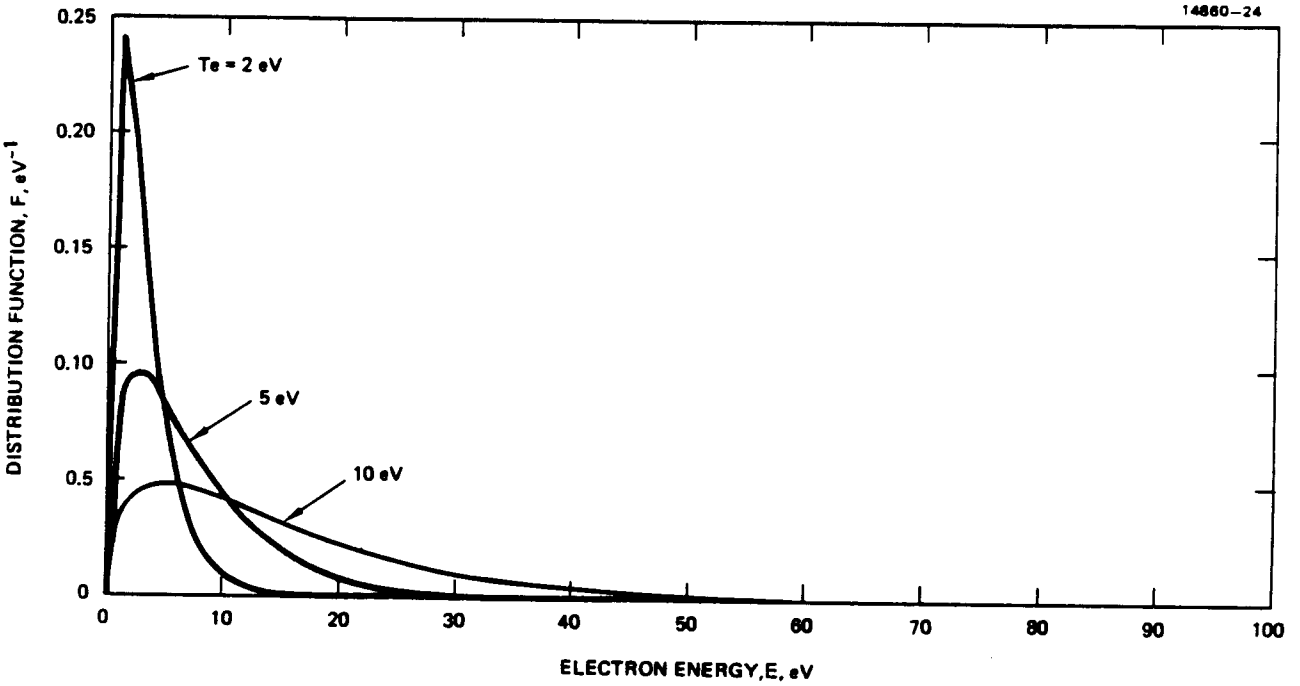

FIGURE 2-16. Maxwellian electron temperature distribution functions.

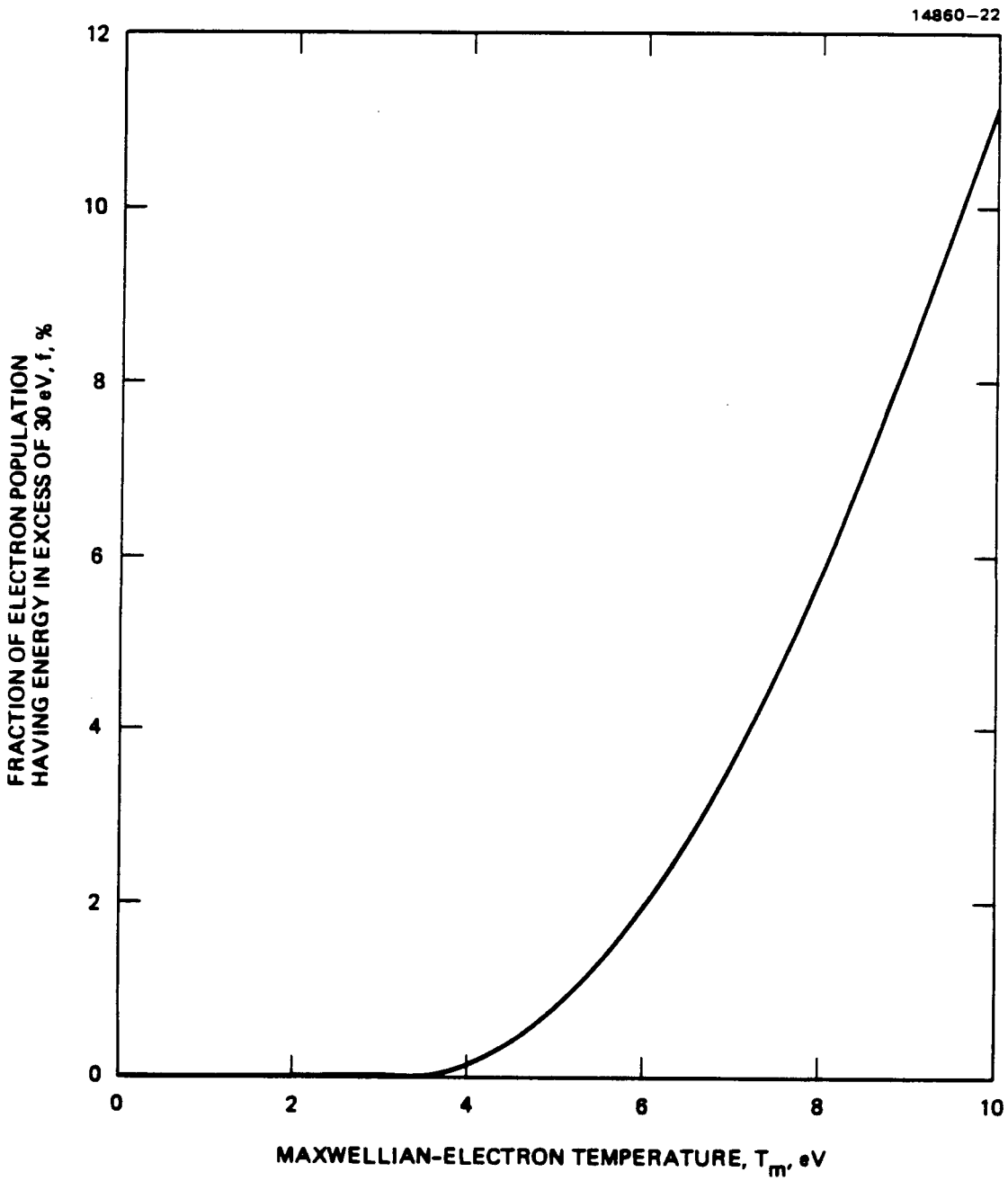

FIGURE 2-17. Calculated fraction of electrons having an energy in excess of 30 eV.

2.4.1 Endwall Anode and Plenum Floating

Figure 2-18 shows the measured variation of current collected by the various anode-potential surfaces (with the endwall anode and the plenum disconnected from the discharge power supply) as a function of cathode-emission current. The plenum and endwall anode comprise a relatively large portion of the endwall area. Compared to the usual case where all anode-potential surfaces are connected together (cf. Figure 2-13), the current collected by the screen anode changes by only a small amount. The current collected by the sidewall anode, however, increases by the amount that previously flowed to the plenum and endwall anode. The sidewall anode collects the majority of the current over a wide range of cathode-emission current.

The effect of electrically floating the various anode surfaces on discharge-chamber performance can be estimated from measurements of accelerator-electrode current and beam-ion-production cost. This is a fast and reliable technique to infer thruster performance. For thruster operation at high beam-ion-production cost, the neutral loss rate approaches a constant,[2-12] but as the beam-ion-production cost is reduced to its baseline value, the neutral loss rate increases. Since the accel current is directly proportional to the neutral loss rate, the variation of accel current with beam-ion-production cost can be used as an absolute indication of baseline beam-ion-production cost and as a relative indication of maximum discharge chamber propellant-utilization efficiency.

Figure 2-19 shows that there is very little change in the overall thruster performance when the endwall anode and the plenum are allowed to float. Furthermore, by floating the endwall anode and the plenum, the current collected by the sidewall anode, which is located in the region of maximum ion-production (cf. Figure 2-8), increases by 20%, yet this results in no significant change in (inferred) thruster performance.

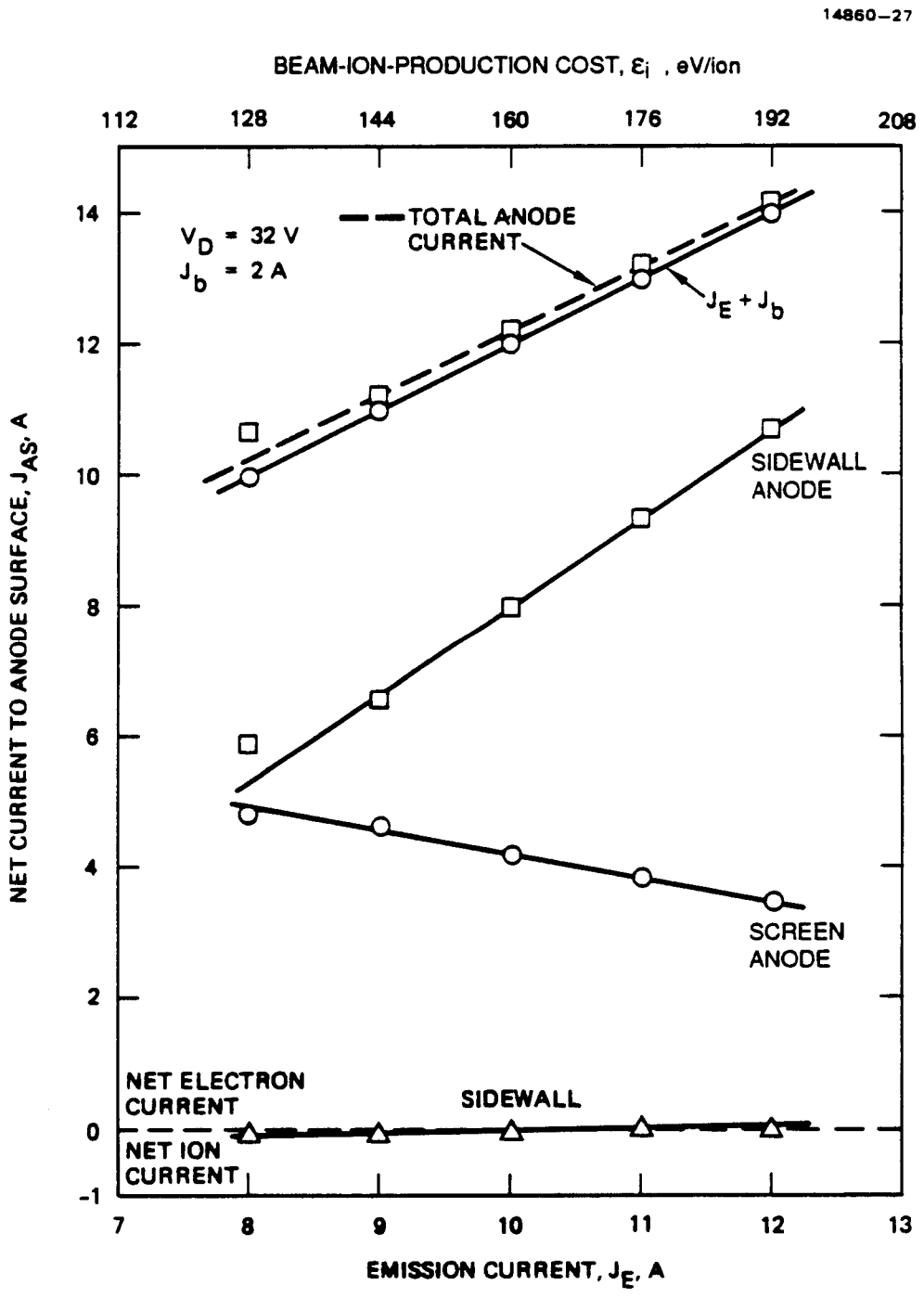

FIGURE 2-18. Net current collected by anode-potential surfaces; and plenum floating.

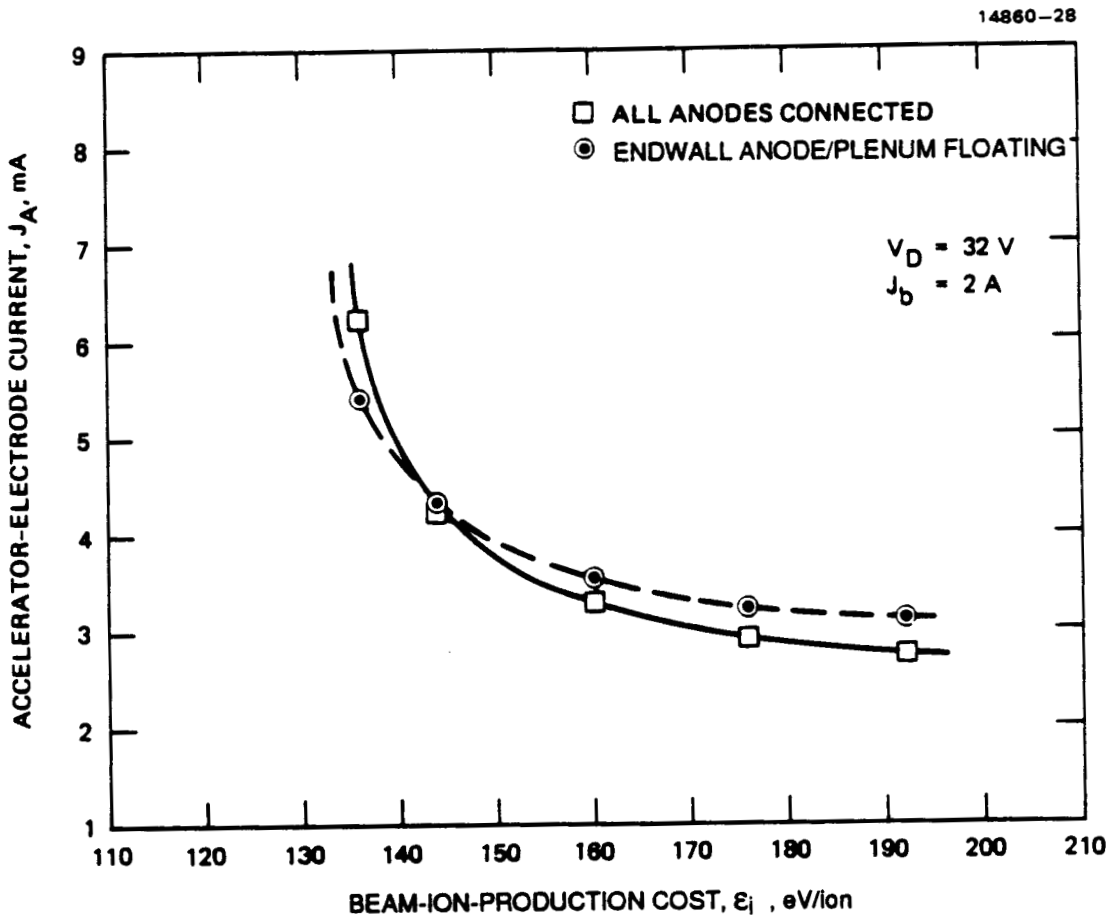

FIGURE 2-19. Variation of accel current with beam-ion-production cost; endwall anode and plenum floating.

Figure 2-20 shows the floating potential (relative to cathode potential) of the endwall anode and the plenum as a function of cathode-emission current. For comparison, anode potential is indicated as a dashed line. The endwall anode floats close to cathode potential, while the plenum floats near anode potential. This is understandable since the plenum is well shielded by the magnetic field and lies outside of the ion-production region; therefore, it collects little current. The endwall anode, on the other hand, defines the upstream boundary of the ion-production region (cf. Figure 2-8) and normally collects a substantial current. When this electrode is allowed to float, it must charge to a negative potential to balance the incident electron and ion currents. In addition, the floating potential of both the plenum and endwall anode decreases with increasing emission current. The floating potential is directly proportional to the electron temperature, which increases with cathode-emission current. Therefore, the floating potential becomes more negative with respect to plasma (anode) potential as the cathode-emission current is increased.

2.4.2 Screen Anode Floating

Figure 2-21 shows the net current collected by the anode surfaces for the case where the screen anode is allowed to float. Comparison with Figure 2-13 indicates that the electron current collected by the sidewall anode increases approximately by the amount of electron current that previously flowed to the screen anode. The current collected by the endwall anode remains essentially unchanged, and the plenum and sidewall/endwall collect net-electron current.

Figure 2-22 shows the effect on thruster performance (as inferred from the variation of accelerator-electrode current with beam-ion-production cost) of floating the screen anode. There is a significant reduction ($\simeq$12 eV/ion) in the baseline beam-ion-production cost and an indication of improved discharge-chamber

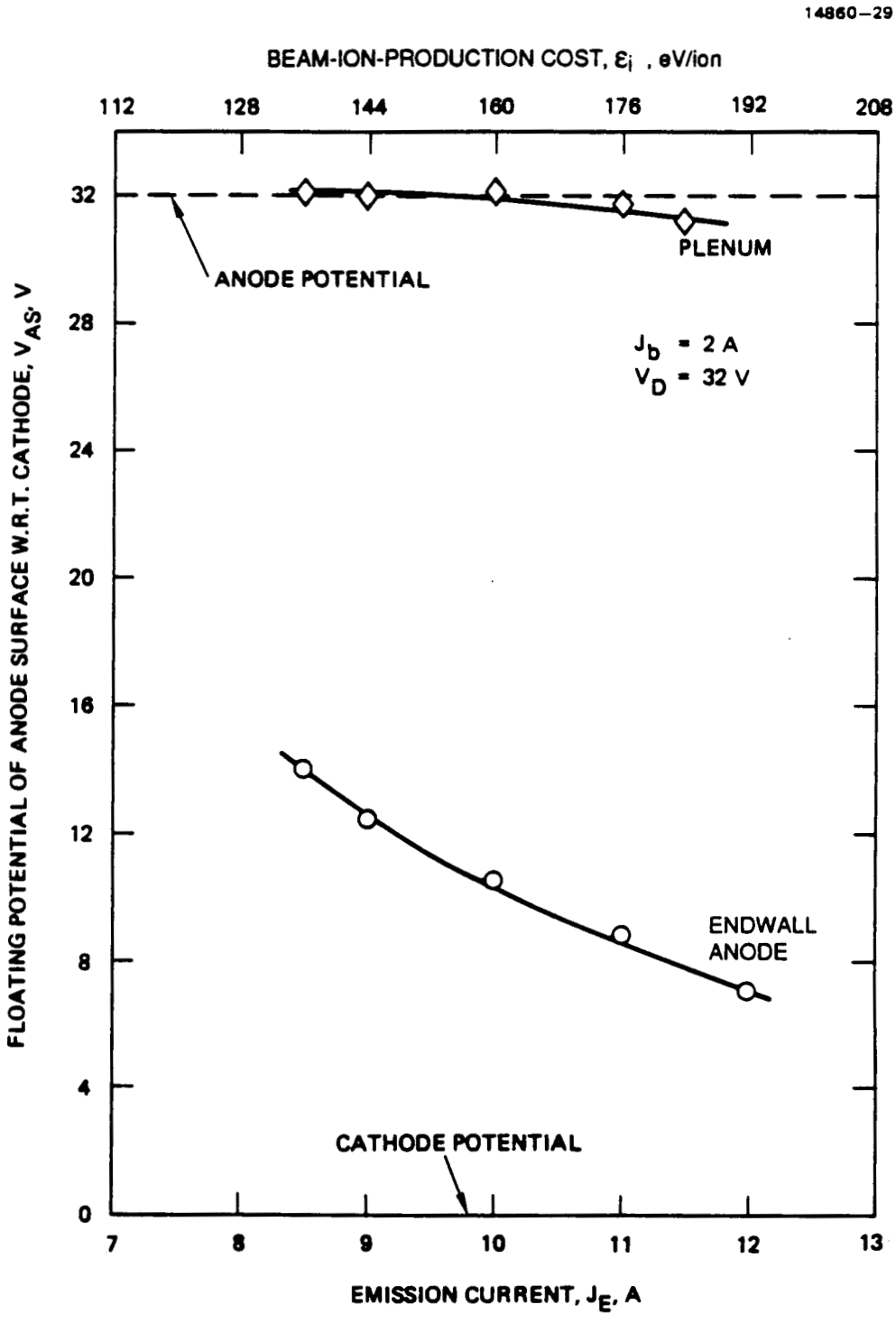

FIGURE 2-20. Floating potential of endwall anode and plenum.

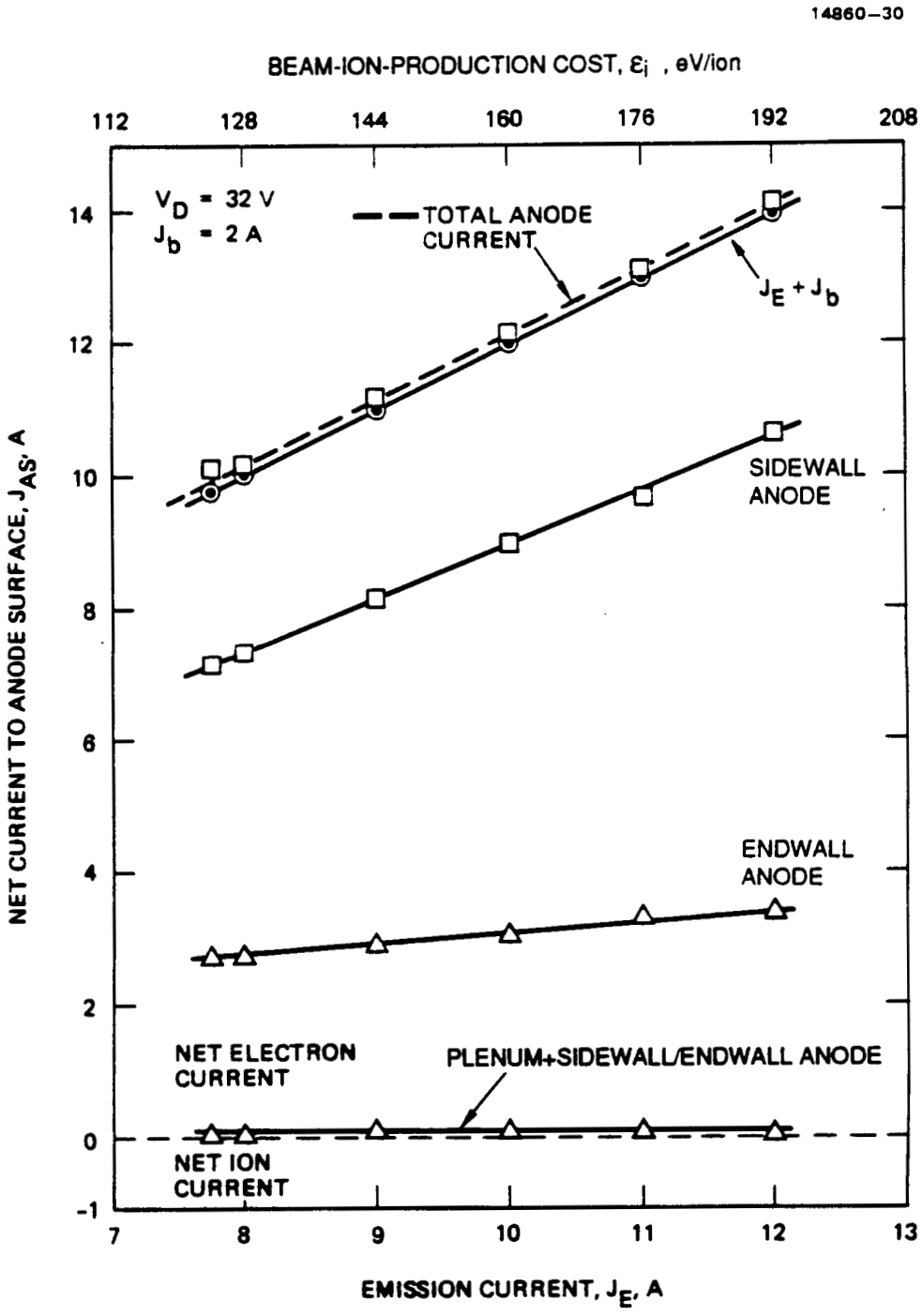

FIGURE 2-21. Net current collected by anode-potential surfaces; screen anode floating.

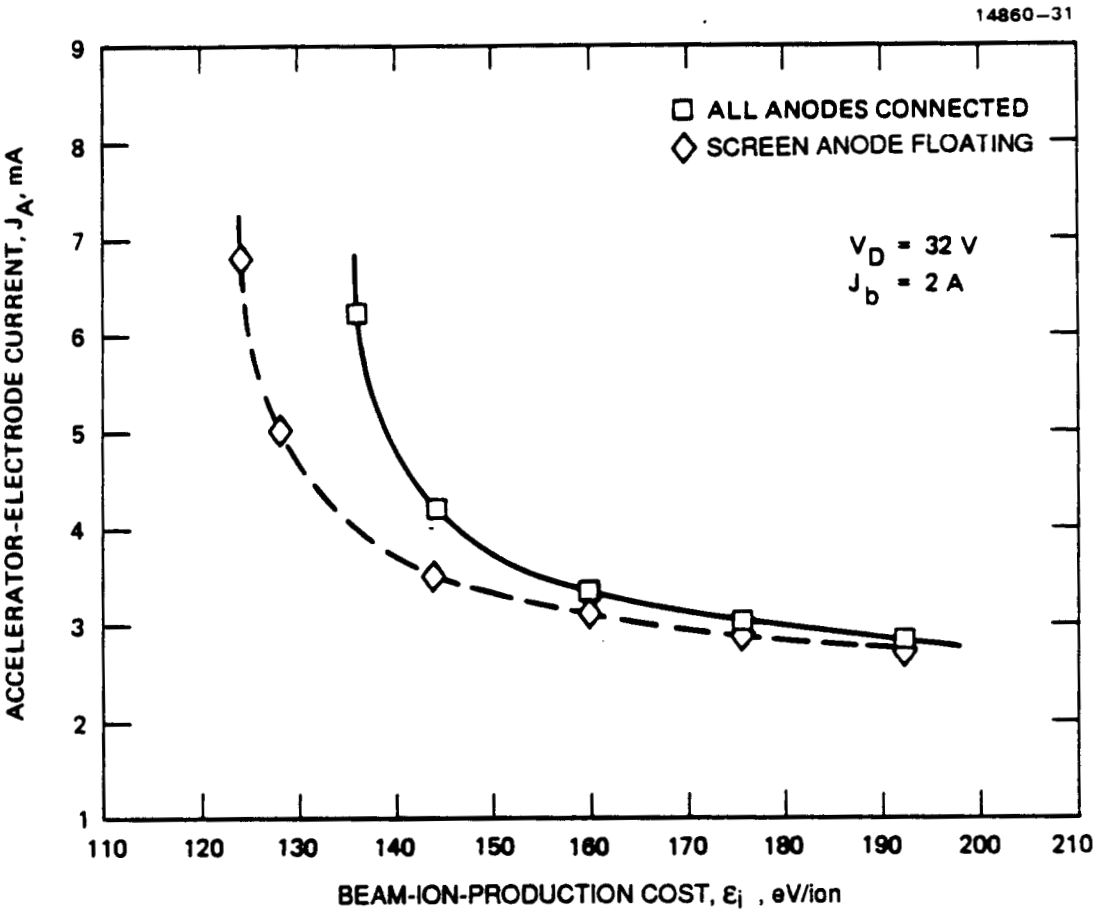

FIGURE 2-22. Variation of accel current with beam ion-production cost; screen anode floating.

propellant-utilization efficiency. The net-electron current collected by the plenum and sidewall/endwall could be due to a reduction in ion loss to these surfaces or to an increase in electron temperature. In the section below, we will show that the Maxwellian electron temperature increases significantly throughout the discharge chamber plasma when the screen anode floats. Figure 2-23 shows the floating potential of the screen anode as a function of cathode-emission current.

The reason for the observed performance improvement with the screen anode floating is believed to be an effect of reducing the electron-collecting anode area. The screen anode is located at the downstream end of the ion-production region (cf. Figure 2-8), where it collects a substantial electron current. Since floating the screen anode restricts electron flow to this electrode, the effective anode area within the ion-production region is reduced. The role of anode area on the performance of ion thrusters has been studied in the past by several researchers.[2-18, 2-19] According to their results, a reduction in the anode area could cause an increase in the electron temperature and, therefore, an improvement in thruster performance. We explored the validity of this model by obtaining Langmuir-probe measurements of the discharge-chamber plasma properties for thruster operation with and without the screen anode floating. Calculated values of the volume-averaged Maxwellian-electron temperature are shown in Figure 2-24, along with measurements of the net current collected by the screen electrode. The net current increase to the screen electrode is correlated with an increase in electron temperature. This result is consistent with the performance improvement suggested by the results shown in Figure 2-22.

2.4.3 Sidewall Anode Floating

Floating the sidewall anode resulted in a loss in thruster performance. It was found, for example, that for thruster operation at a beam-ion-production cost of 192 eV/ion, the accelerator-electrode current was well in excess of 10 mA (as

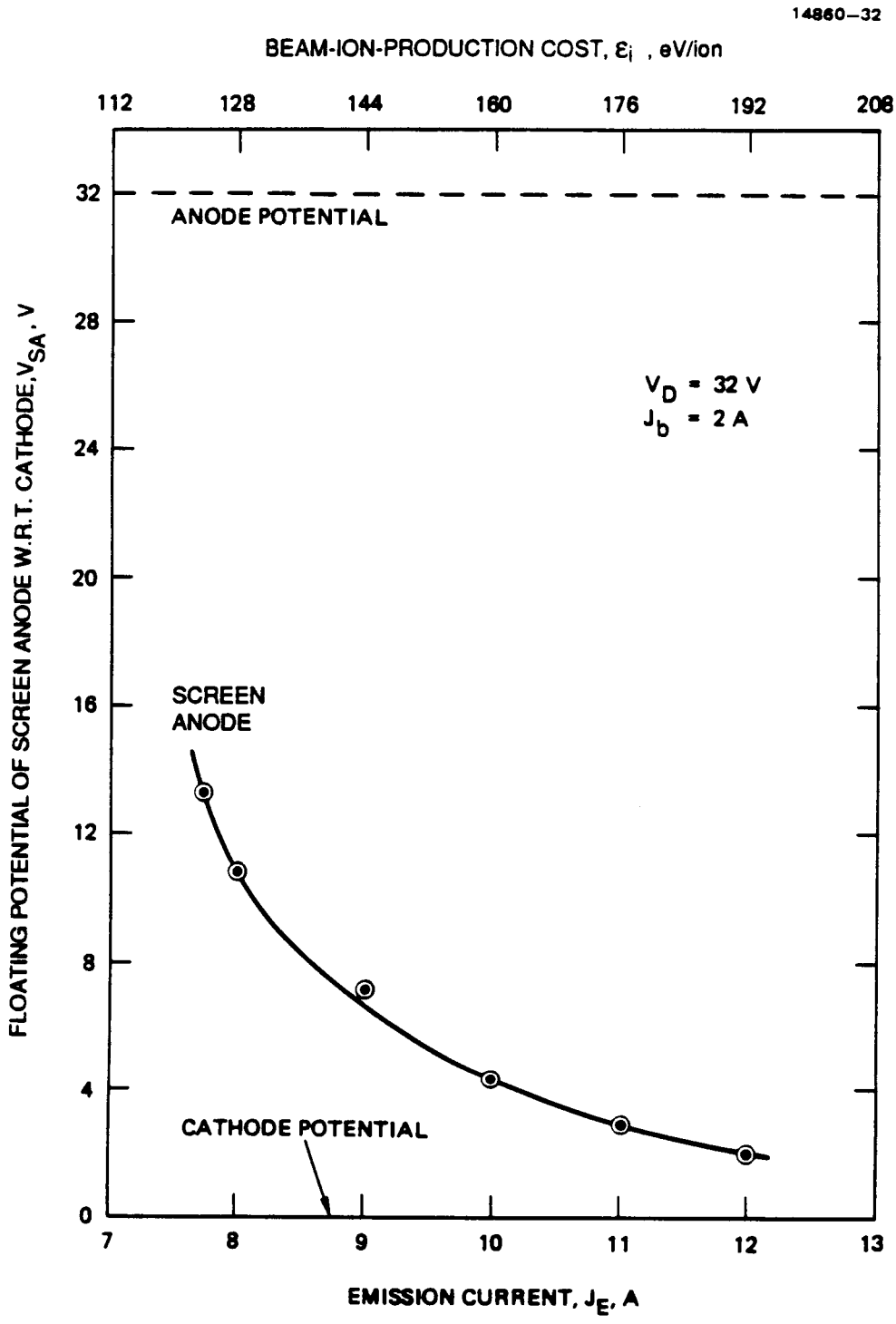

FIGURE 2-23. Floating potential of screen anode.

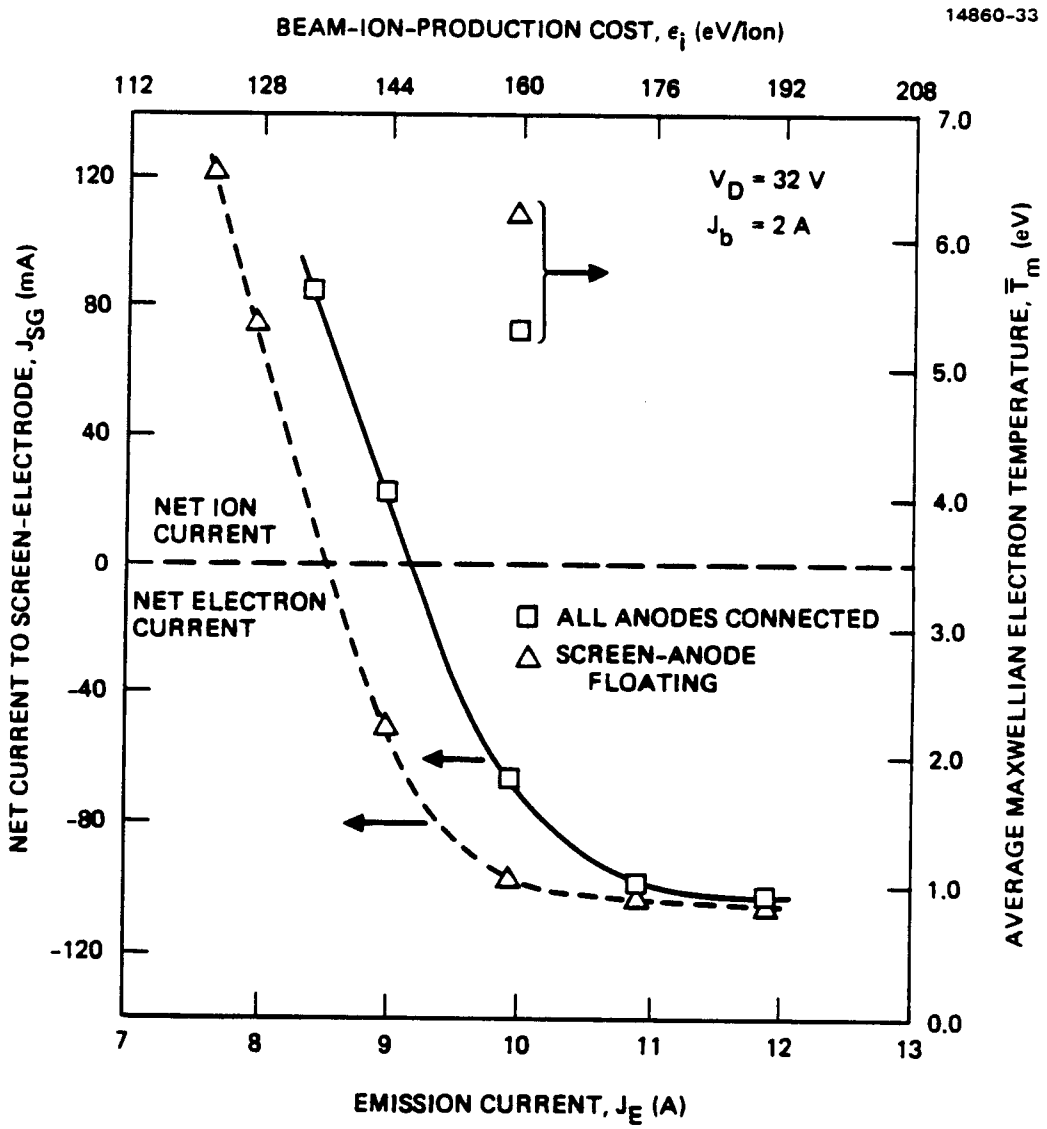

FIGURE 2-24. Correlation of electron temperature with collected screen current.

compared to the usual value of about 3.5 mA); therefore, further study of this case was ruled out. We interpret these results as indicating that the sidewall anode is the most important electrode affecting discharge-chamber processes. This finding is consistent with the results of Figure 2-13, which show that since the axial location of the sidewall anode coincides with the region of highest ion production, it collects most of the electron current.

2.4.4 Sidewall/Endwall Floating

Results presented in Figure 2-13 showed that net-ion current is collected by the plenum and sidewall/endwall. Furthermore, the results of Figure 2-14 indicated that the ion current collected by the sidewall/endwall-plenum surface is about twice as large as the electron current that is collected.

Figure 2-25 shows the variation of the sidewall/endwall floating potential with cathode-emission current. The floating potential is positive with respect to the three anode-potential magnet-ring covers because net-ion current is collected by this surface during normal operation. The effect on thruster performance of electrically floating the sidewall/endwall is presented in Figure 2-26, which shows about a 6-eV/ion reduction in the baseline beam-ion-production cost. We attribute the increased performance to the fact that the sidewall/endwall floats at a positive potential with respect to the other anode surfaces and, therefore, has a tendency to impede ion loss to that surface.

2.4.5 Sidewall/Endwall-Plenum Bias

We explored the performance improvement associated with floating the sidewall/endwall-plenum surface by biasing these surfaces positive with respect to the screen, sidewall, and endwall anodes. The power-supply arrangement shown in Figure 2-27 was used in the bias experiments. Biasing the

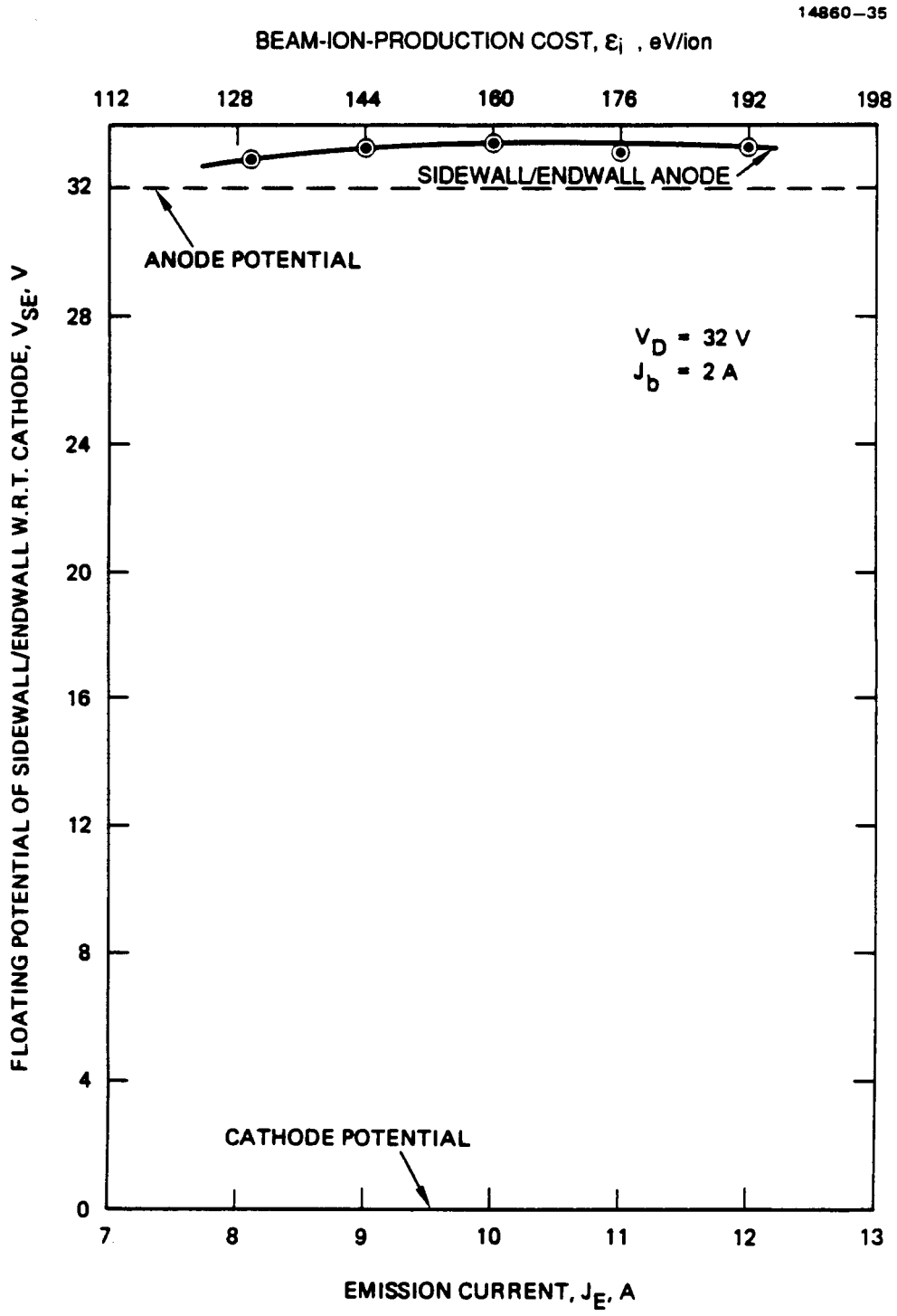

FIGURE 2-25. Floating potential of sidewall/endwall.

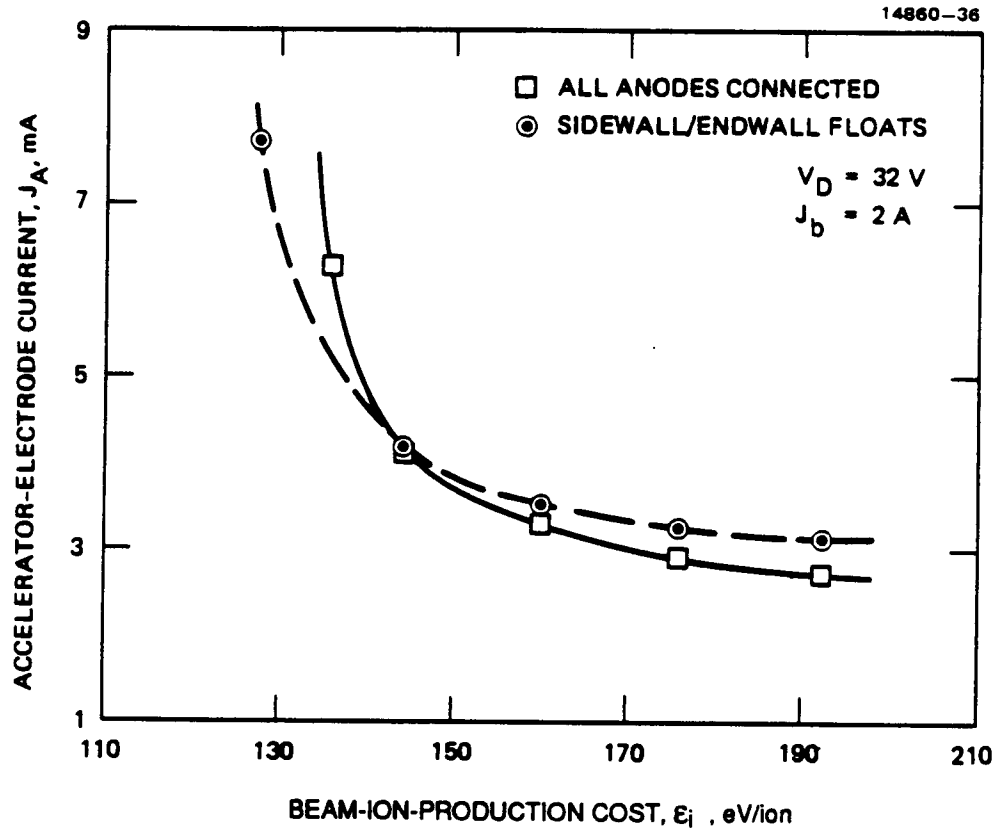

FIGURE 2-26. Variation of accel current with beam-ion-production cost; sidewall/endwall floating.

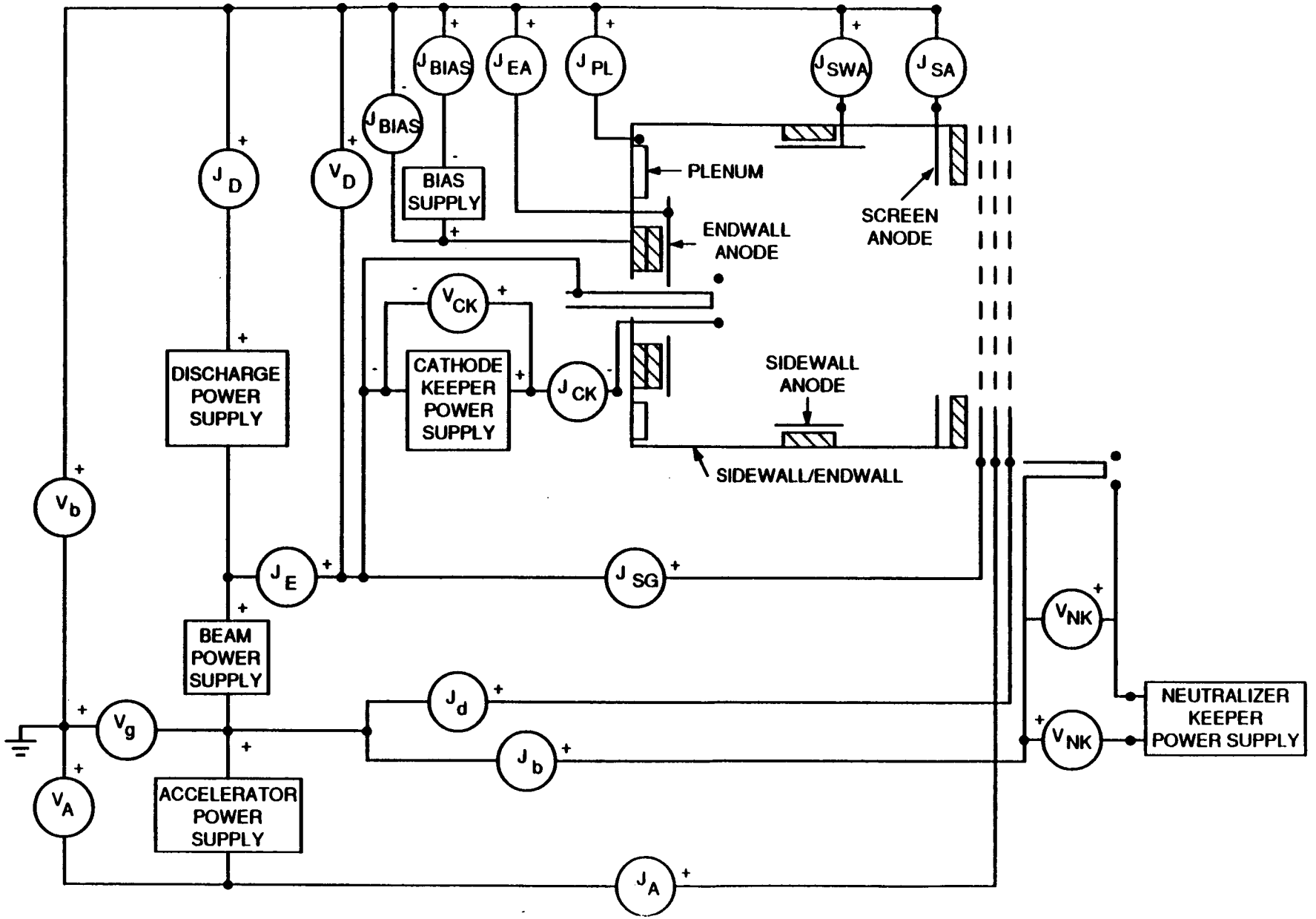

FIGURE 2-27. Schematic diagram of power supply configuration for sidewall/endwall-plenum bias experiment.

sidewall/endwall-plenum surfaces positive with respect to the anode-potential magnet-ring covers is a technique known as "electrostatic plugging" which has been used by several researchers[2-20, 2-21] to improve the performance of electron-bombardment-type ion sources.

With the currents measured as indicated in Figure 2-27, the beam-ion-production cost was calculated using the expression

$$\epsilon_i = \frac{J_E V_D}{J_b} + \frac{J_{BIAS} V_{BIAS}}{J_b} \quad . \qquad (2\text{-}1)$$

Thruster performance measurements (uncorrected for doubly-charged ions) were obtained for various bias voltages. Figure 2-28 shows the results for a bias voltage of V_{BIAS} = 4.5 V. There is a reduction in the baseline beam-ion-production cost of about 10 eV/ion and an increase in maximum discharge-propellant-utilization efficiency of about 5%, thus verifying the performance-enhancement technique. No additional performance gains were observed by increasing the bias voltage to values as high as V_{BIAS} = 11 V.

Measurements were performed to determine whether the separate effects of biasing the sidewall/endwall and additionally floating the screen anode, were additive (separately, each effect was shown to reduce the baseline beam-ion-production cost by about 10 eV/ion). Figure 2-29 shows the effect of biasing the sidewall/endwall surface 8 V positive with respect to the other anode surfaces, in addition to electrically floating the screen anode. The results indicate that the effects are not additive. For comparison purposes, the separate cases when the screen anode floats, the sidewall/endwall floats, and the case when all the anodes are connected are also shown.

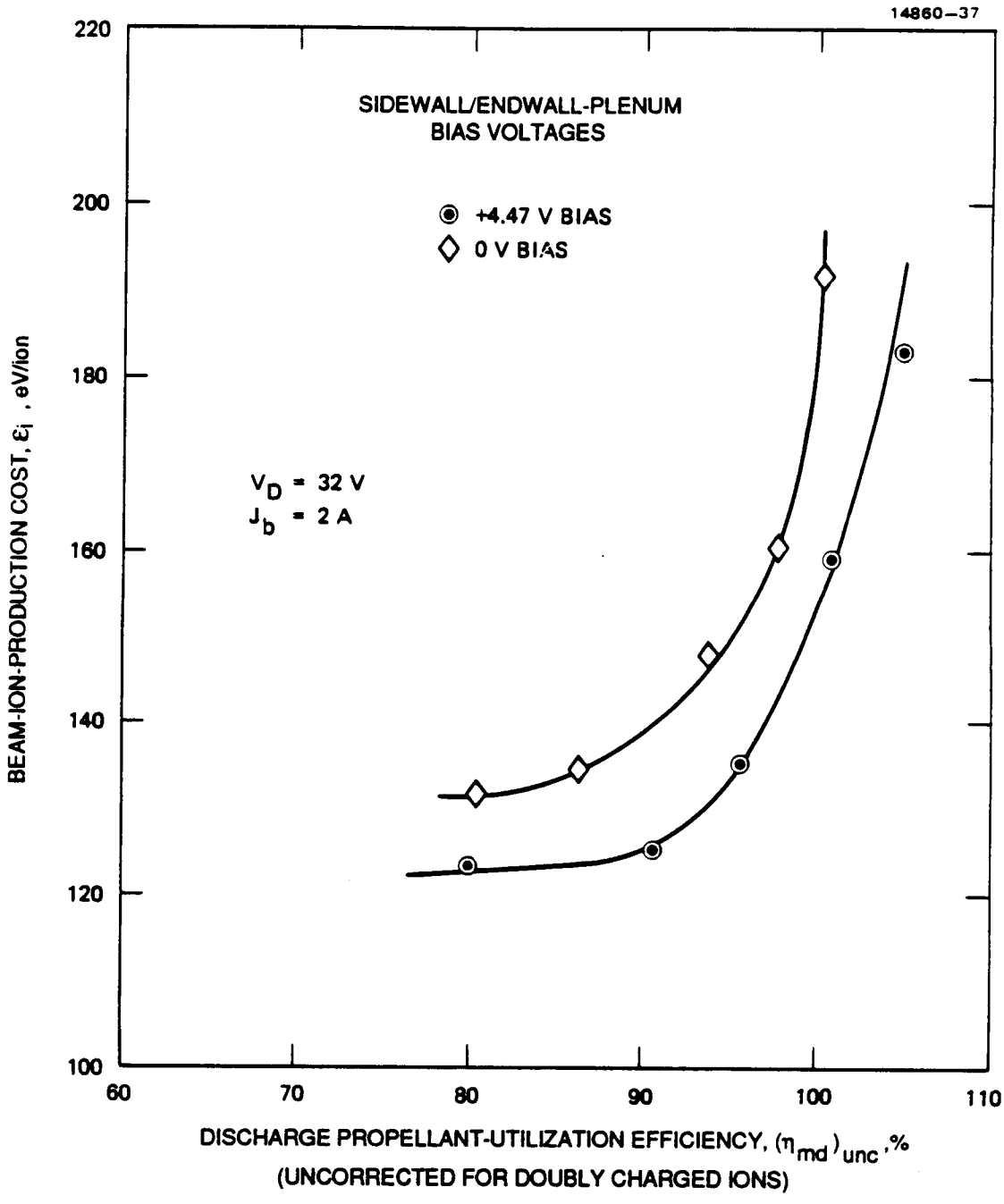

FIGURE 2-28. Performance measurements for two bias configurations of the sidewall/endwall-plenum.

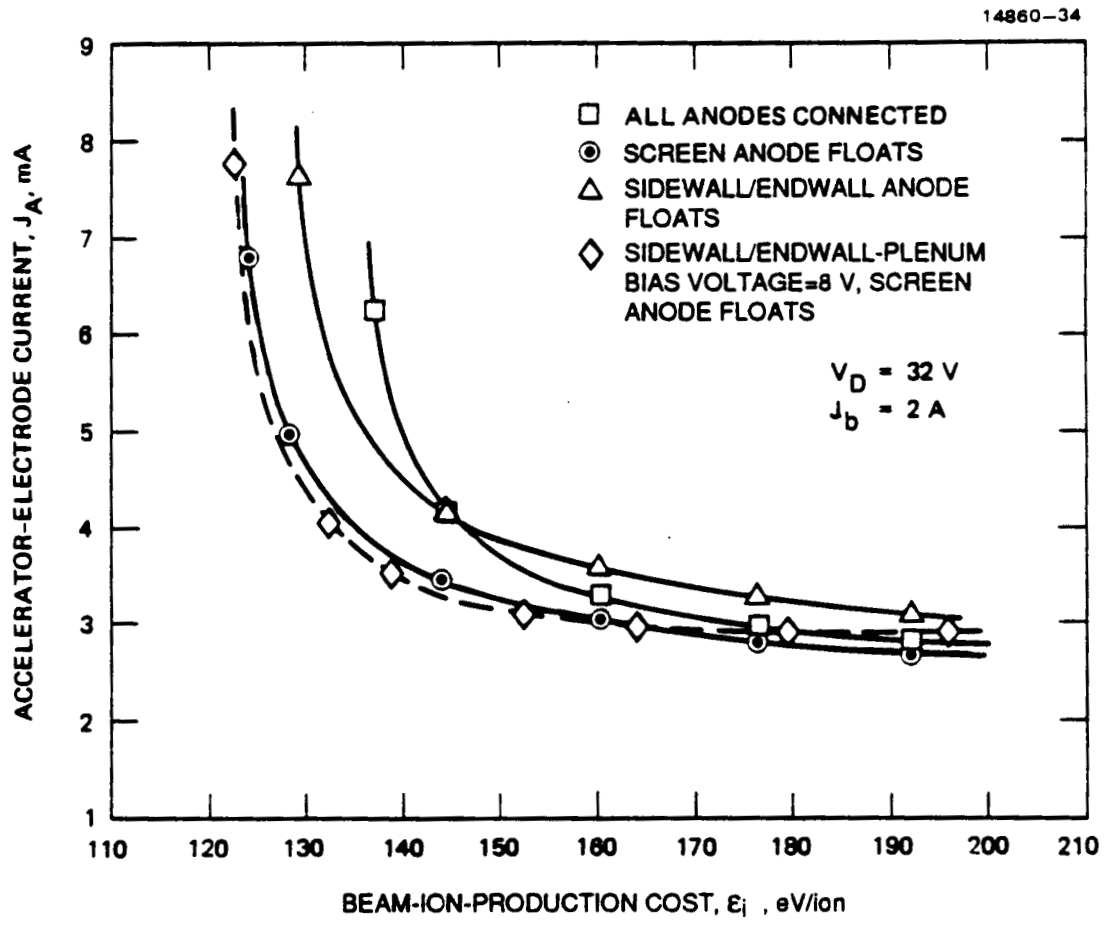

FIGURE 2-29. Performance characteristics summary.

2.5 OPERATION AT REDUCED DISCHARGE VOLTAGE

The primary wearout mechanism in ion-thruster discharge chambers is believed to be sputter erosion of the cathode-potential surfaces. Therefore, thruster operation at reduced discharge voltage could significantly alter this wearout mechanism. Because the ring-cusp thruster exhibits such a high level of performance, we explored operation at reduced discharge voltage as a means of minimizing internal sputtering and extending lifetime.

We evaluated the performance of the ring-cusp thruster operating at several different discharge voltages. The results are presented in Figure 2-30, which shows the variation of discharge-propellant-utilization efficiency (uncorrected for doubly charged ions) with discharge voltage. The results indicate that the ring-cusp thruster can be operated at a discharge voltage as low as 24 V, while maintaining a performance commensurate with that of the J-series thruster. The lifetime that can be expected with reduced discharge voltage was calculated using the screen-grid lifetime model developed under NASA Contract NAS 3-21040. Figure 2-31 shows the results of the calculations (they have been normalized to the value corresponding to a discharge voltage of V_D = 32 V), which predict a factor-of-three increase in the lifetime of the screen electrode for a discharge voltage of 24 V.

2.5.1 Sidewall/Endwall-Plenum Bias

The effect of biasing the sidewall/endwall-plenum surface to improve thruster performance was further exploited to enable superior thruster performance at reduced discharge voltage. Significant lifetime benefits have been shown to be realized by reducing the discharge voltage down to the 24-26 V range, with some loss in performance. Therefore, we investigated biasing the sidewall/endwall surface as a means of regaining thruster performance at reduced discharge voltage.

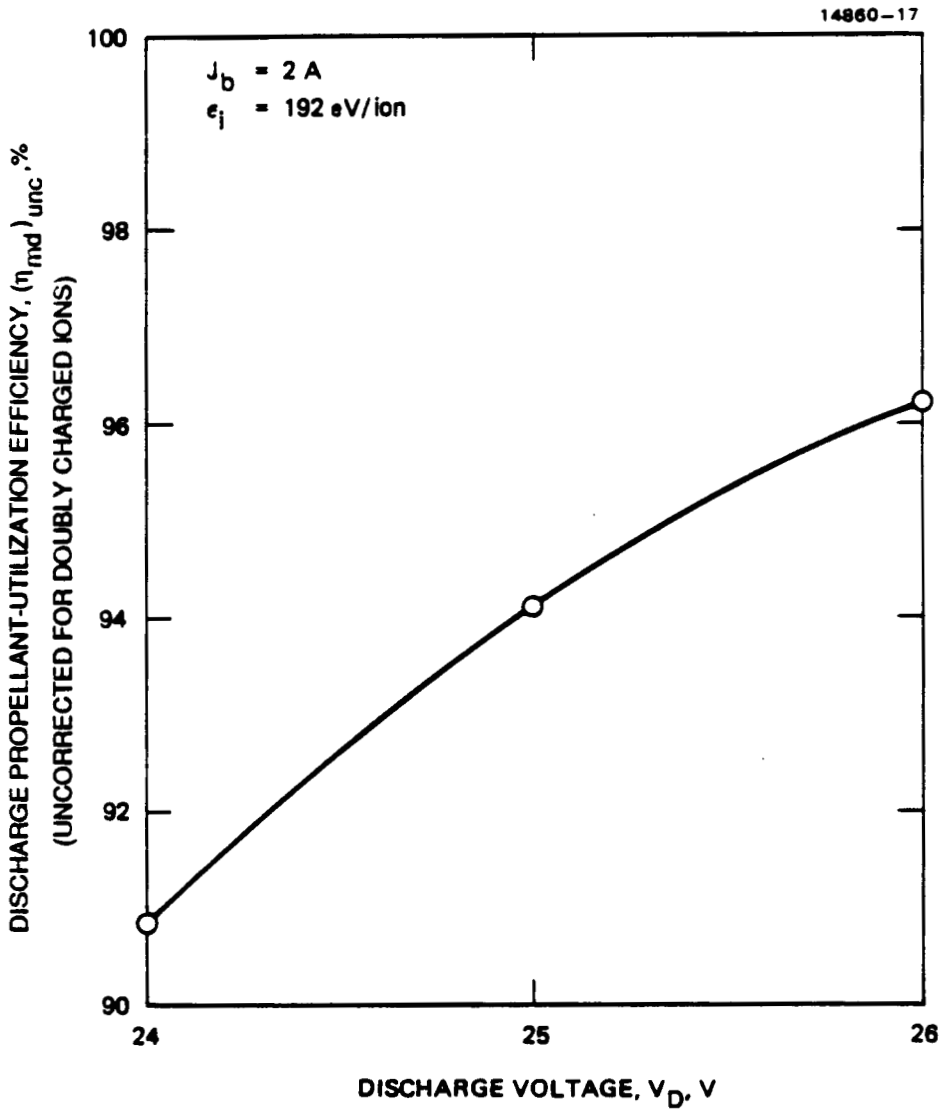

FIGURE 2-30. Performance of ring cusp thruster at several different discharge voltages.

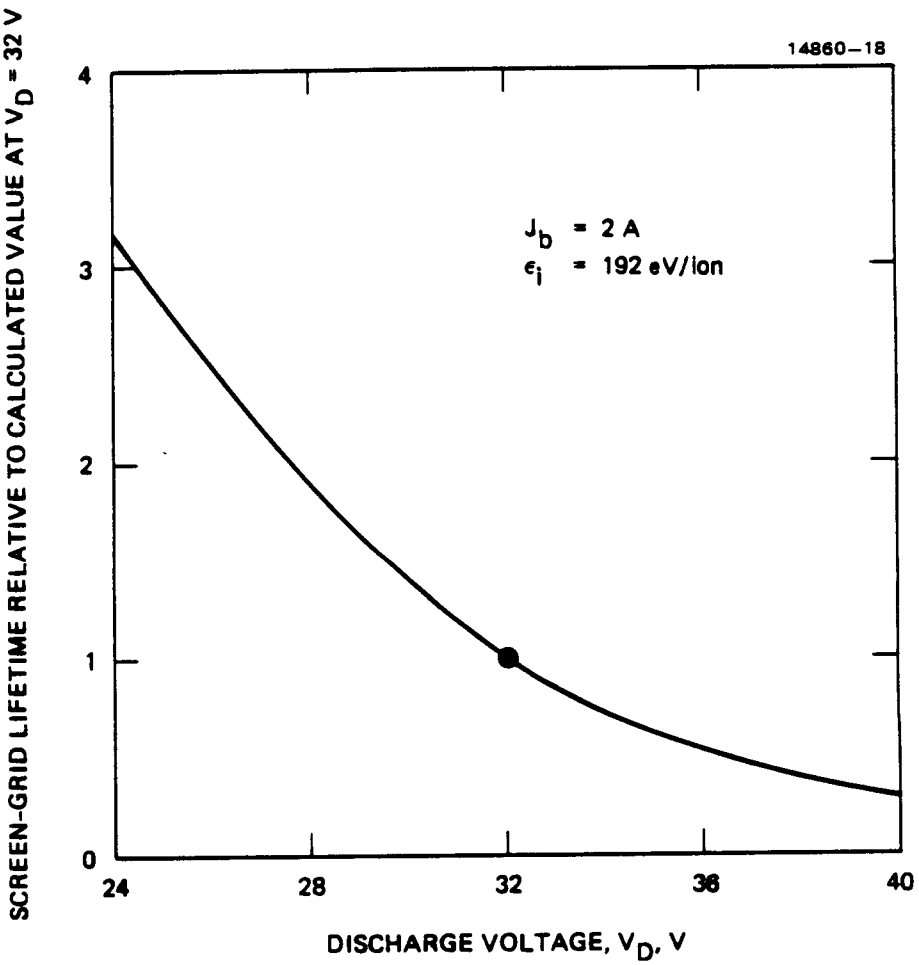

FIGURE 2-31. Variation of normalized screen grid lifetime with discharge voltage.

Figure 2-32 shows the variation of accelerator-electrode current with beam-ion-production cost for different discharge and sidewall/endwall-plenum bias voltages. The results demonstrate the performance enhancement that can be achieved, and they suggest that the discharge voltage can be reduced to as low as 26 V with only a slight penalty in beam-ion-production cost and discharge-propellant-utilization efficiency. This could result in a substantial increase in chamber lifetime (at nearly the same efficiency), as a result of reduced ion-sputtering.

Using our optical-spectroscopy setup,[2-22] molybdenum-line-intensity measurements (for fixed plasma conditions, the molybdenum line intensity is proportional to the sputtering rate of the screen electrode) were obtained to assess the lifetime impact of thruster operation at reduced discharge voltage (with a bias applied to the sidewall/endwall-plenum). Two operating modes were studied and compared; 32-V discharge with no bias on the sidewall/endwall-plenum, and 26-V discharge with 6-V bias on the sidewall/endwall-plenum. Figure 2-33 shows the measured variation of molybdenum-line-intensity and accelerator-electrode current with beam-ion-production cost for the two modes of operation. The molybdenum line intensity for the 26-V discharge, 6-V bias mode is 2 to 3 times less than it is for the 32-V, unbiased mode. On the basis of the screen-electrode lifetime predictions shown previously in Figure 2-31, the factor-of-two reduction in the molybdenum line intensity for the 26-V, 6-V bias mode is consistent with an increase in screen-electrode lifetime.

We verified that thruster operation at V_D = 26 V with a 6-V bias on the sidewall/endwall-plenum resulted in reduced plasma potential at the screen electrode, by probing the plasma on thruster centerline just upstream of the screen electrode. The results are presented in Figure 2-34, verifying that the plasma potential is reduced by about 5 V. This result is consistent with the observed decrease in molybdenum-line-intensity measurements presented in Figure 2-33.

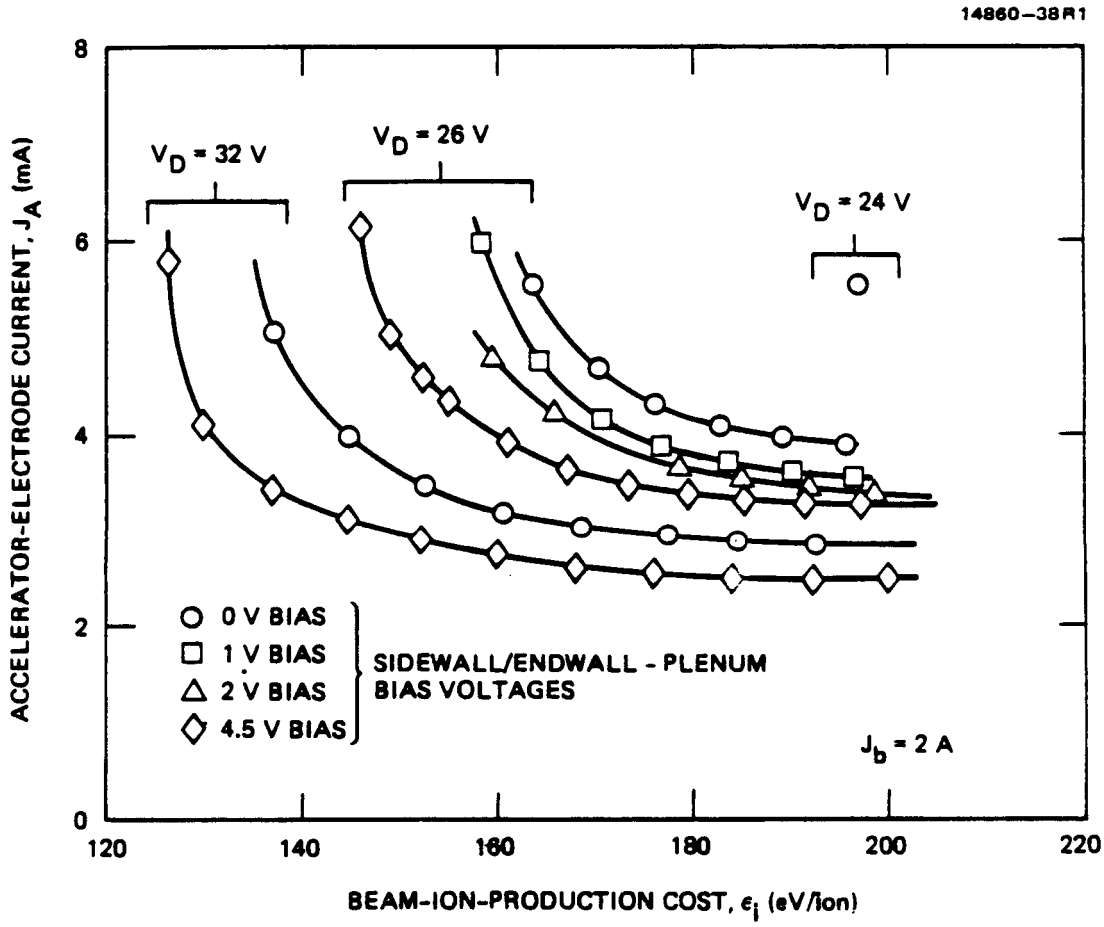

FIGURE 2-32. Variation of accel current with beam-ion production cost for different discharge voltages and sidewall/endwall-plenum bias voltages.

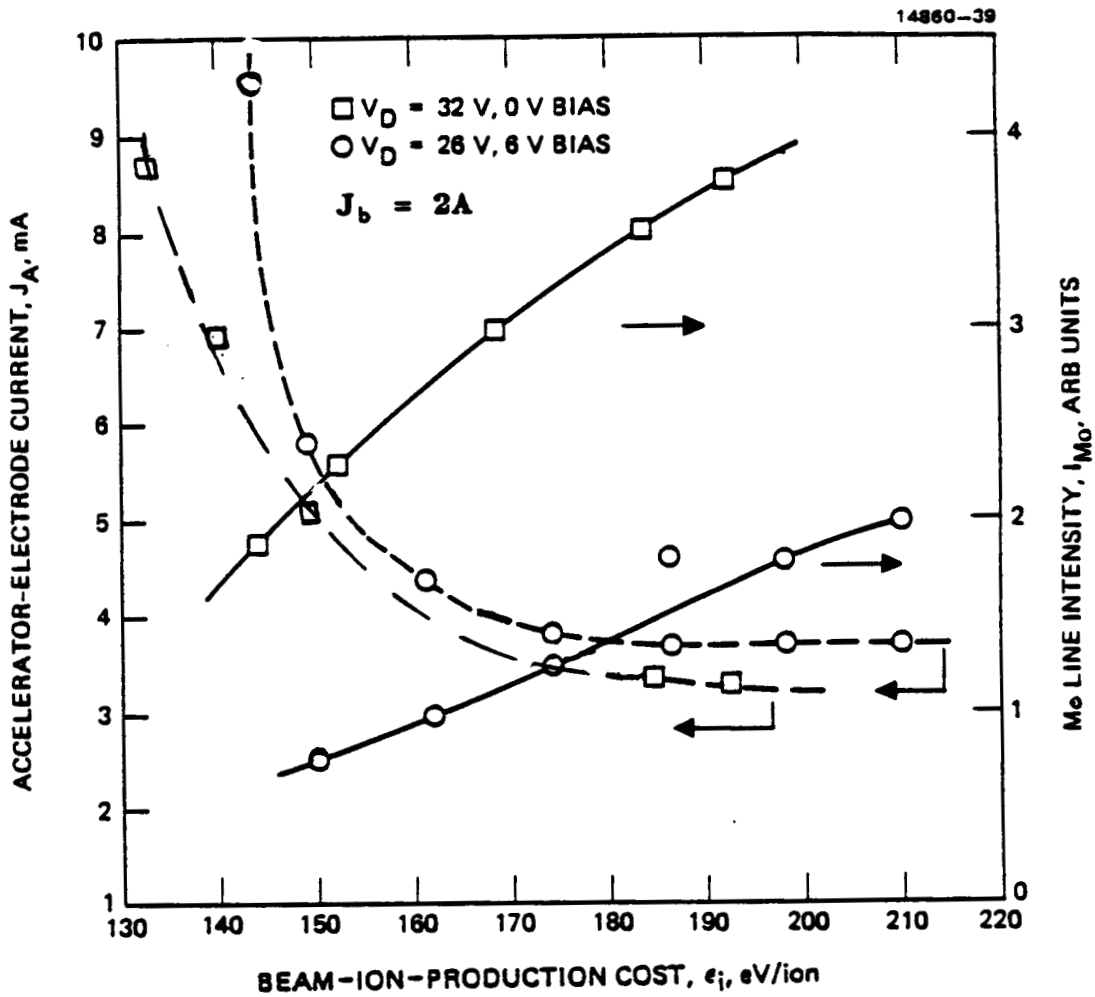

FIGURE 2-33. Variation of accel current and molybdenum line intensity measurements with beam-ion-production cost for two values of discharge voltage and sidewall/endwall-plenum bias voltage.

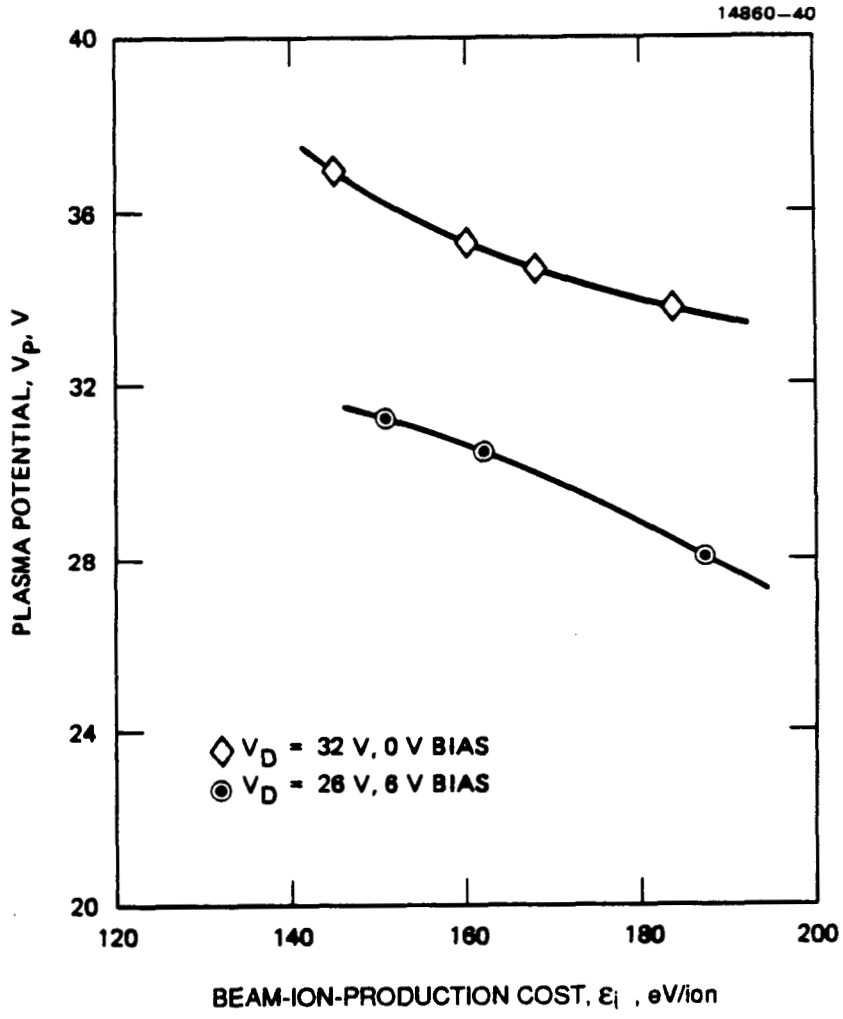

FIGURE 2-34. Variation of measured plasma potential with beam-ion-production cost for two values of discharge voltage and sidewall/endwall-plenum bias voltage. Plasma potential measurements taken on thruster centerline at screen electrode.

2.6 CATHODE EROSION

A life limitation of the J-series thruster is believed to be baffle/pole-piece erosion and subsequent deposition of material onto the cathode keeper and keeper support. The ring-cusp thruster design eliminates the cathode baffle/pole-piece assembly and positions the cathode directly in the discharge plasma.

The cathode used in the ring-cusp and J-series thrusters has a 0.76-mm-diameter orifice made of W-2%Th. Figure 2-35 shows a photograph of the cathode orifice plate after the 694 hours of ring-cusp thruster operation that were accumulated under this and a companion study.[2-4] The photograph suggests that for ring-cusp thrusters operating with mercury propellant, an exposed cathode with a 0.76-mm-diameter orifice experiences no significant erosion.

An attempt was made to incorporate the strong magnetic field near the cathode orifice of the ring-cusp thruster into a J-series-type thruster. The intent was to explore ways of improving the performance and lifetime of the J-series thruster with minimal modification of its discharge chamber. An electrically equivalent J-series thruster (S/N 301-J) was modified to produce a "hybrid" ring-cusp configuration. The performance of this thruster was substandard, and, therefore, no further measurements or modifications were performed. A summary of the results of this investigation is presented in Appendix C.

2.7 CATHODE LOCATION

The effect of the cathode location in the ring-cusp discharge chamber was explored by using the movable-cathode arrangement that was designed and fabricated under NASA Contract NAS 3-21943. Figure 2-36 shows the variation of accelerator-electrode current with cathode position. These results show there is little effect of cathode location, unless it is located near the endwall. Figure 2-36 also shows the variation of axial

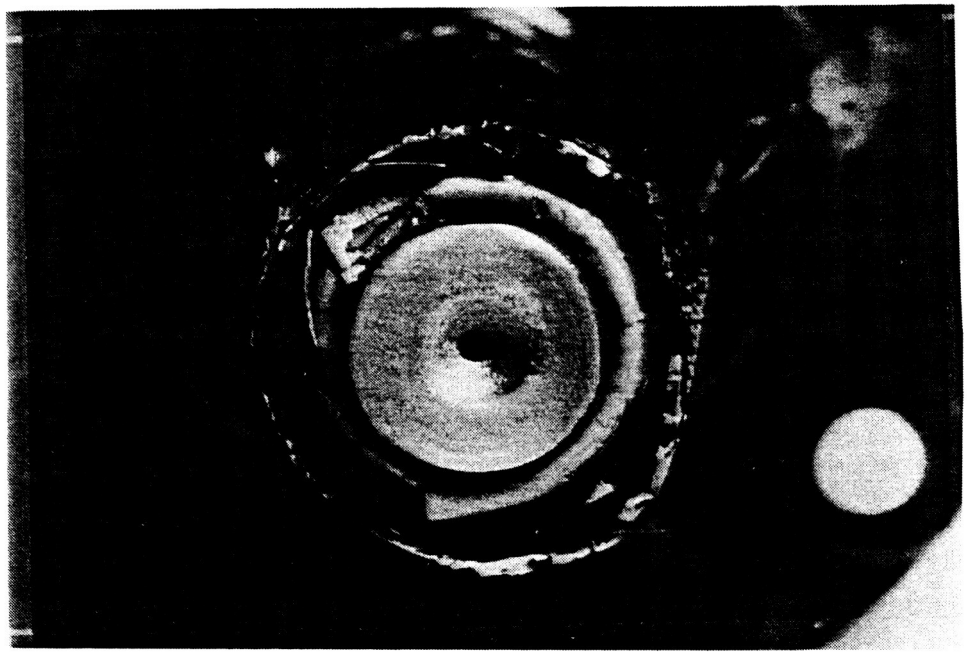

FIGURE 2-35. Photograph of cathode orifice after 694 hours of operation in the ring-cusp thruster.

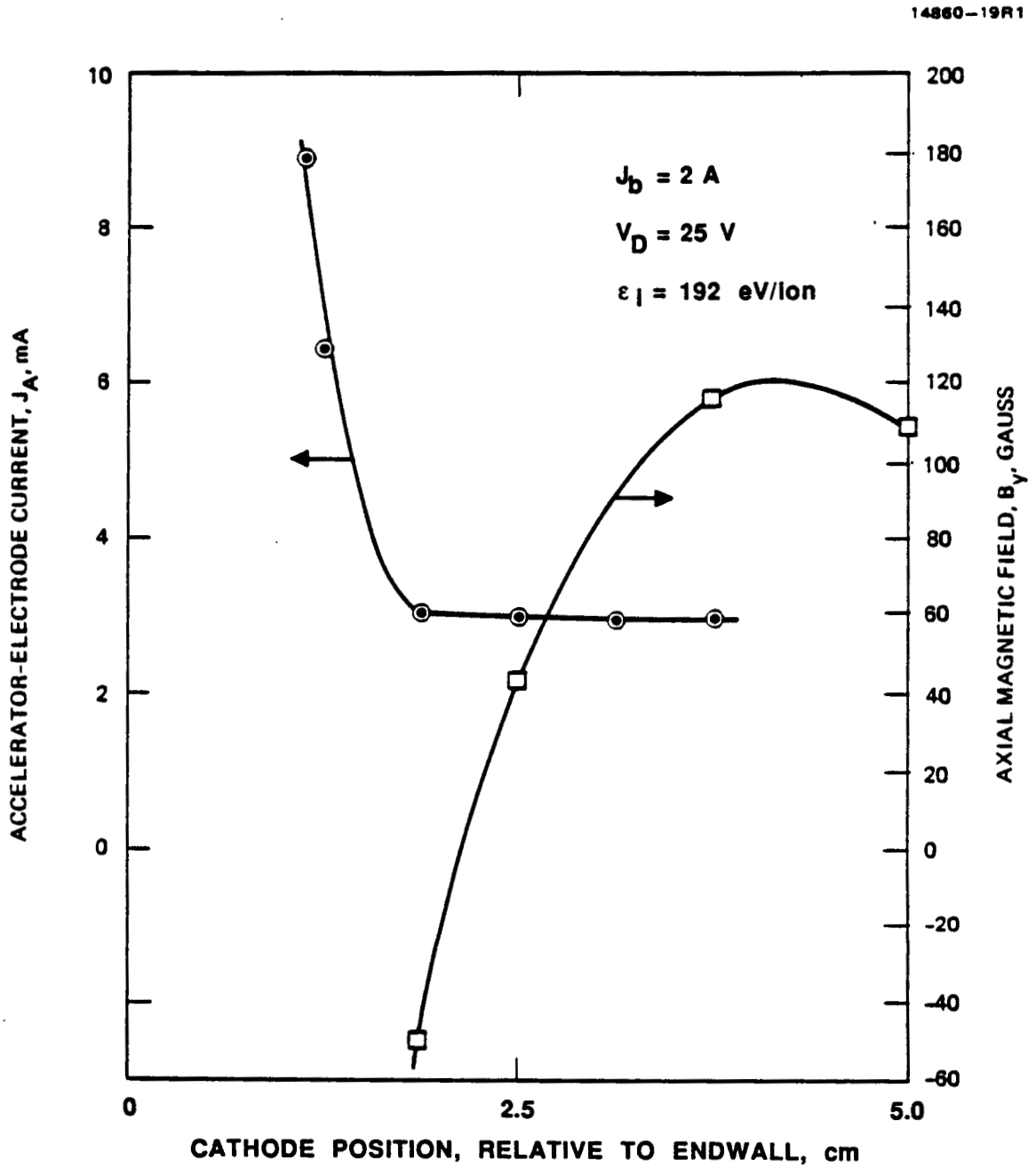

FIGURE 2-36. Variation of accel current with cathode position with respect to axial magnetic field strength.

magnetic field at the location of the cathode orifice. The two curves suggest that the magnitude of the field at the cathode orifice has little effect on performance, as long as the cathode is located downstream of the field-reversal point. The flat region of the accelerator-electrode-current variation suggests that no improvement in performance is to be expected as a result of positioning the cathode further into the discharge chamber.

REFERENCES

2-1. Sovey, J.S, "Improved Ion-Containment Using a Ring-Cusp Ion Thruster," AIAA Paper No. 82-1928, New Orleans, Louisiana, November 1982.

2-2. Lovell, R.R. et al., "30-cm Ion Thruster Subsystem Design Manual," NASA Technical Memorandum 79191, National Aeronautics and Space Administration, Lewis Research Center, Cleveland, Ohio, June 1979.

2-3. Poeschel, R.L., "Retrofit and Acceptance Test of 30 cm Ion Thrusters," NASA CR-165259, Hughes Research Laboratories, Malibu, California, June 1981.

2-4. Beattie, J.R. and Matossian, J.N., "Inert Gas Thruster Technology," Final Report NAS 3-23860, Hughes Research Laboratories, Malibu, Calif.

2-5. Beattie, J.R. and Kami, S., "Advanced Technology 30-cm-Diameter Ion Thruster," AIAA Paper No. 82-1910, New Orleans, Louisiana, November 1982.

2-6. Beattie, J.R., "Extended Performance Technology Study; 30-cm Thruster," Final Report NAS 3-21943, Hughes Research Laboratories, June 1983.

2-7. Beattie, J.R. and Poeschel, R.L., "Ring-Cusp Ion Thrusters," AIAA Paper No. IEPC 84-71, Tokyo, 1984.

2-8. Leung, K.N., Hershkowitz, N., and Mackenzie, K.R., "Plasma Confinement by Localized Cusps," Physics of Fluids, Vol. 19, No. 7, pp. 1045-1053, July 1976.

2-9. Knorr, G. and Merlino, R.L., "The Role of Fast Electrons for the Confinement of Plasma by Magnetic Cusps," Plasma Phys. and Controlled Fusion, Vol. 26, No. 2, pp. 433-442, 1984.

2-10. Hershkowitz, N., Leung, K.N., and Romeser, T., "Plasma Leakage Through a Low-β Line Cusp," Phys. Rev. Letters, Vol. 35, pp. 277-280, August 1975.

2-11. Masek, T.D., "Plasma Properties and Performance of Mercury Ion Thrusters," AIAA Paper No. 69-256, Williamsburg, Virginia, March 1969.

2-12. Kaufman, H.R., "Ion Thruster Propellant Utilization," Ph.D Thesis, Colorado State University, Fort Collins, Colorado, June 1971.

2-13. Kaufman, H.R., Robinson, R.S., and Frisa, L.E., "Ion Flow Experiments in a Multipole Discharge Chamber," AIAA Journal, Vol. 22, No. 11, pp. 1544-1549, November 1984.

2-14. Brophy, J.R. and Wilbur, P.J., "The Flexible Magnetic Field Thruster," J. Spacecraft and Rockets, Vol. 22, No. 6, pp. 611-618, November-December 1983.

2-15. Matossian, J.N. and Beattie, J.R. "Properties of Plasmas in Electron Bombardment Ion Thrusters," AIAA Paper No. 87-1076, Colorado Springs, Colorado, May 1987.

2-16. Beattie, J.R. and Wilbur, P.J., "Cusped Magnetic Field Mercury Ion Thruster," J. Spacecraft and Rockets", Vol. 14, No. 12, pp. 747-755, December 1977.

2-17. Longhurst, G., "Prediction of Plasma Properties in Mercury Ion Thrusters," NASA CR-159448, Colorado State University, Fort Collins, Colorado, December 1978.

2-18. Holmes, A.J.T., "Role of Anode Area in the Behaviour of Magnetic Multipole Discharges," Rev. Sci. Instruments, Vol. 52, No. 12, pp. 1814-1823, December 1981.

2-19. Goebel, D.M., "Ion Source Discharge Performance and Stability," Phys. Fluids, Vol. 25, No. 6, pp. 1093-1102, June 1982.

2-20. Ehlers, K.W. and Leung, K.N., "Increasing the Efficiency of a Multicusp Ion-Source," Rev. Sci. Instruments, Vol. 53, No. 9, pp. 1429-1433, September 1982.

2-21. Hershkowitz, N., Hendricks, K., and Carpenter, R.T., "Electrostatic Plugging of Leaks in a Multipole Device," J. Appl. Phys., Vol. 53, No. 6, pp. 4105-4112, June 1982.

2-22 Poeschel, R.L. and Beattie, J.R., "Primary Electric Propulsion Technology Study," NASA CR-159688, Hughes Research Laboratories, Malibu, California, November 1979.

SECTION 3

ION-OPTICS TECHNOLOGY

Earth-orbital applications of ion-propulsion technology may benefit from thruster operation at a lower specific impulse than the nominal design point of the state-of-the-art J-series thruster ($I_{sp} \simeq 3000$ sec). Applications such as North-South stationkeeping of geosynchronous communications satellites may also require cyclic operation, where the typical thruster duty cycle might be 1 hour per day. These operating requirements translate into new design requirements for the ion-extraction assembly; namely, the use of a three-grid electrode design and a low-thermal-mass electrode-mounting arrangement. Substantial progress in meeting these requirements was made under the present program, along with improvements to the procedures that have been used in the past for fabricating and assembling the J-series ion-extraction assemblies.

3.1 THERMOMECHANICAL MODELLING

The ion-extraction assembly of the J-series thruster utilizes the relatively massive mounting-ring arrangement shown in Figure 3-1(a) for supporting the electrodes. Excellent steady-state performance characteristics have been demonstrated with this design for operation to beam currents at least as high as $J_b = 4$ A. However, under cyclic operating conditions there is some concern that the relatively poor thermal contact between the edge of the electrodes and their stiffening rings could result in unacceptable transient temperature distributions. The consequent aperture misalignment resulting from excessive nonuniformities in the temperature distributions could lead to undesirable beamlet vectoring, possibly causing direct impingement of ions onto the accelerator electrode.

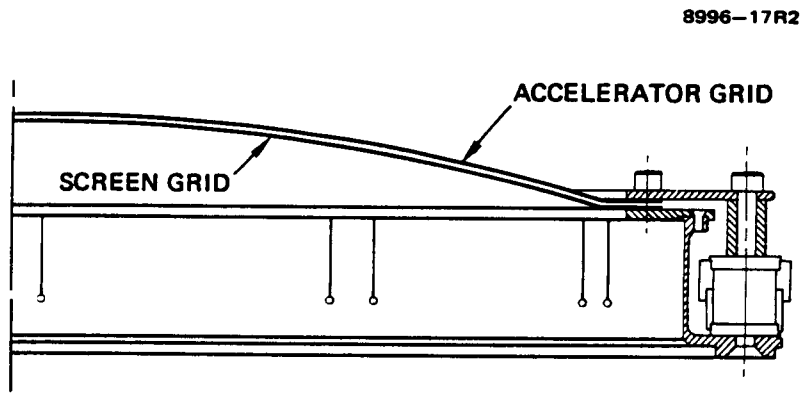

a. J-SERIES DESIGN ("STANDARD")

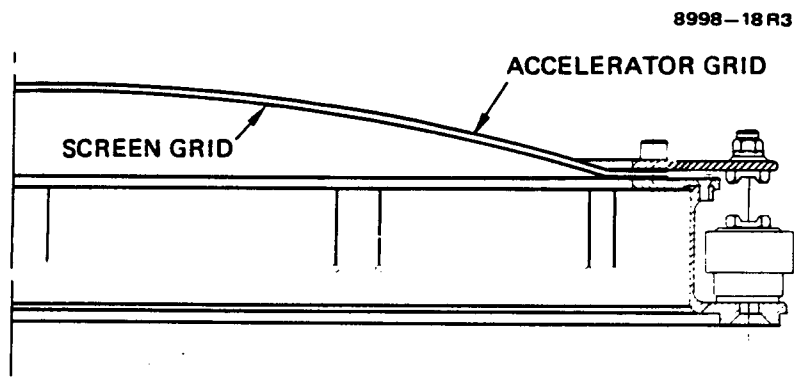

b. ADVANCED TECHNOLOGY 2-GRID DESIGN

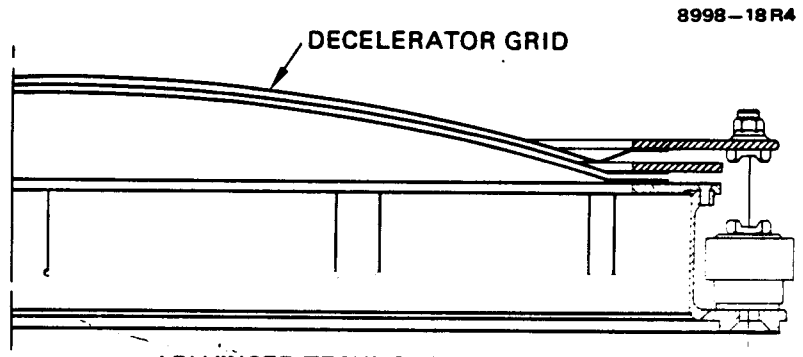

c. ADVANCED TECHNOLOGY 3-GRID DESIGN

FIGURE 3-1. Rigid and "flexible" ion-optics mountings.

The usefulness of a thermomechanical model[3-1] of the J-series ion-extraction assembly was demonstrated under NASA Contract NAS 3-21040. A finite-element model (designated as EASE2) of the optics assembly (based on measured temperature distributions) indicated that under thermal loading the rigid post-type mounting of the accel stiffening ring could lead to significant deformation of the grid and a change in the interelectrode spacing. The same model was used to show that nearly uniform grid spacing could be achieved by using the single "flexible" supports shown in Figure 3-1(b) and 3-1(c) to mount the electrode-stiffening rings. Both two- and three-grid ion-extraction assemblies that employ this design have been successfully fabricated and tested under NASA Contracts NAS 3-21943[3-2] and NAS 3-22474.[3-3]

Under the present program, we extended the modelling initiated under NASA Contract NAS 3-21040 to examine the effects of eliminating the stiffening rings of a "conventional" mounting arrangement and mounting both the screen and accel electrodes to thin thermally compliant structural supports.

The simplified electrode-mounting arrangement of Figure 3-2 eliminates the large thermal mass of the J-series stiffening rings by incorporating a "dog leg" bend into the planar edge of the electrodes to provide the required stiffness. The electrodes are mounted onto flexible box-type members that can accommodate thermal expansion in the radial direction, while providing excellent rigidity in the transverse direction. If successfully demonstrated, we predicted that the low-thermal-mass design would improve the reliability of the J-series ion-extraction assembly, making it suitable for cyclic operation.

We analyzed the simplified structure of Figure 3-2 and showed that:

- The simplified mounting structure allows the electrodes to be decoupled for analysis purposes, so that essentially the same model can be used to evaluate all three grids (by using separate load cases)

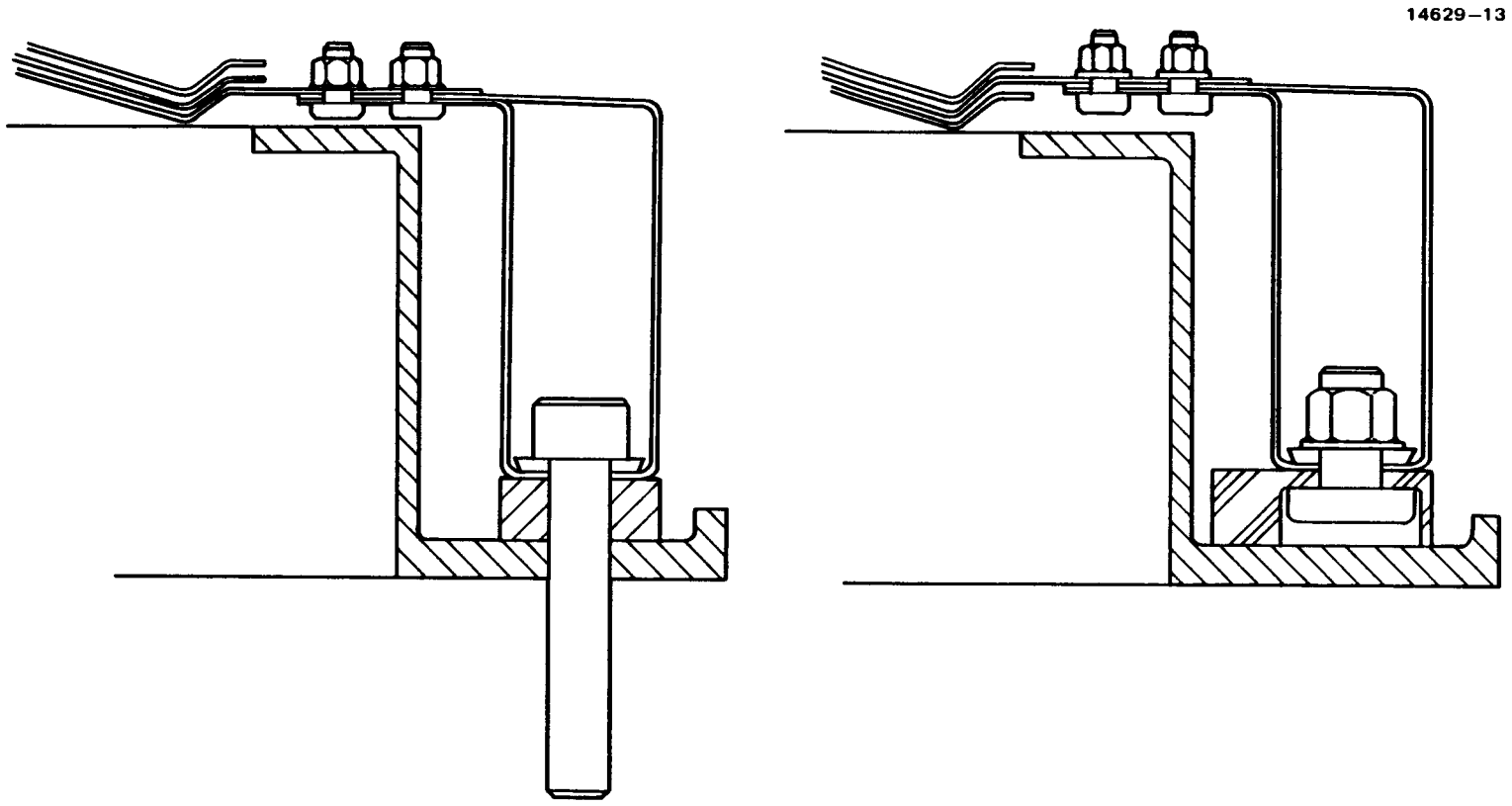

a. SCREEN SUPPORT

b. ACCEL SUPPORT

FIGURE 3-2. Simplified ion-optics mounting.

- The thin structural members that support the electrodes are not rigid enough to inhibit radial expansion, resulting in low stresses in the electrodes
- The thickness of the flexure causes the most significant change in stress
- The temperature distributions in the flexures are critical in determining the calculated deformations of the electrodes.

A more detailed discussion of the analysis results are presented in the sections that follow.

Several finite-element models (shown in Figure 3-3) were considered in performing the EASE2 analysis. The first model (Model 1) resulted in several points of inflection that could not possibly exist for the specified constraints. This discrepancy was attributed to the large aspect ratio (length-to-width ratio of the mesh, as indicated in the example of Figure 3-4) of the elements employed in the model and was corrected by increasing the number of nodes along the shell (reducing the mesh dimension). This modification to the original model resulted in a smooth profile, as shown for Models 2 through 6.

In Models 2 thru 6, the Ti mounting plate was eliminated, so that the base of the double flexmember support remained fixed. This requires a 60% increase in the deflection beyond that which the flexmembers would normally experience with a mounting ring undergoing thermal expansion (as in the other models), with the major effect being a direct increase in the stress in the flexmember. The effects produced by the various models shown in Figure 3-3 are summarized below, with the results of Model 2 taken as the baseline for comparison. The highest stress on the electrode was calculated to be about 20 MPa (2.9×10^3 psi) (radial) and occurs near the flex support.

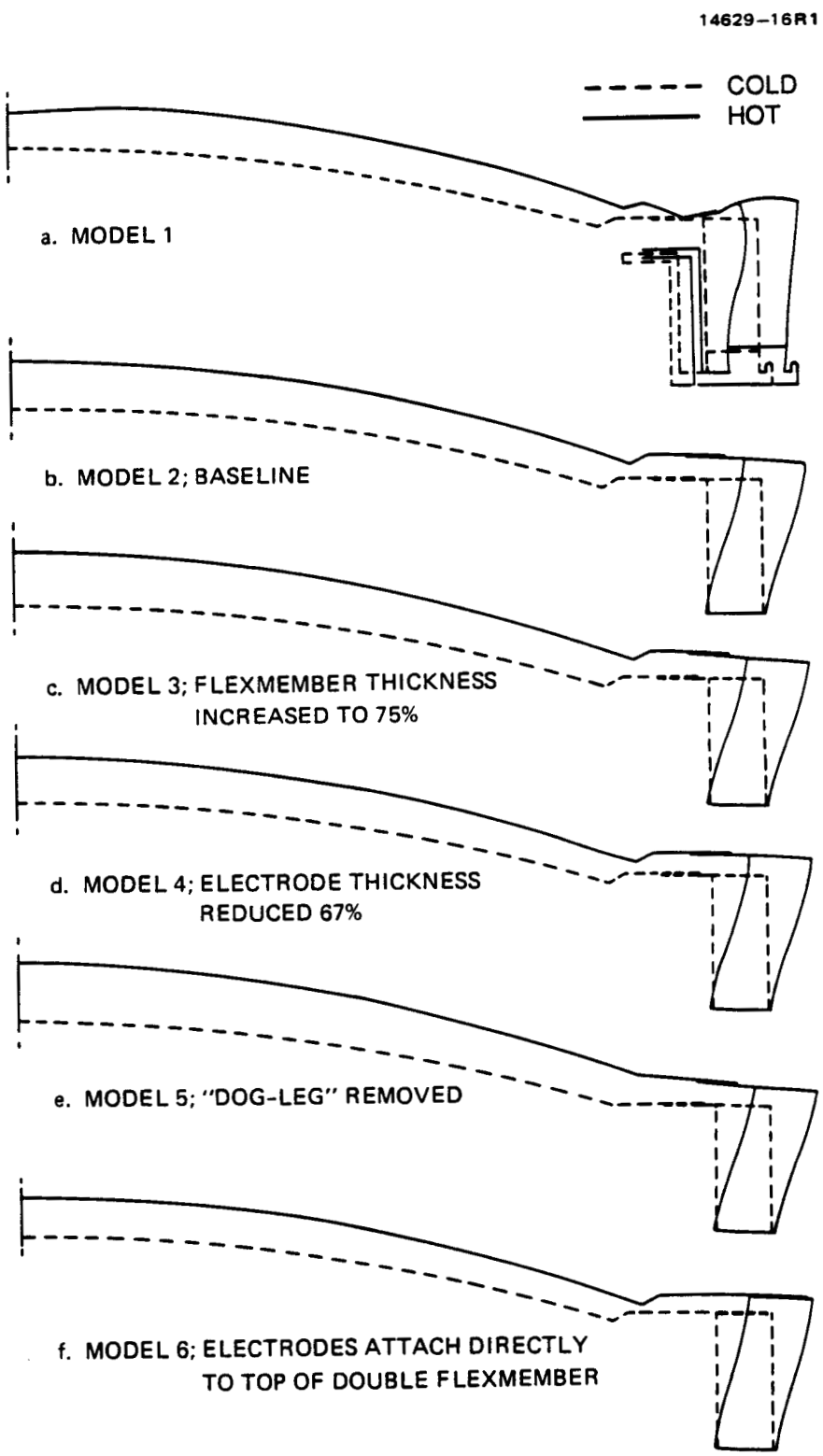

FIGURE 3-3. Finite-element models and calculated deformations.

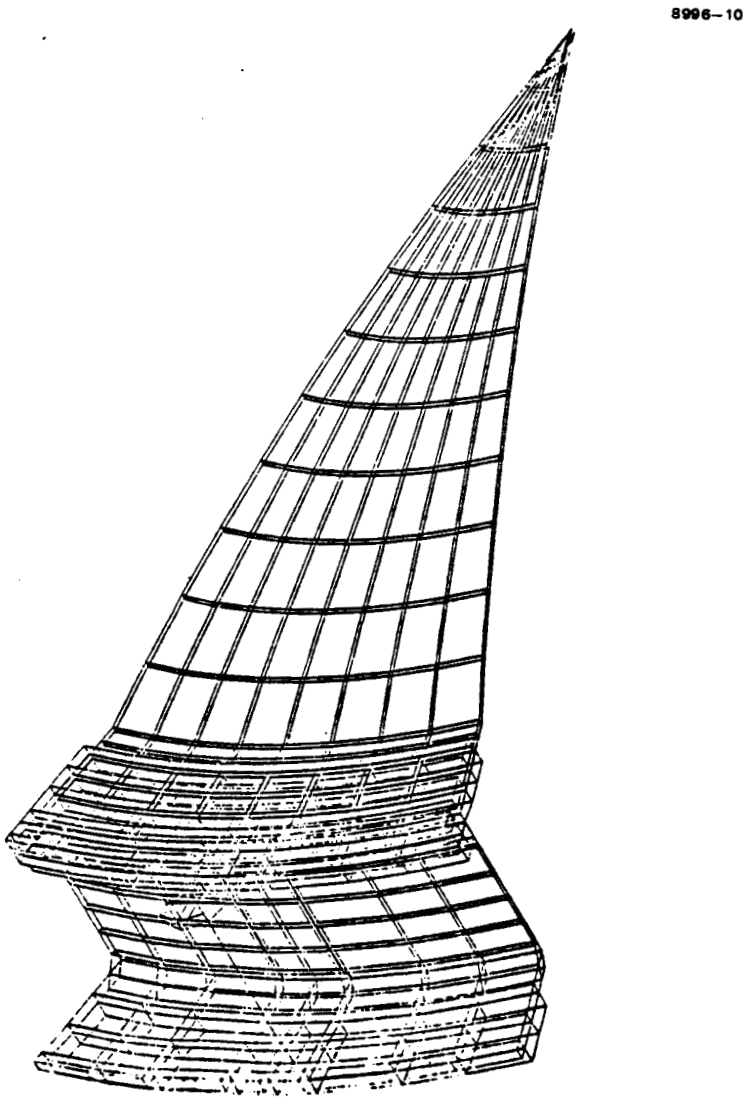

FIGURE 3-4. Finite elements employed in the stress-analysis model.

3.1.1 Effect of the Flexmember Thickness

Model 3 employed a flexmember with a thickness of 0.76 mm, or 75% increase over that used for Model 2. There was no significant change in the calculated radial displacements. However, the stiffer arm extending from the double flexmember, combined with differential thermal expansion between the inner and outer flexmembers, causes the arm to tilt upwards. This produces a 7.5% increase in the vertical displacement at the center of the electrode.

3.1.2 Effect of Electrode Thickness

Model 4 employed a 67% reduction in the thickness of the electrode within the aperture boundary, and resulted in a point of inflection on the shell curvature inboard of the location of the aperture boundary. Outboard of this point the slopes to and through the "dog leg" appear to be identical to those corresponding to the baseline configuration. The use of a thinner material as a means of simulating the perforated electrode geometry is probably more representative of the true deflections than the smooth profile predicted by Model 2.

3.1.3 Effect of Removing the Dog Leg

Model 5 has flat flanges at the edges of the electrodes, with the "dog leg" removed. Differential thermal expansion between the inside and outside flexmembers causes the extended arm to tilt upward, and the compliance of the flat flange to the upward tilt causes a 16% increase in vertical displacement at the center of the electrode. The flexmembers of Model 5 are 0.43 mm thick and undergo a 16% increase in vertical displacement, compared to the 0.76-mm-thick flexmembers of Model 3, which have a calculated strain of only about 7%.

3.1.4 Effect of Electrode Diameter

The extended arm of the double flexmember support was removed in Model 6. This configuration was modelled by leaving the flexmember at the same location as in the previous models and enlarging the electrode flange to join the flexmember. This, in effect, presented a more compliant member between the "dog leg" and the flexmember supports (as in Model 5). In a practical design, the support would be located inboard, as close to the "dog leg" as the thruster shell structure would allow. This would result in deflections approaching, but (because of the elimination of the arm extension) not exceeding those of the baseline model. The net result predicted by Model 6 is a 19% decrease in the vertical displacement at the center of the electrode.

Thermal expansion of the flex member support is included in all of the deflections indicated above. For Model 2, thermal expansion accounted for 38.5% of the vertical displacement at the screen center. Thermal expansion of the inboard flexmembers was approximately 0.2 mm for Models 2-6.

The simplified electrode mount shown in Figure 3-2 was fabricated under the present program. Test results obtained with this promising new design will be obtained under NASA Contract NAS 3-23860.

3.2 ELECTRODE-FABRICATION TECHNOLOGY

Several improvements to grid-fabrication procedures were identified under NASA Contract NAS 3-23774. Under the present program, we continued the earlier work and reduced the improved grid-fabrication techniques to practice. We also formulated a set of detailed instructions to be followed during the fabrication of electrodes. Other work included an examination of the molybdenum materials properties that should give the best results for hydroforming electrodes, particulary for the decel electrode of three-grid ion-extraction assemblies. This latter work is discussed in Section 5.

3.2.1 Improvements to the Hydroforming Fixture

Previous work[3-3] described the difficulty encountered in hydroforming the decel electrode of a three-grid ion-extraction assembly and concluded that flat spots or bumps appearing on the surface of the hydroformed electrodes could be eliminated by preventing air from being trapped between the grids during the dishing operation. To accomplish this, we modified the hydroforming fixture as shown in Figure 3-5. By eliminating the indicated air pocket, and by providing a vent for the release of any trapped air, electrode fabrication has been improved to the point that none of the ≃30 grids that have been hydroformed since the tooling was modified have shown any signs of non-sphericity.

3.2.2 Improvements to the Stress-Annealing Fixture

Following the earlier work,[3-3] we modified the stress-annealing fixture used for standard-dish-depth, three-grid optics assemblies. The problem that had been encountered in the past was thought to be the result of differential thermal expansion between the molybdenum electrodes and the carpenter-steel liner used in the annealing fixture. Under the present program, we replaced the steel liner with the graphite plug and liner shown in Figure 3-6. Stress-relieving operations performed since the fixture was modified have been highly successful. The only difficulty we have encountered has been an occasional cracking of the graphite ring. We believe the cracked rings have been caused by the rapid cooldown of the hot fixture, which is accomplished by blowing cold gas over the fixture. Closer control on vendor procedures is expected to eliminate this problem.

3.3 EXPERIMENTAL RESULTS

Table 3-1 lists the geometrical parameters of three ion-extraction assemblies that were fabricated and tested under this program to evaluate ion-optics performance effects related to aperture diameter and offset (to vector individual beamlets).

14629-1R1

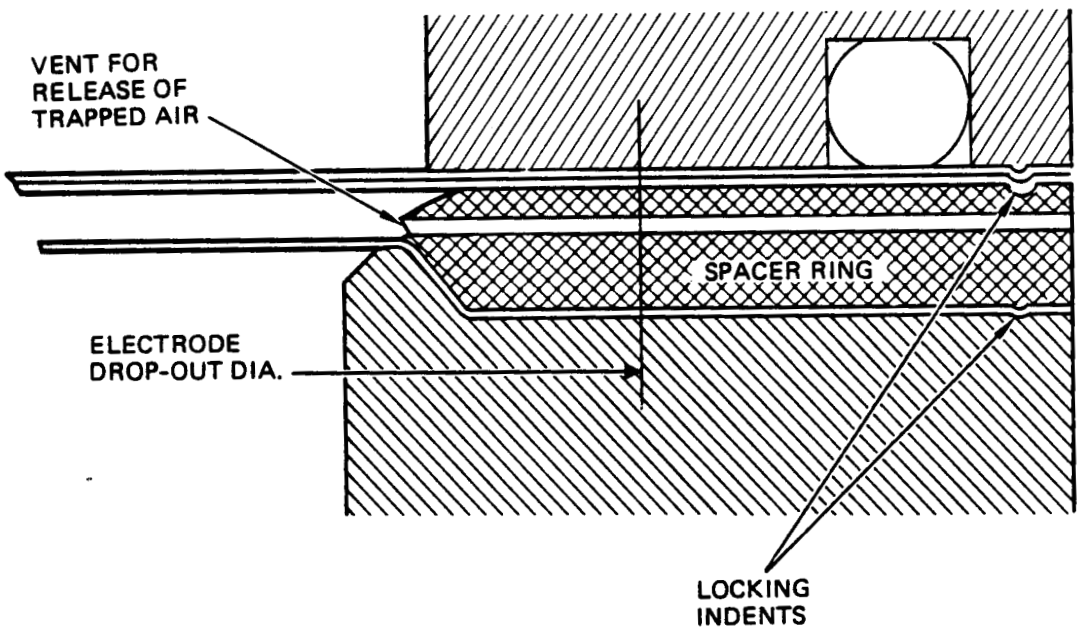

FIGURE 3-5. Modification to the clamping region of the hydroforming fixture for venting trapped air and preventing slippage of the grid material.

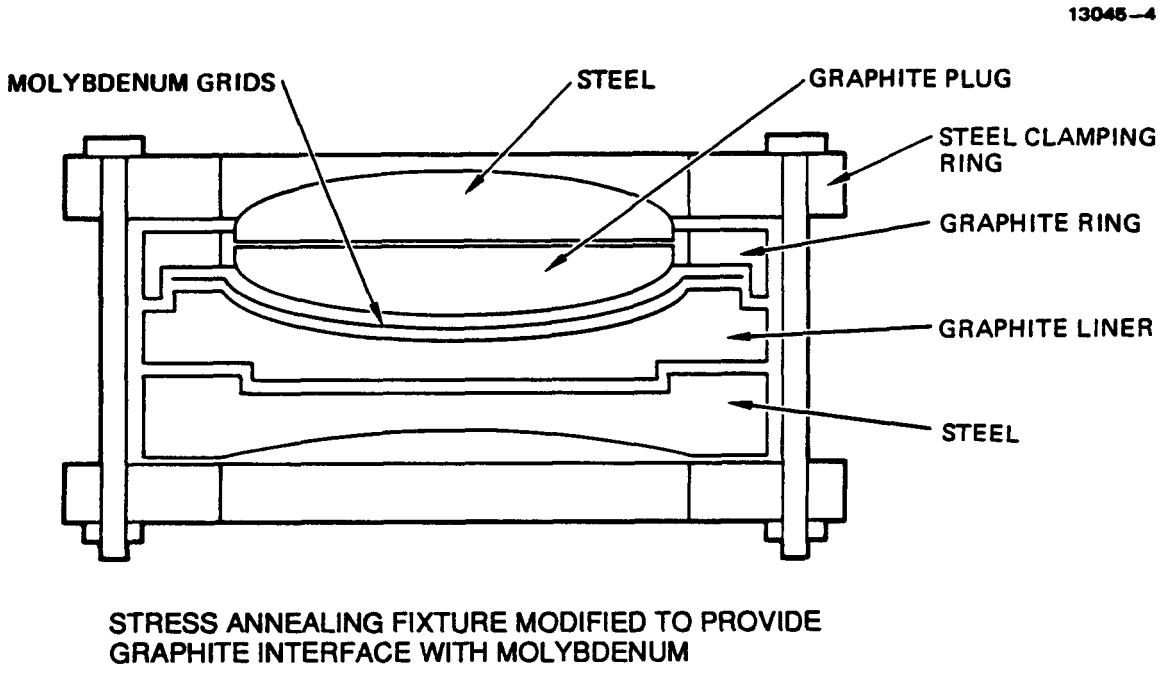

FIGURE 3-6. Improved stress-annealing fixture with graphite liners.

TABLE 3-1. Comparison of Ion-Extraction System Parameters.

14860-45R1

PARAMETER	GRID SET C015	GRID SET C025	GRID SET C027
APERTURE SHAPE	ROUND	HEX	ROUND
NUMBER OF APERTURES	14,996*	23,191*	14,995*
t_s, t_a, t_d	0.254	0.254	0.381
d_s	1.905	1.524	1.905
d_a	1.143	0.9144	1.143
d_d	1.524	1.219	1.524
$C\lambda^s$	-0.183	-0.183	-0.368
$C\lambda^a$	0.000	0.000	0.000
$C\lambda^d$	0.183	0.183	0.020
MINIMUM TOTAL VOLTAGE AT J_b = 2A	1250	1250	1200

* APPROXIMATE VALUE. DIMENSIONS ARE IN mm

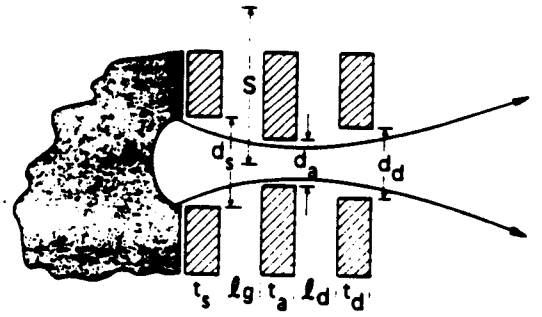

d_a – ACCEL HOLE DIAMETER

d_s – SCREEN HOLE DIAMETER

t_a – ACCEL GRID THICKNESS

t_s – SCREEN GRID THICKNESS

ℓ_g – SCREEN-TO-ACCEL INTERELECTRODE SPACING (0.584 mm NOMINAL)

ϕ_a – ACCEL GRID OPEN AREA FRACTION $\dfrac{\sqrt{3}\pi d_a^2}{6S^2}$

ϕ_s – SCREEN GRID OPEN AREA FRACTION $\dfrac{\sqrt{3}\pi d_s^2}{6S^2}$

S – APERTURE SPACING

C_λ – APERTURE COMPENSATION, % (W.R.T. ACCEL ELECTRODE)

ℓ_d – ACCEL-TO-DECEL INTERELECTRODE SPACING (0.584 mm NOMINAL)

t_d – DECEL GRID THICKNESS

3.3.1 Aperture Diameter

Previous studies have shown that screen apertures smaller than about 2 mm in diameter result in a reduction in perveance per aperture.[3-4] In spite of the reduction in perveance per aperture, we anticipated a net increase in beam-extraction capacity to result from reducing the screen-aperture diameter to less than 2 mm and increasing the number of apertures. Grid sets C015 and C025 were used to evaluate the effect of reducing the screen apertures from 1.91 mm to 1.52 mm, while increasing the number of apertures from about 15,000 to over 23,000. As the results of Table 3-1 indicate, there was essentially no increase in beam-extraction capacity; apparently the decrease in current per aperture was approximately equal to the increase in number of apertures (assuming the same gap and alignment). Recent analysis[3-5] and experimental results[3-6] indicate that aperture alignment becomes increasingly important as size is reduced.

We used optics set C015 to perform measurements of the perveance limit by spot welding a strip of 0.01-mm tantalum foil over a row of accel apertures on the downstream surface of the accel electrode (the decel electrode was removed) and then ion-machining through the foil by operating the thruster for a few hours. Foil-aperture diameters measured for different total accelerating voltages are shown in Figure 3-7. At a total voltage of 1900 V (well in excess of that corresponding to the perveance limit of $V_T \simeq 1100$ V), the machined apertures are relatively uniform across the beam diameter and are about 60% of the accelerator-aperture diameter. At total voltages near the perveance limit, the machined aperture diameters are about 90% of the accelerator-aperture diameter. The results of Figure 3-9 suggest that the perveance limit occurs near the center of the ion optics for this (uncompensated) grid set.

The effect of smaller aperture diameter on electron backstreaming limit is shown in Figure 3-8. The increase in net-to-total accelerating voltage ratio, R_{max}, with smaller apertures

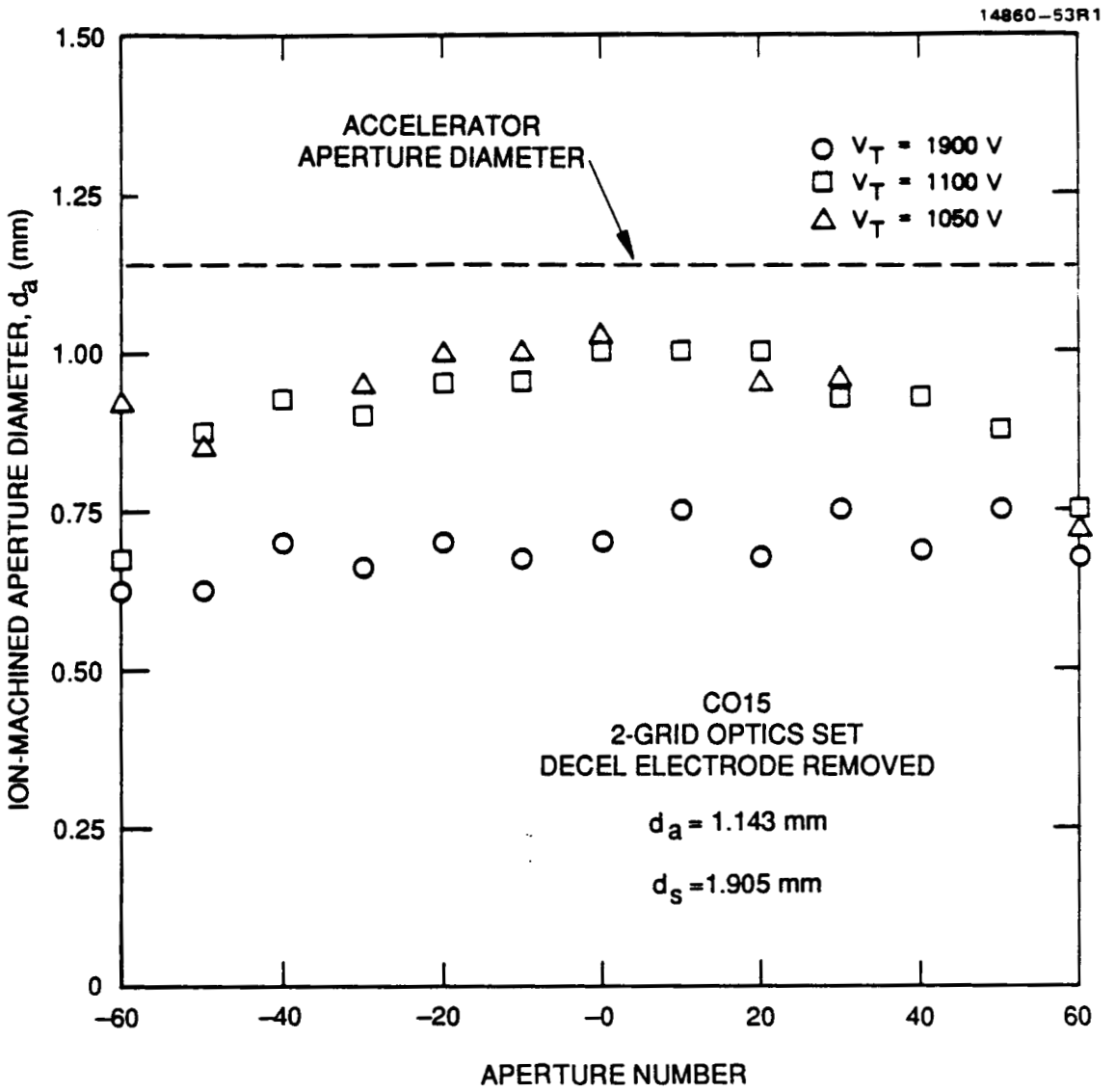

FIGURE 3-7. Variation of ion-machined aperture diameter for various radial locations and total accelerating voltages.

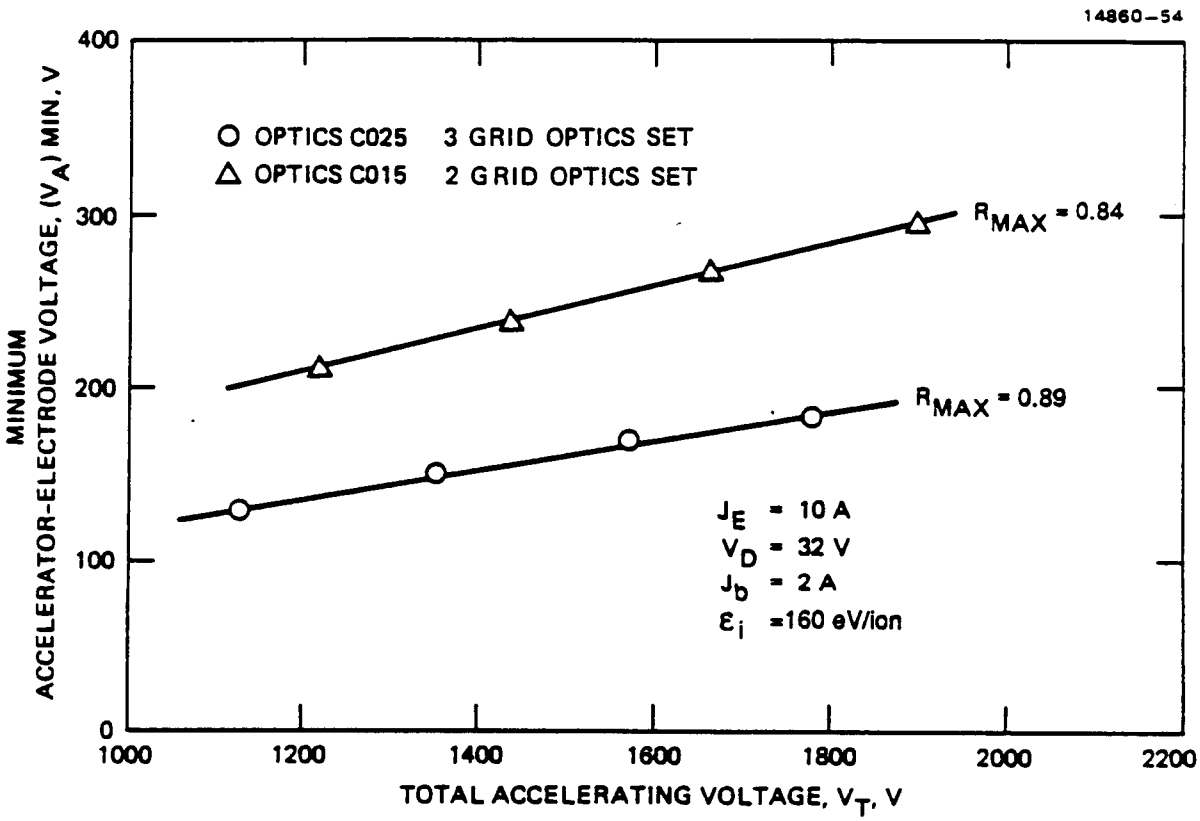

FIGURE 3-8. Variation of minimum total accelerator voltage with total accelerating voltage for grid sets C015 and C025.

is consistent with Kaufman's analysis[3-7] which relates R_{max} to the thickness-to-diameter ratio of the accelerator apertures, t_a/d_a. The ability to operate at such low accelerator voltages could significantly reduce the amount of accelerator-electrode sputtering due to a reduction in sputter yield that would accompany the reduced ion energies.

3.3.2 Beamlet Vectoring

The optics set C027 (Table 3-1) was designed for a net-to-total accelerating voltage ratio of R = 0.5, using a beamlet-vectoring model[3-2] to calculate the aperture compensation required to vector beamlets parallel to the thruster axis. We verified the effectiveness of the aperture compensation in achieving beamlet vectoring by measuring the thrust-loss factor, F_t, as a function of the net-to-total accelerating voltage ratio, R. Figure 3-9 shows the variation of measured thrust-loss factor for optics sets C027 (compensated) and C015 (uncompensated). The thrust-loss factor for optics set C027 varies with R and has a maximum near its design operating point of R = 0.5. By comparison, the thrust-loss factor is essentially independent of R for the uncompensated optics set C015.

Further insight into the results presented in Figure 3-9 can be obtained from the angular dispersion profiles of the ion beamlets obtained from ExB probe measurements. Figure 3-10 shows the results for optics set C015, showing that the beamlet angle is independent of R. Furthermore, the profiles decrease in height and increase in angular width as the R value is reduced. This behavior is a consequence of beamlet spreading that accompanies the increase in ion deceleration at low values of R.

Angular dispersion profiles for optics set C027 are presented in Figure 3-11. These profiles also decrease in height and increase in angular width as the R value is reduced. However, the beamlet angle is strongly dependent on the R value for this compensated optics set. In addition, at an R value

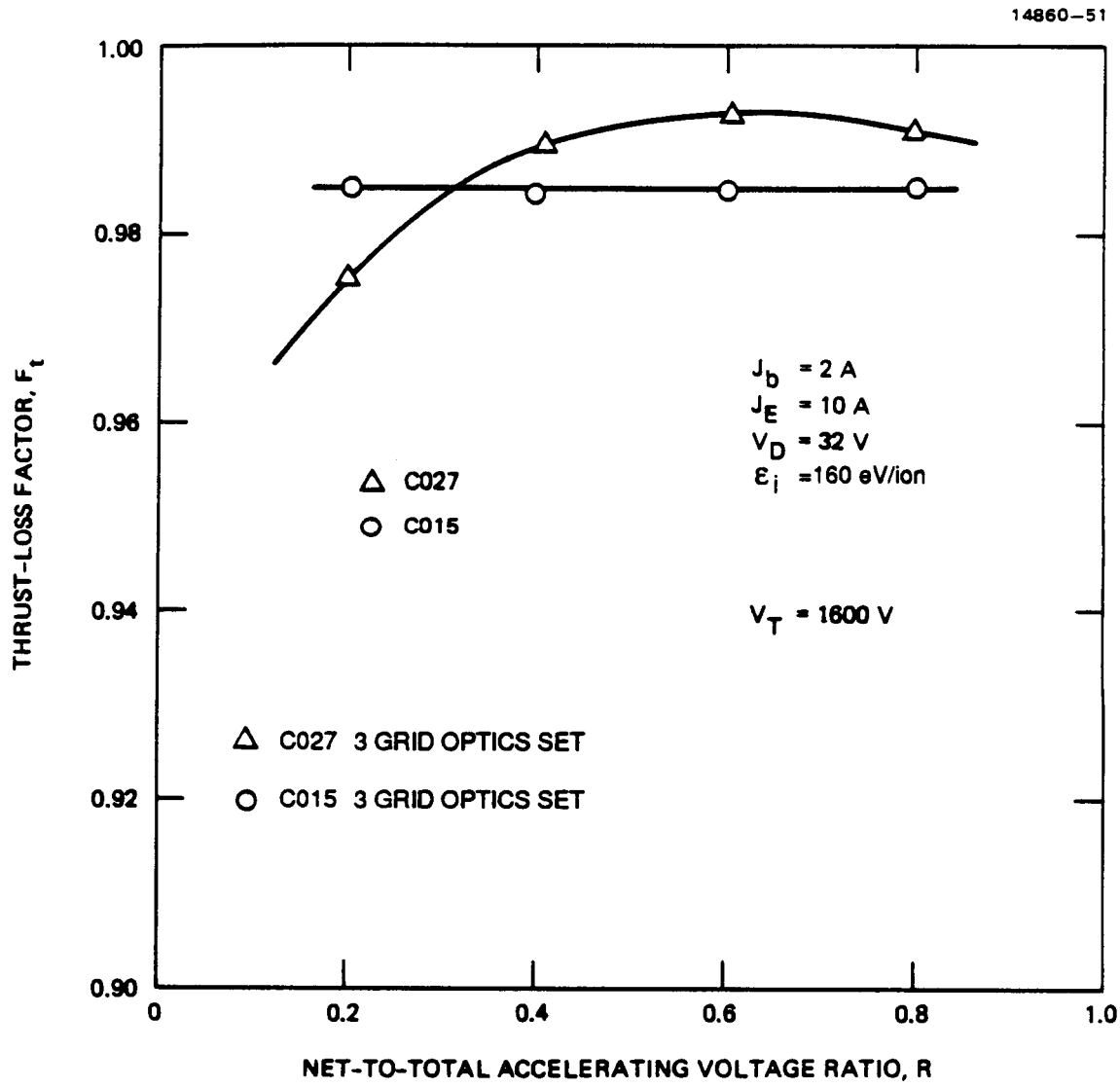

FIGURE 3-9. Variation of thrust-loss factor with net-to-total accelerating voltage ratio for grid sets C015 and C027.

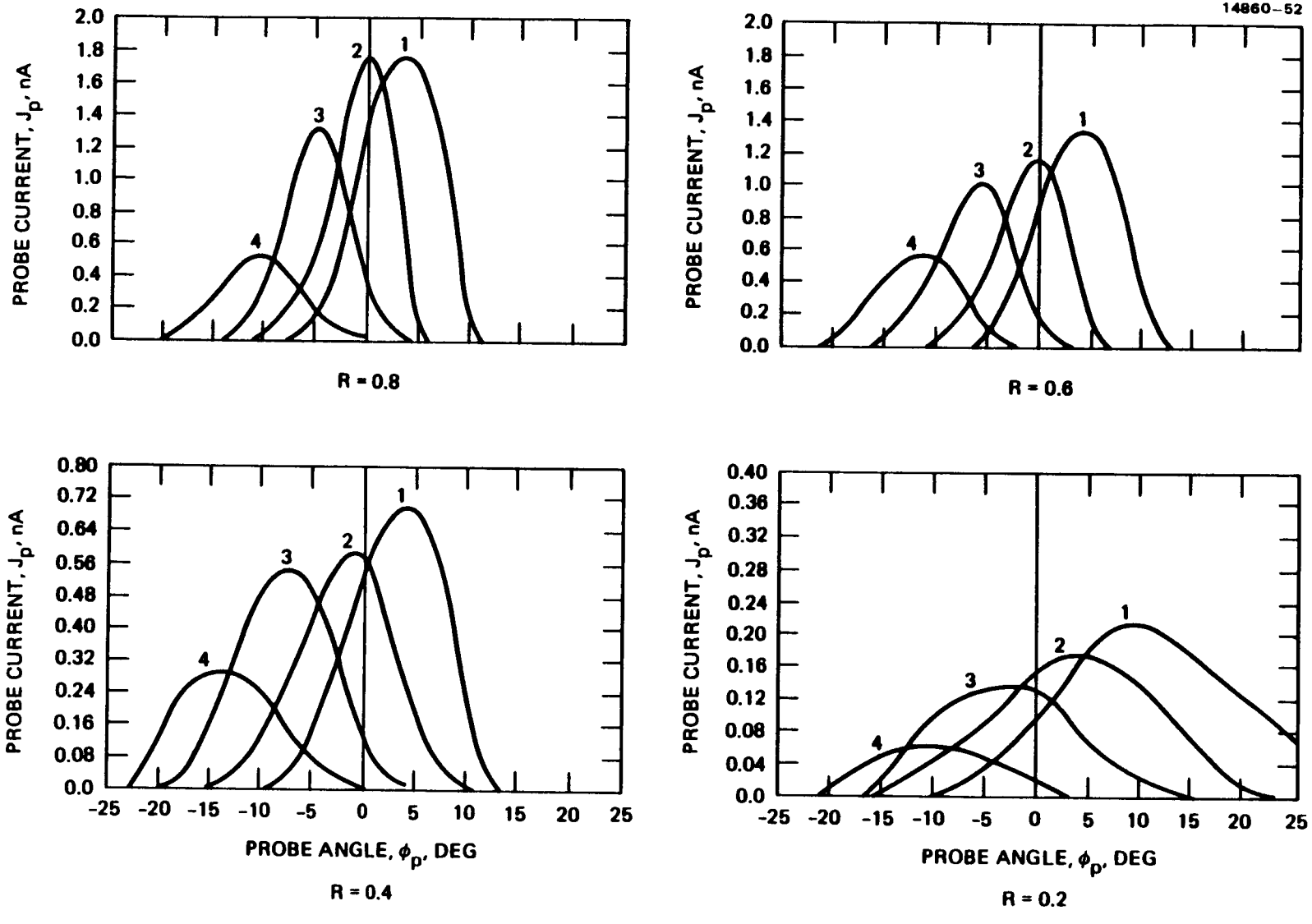

FIGURE 3-10. Ion current angular dispersion profiles for grid set C015. 1 = thruster centerline, 2 = 1/4 thruster radius, 3 = 1/2 thruster radius, 4 = 3/4 thruster radius.

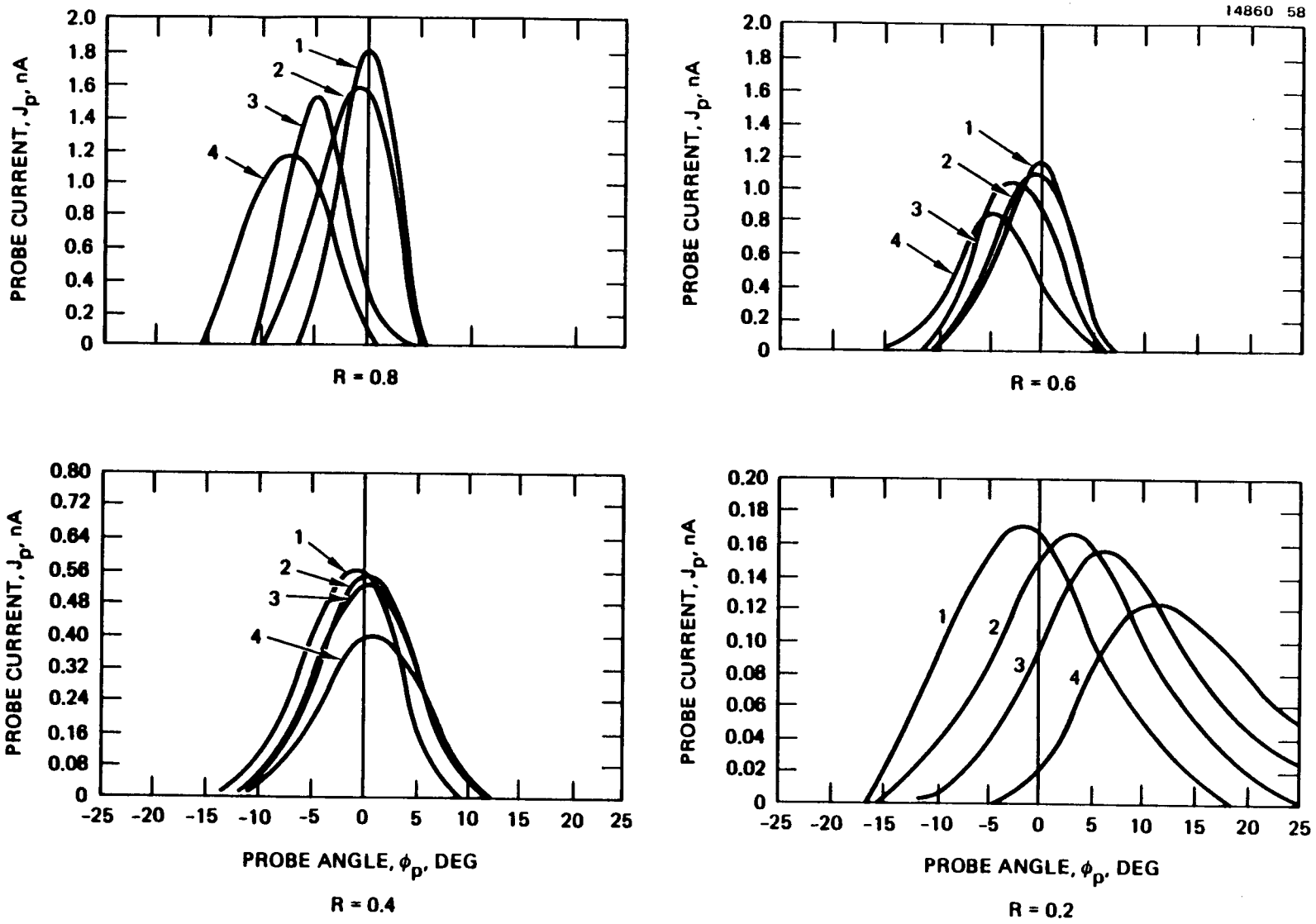

FIGURE 3-11. Ion current angular dispersion profiles for grid set C027. 1 = thruster centerline, 2 = 1/4 thruster radius, 3 = 1/2 thruster radius, 4 = 3/4 thruster radius.

between 0.4 and 0.6 there is nearly complete beamlet vectoring along the lines parallel to the beam axis for all radial locations (consistent with a large value of F_t shown in Figure 3-9), while for other values of R there is off-axis beamlet vectoring (consistent with the lower values of F_t shown in Figure 3-9). Figure 3-11 indicates the cross-over beamlet vectoring occurs at an R value of 0.2.

REFERENCES

3-1. Poeschel, R.L. and Beattie, J.R., "Primary Electric Propulsion Technology Study," NASA CR-159688, Hughes Research Laboratories, Malibu, California, November 1979.

3-2. Beattie, J.R., "Extended Performance Technology Study - 30-cm Thruster," NASA CR-168259, Hughes Research Laboratories, Malibu, California, June 1983.

3-3. Poeschel, R.L., "Development of Advanced Inert-Gas Ion Thrusters," NASA CR-168206, Hughes Research Laboratories, Malibu, California, July 1983.

3-4. Rawlin, V.K., "Studies of Dished Accelerator Grids for 30-cm Ion Thrusters", AIAA Paper No. 73-1086, 1973.

3-5. Kaufman, H.R. and Robinson, R.S., "Minimum Hole Size in Ion Optics", J. Spacecraft, Vol. 22, No. 3, pp. 381-382, May-June 1985,

3-6. Rovang, D., "Ion Extraction Capabilities of Two-Grid Accelerator Systems", NASA CR-174621, Colorado State University, Fort Collins, Colorado, February 1984.

3-7. Kaufman, H.R., "Technology of Electron-Bombardment Ion Thrusters", in Advances in Electronics and Electron Physics, Vol. 36, L. Marton, ed., Academic Press, pp. 265-373, 1974.

SECTION 4
POWER-PROCESSOR SIMPLIFICATIONS

A dramatic simplification (factor-of-ten reduction in parts count) of the power processor required to operate an 8-cm-diameter mercury ion thruster was demonstrated under a joint NASA/Hughes program aimed at reducing the complexity of ion-propulsion systems.[4-1] The Simplified Power Processor Unit (SPPU) shown in the schematic of Figure 4-1 was built under the Hughes-funded program, and preliminary evaluation of the unit (using a laboratory-model 8-cm-diameter thruster) demonstrated the feasibility of the simplified approach. Under the present program, we investigated the startup transients and steady-state operating characteristics of a laboratory-model 8-cm-diameter thruster when operated with the SPPU. We also demonstrated that the SPPU could be used to successsfully operate an 8-cm-diameter thruster that was functionally equivalent to the Ion Auxiliary Propulsion System (IAPS) flight thrusters and verified that steady-state performance was comparable to that obtained using a conventional laboratory-model power processor and test console.

4.1 STEADY-STATE AND TRANSIENT OPERATION

The initial operation[4-1] of the SPPU used the output of Resistance Temperature Devices (RTD's) to control the output of the discharge- and neutralizer-vaporizer-heater supplies (see Figure 4-1). Under the present program, we improved the performance characteristics of the SPPU by adding an external circuit that transforms thermocouple input into simulated-RTD output. By replacing the RTD's on the laboratory-model 8-cm-diameter thruster with thermocouples, we could sense the temperature at a location closer to the vaporizer and we eliminated a 20°C to 50°C overshoot in temperature that had been

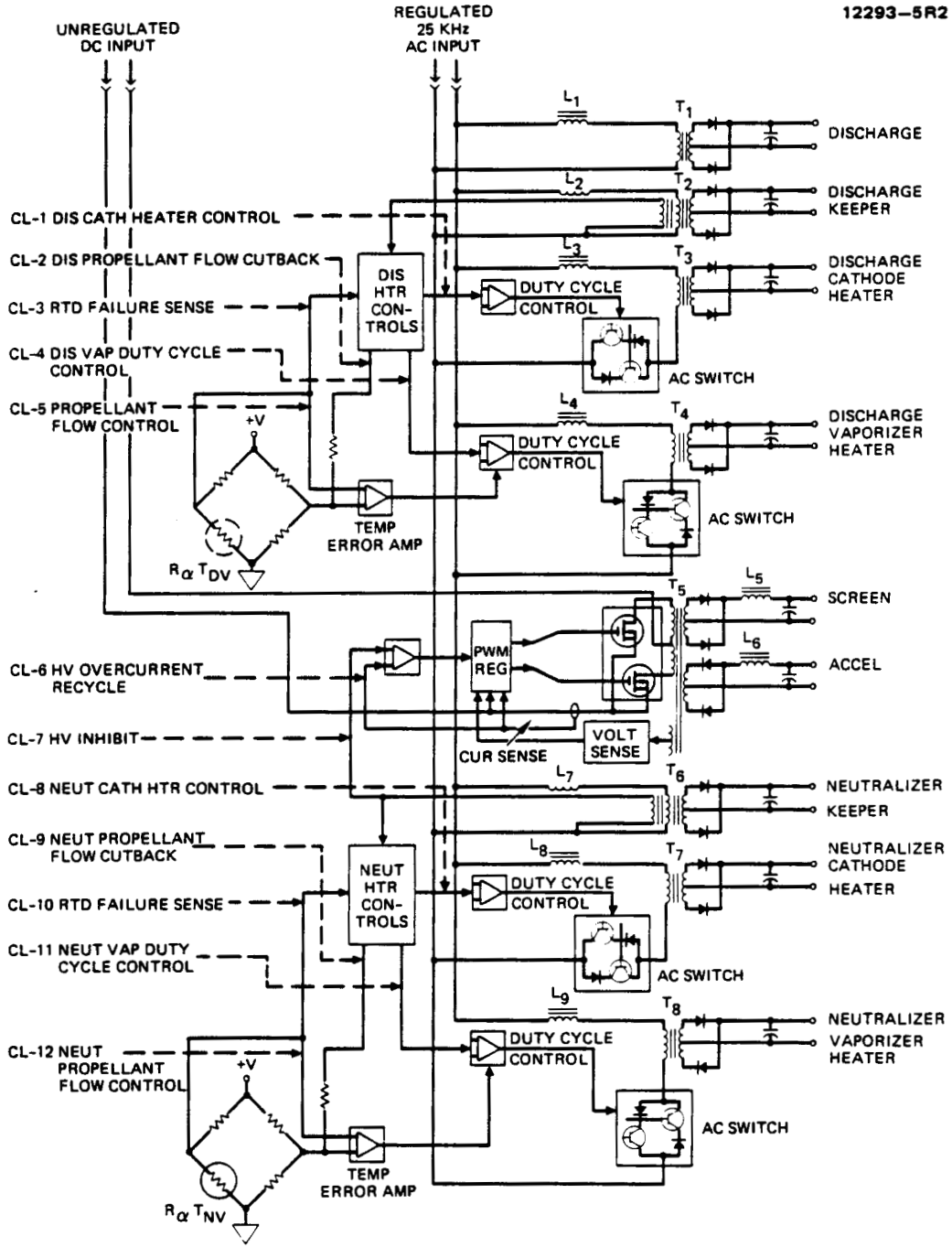

FIGURE 4-1. Schematic diagram of SPPU with RTD's to control the output of the discharge- and neutralizer-vaporizer-heater supplies.

observed when the thruster was equipped with RTD's. We emphasize that the modification was only to accommodate the particular thruster setup; either RTD or thermocouple input to the SPPU is satisfactory, as long as the temperature-sensing elements are placed in close proximity to the vaporizers.

4.1.1 Vaporizer-Temperature Optimization

We operated the laboratory-model eXtended-performance Ion Auxiliary Propulsion System (XIAPS) thruster under steady-state conditions for several hours to ensure that thermal equilibrium had been reached. By varying the discharge-vaporizer temperature and recording the discharge voltage and beam current corresponding to each temperature, we obtained the characteristics shown in Figure 4-2. The results were obtained by increasing the temperature in the manner suggested by the arrows shown on the curves (we understand the hysteresis effect to be the result of thermal lag in the vaporizer thermocouple). Another representation of these results is presented as Figure 4-3. Both figures show that a local maximum in beam current exists at a flow rate corresponding to a discharge-vaporizer temperature of T_{d_v} = 355°C; variations in flow about the optimum produces a dramatic reduction in the beam current. The characteristic presented in Figure 4-3 shows that the discharge voltage could be used as a controlled parameter (instead of the discharge-vaporizer temperature) to achieve maximum beam current.

4.1.2 Cold-Start Behavior

Figure 4-4 shows the vaporizer-temperature variation of the XIAPS thruster for a period of approximately two hours after an ON command was issued to the SPPU. The temperatures are seen to reach their reference values in a matter of a few minutes and are then controlled to within 0.5% of these values. Figure 4-5 presents the temporal variation of beam current and discharge voltage, showing that these parameters reach 90% of their steady-state values within 30 minutes of startup. The scatter in the

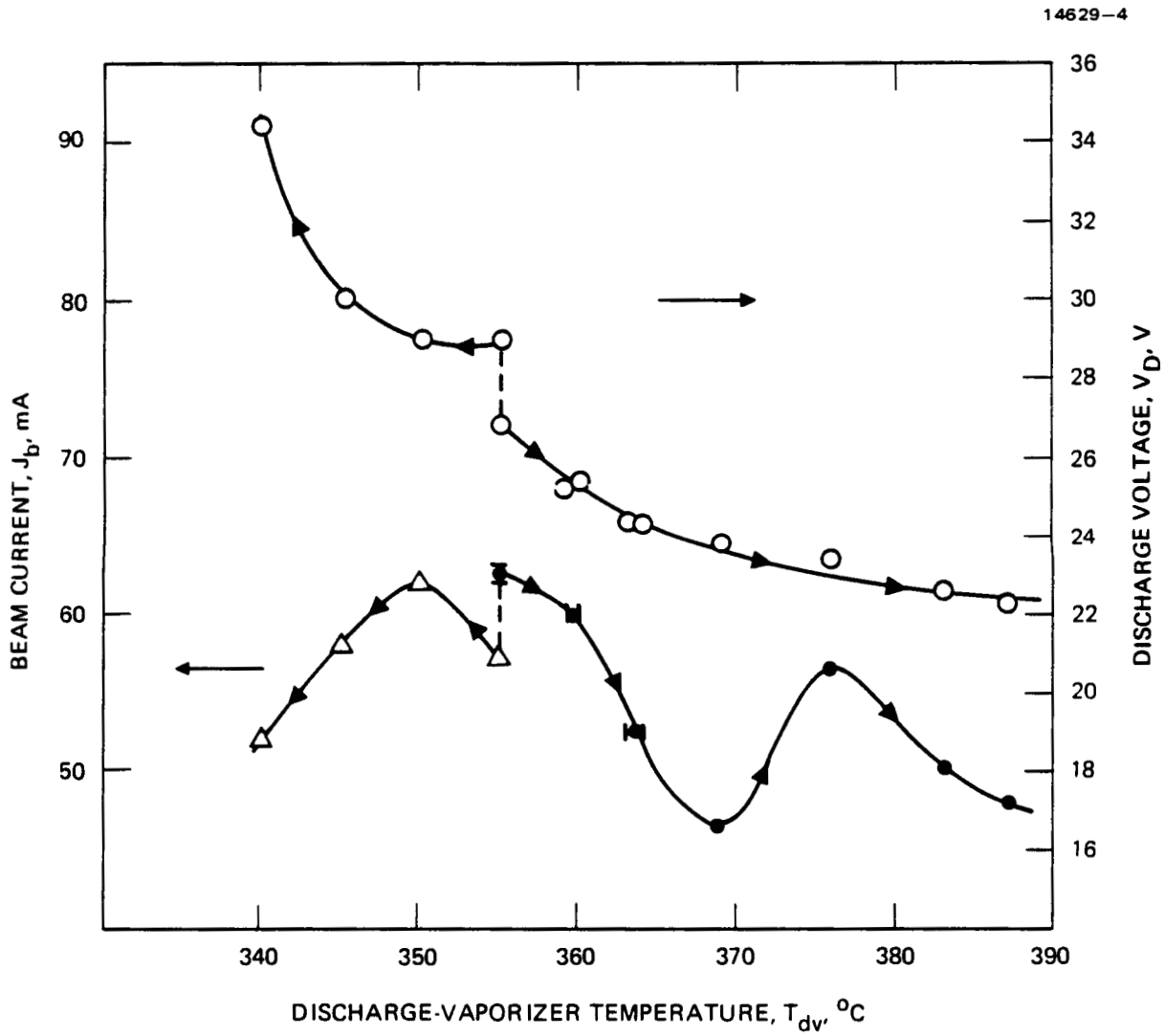

FIGURE 4-2. Variation of beam current and discharge voltage with discharge-vaporizer temperature for the XIAPS thruster.

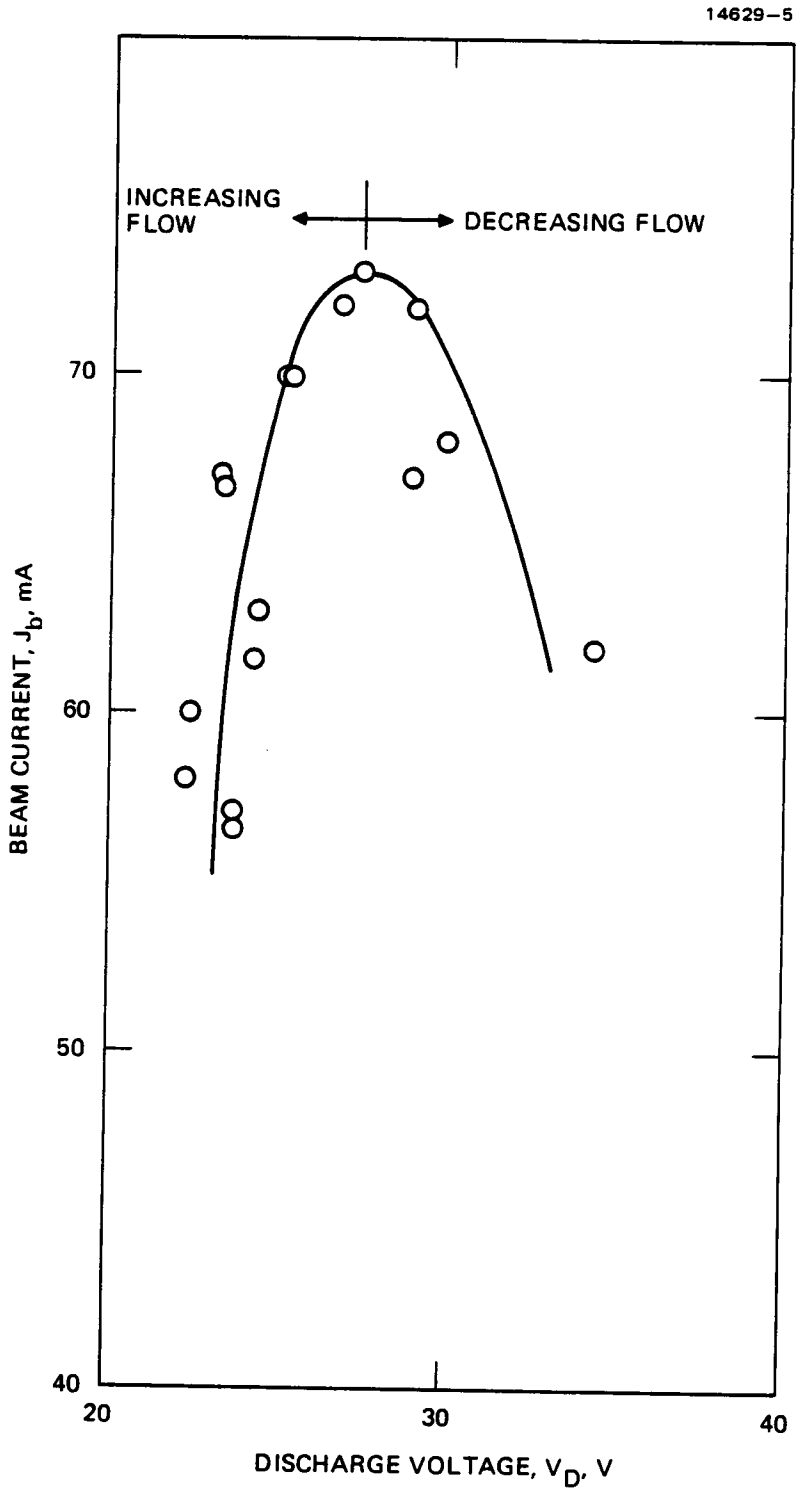

FIGURE 4-3. Beam-current/discharge-voltage characteristic obtained by varying discharge flow rate.

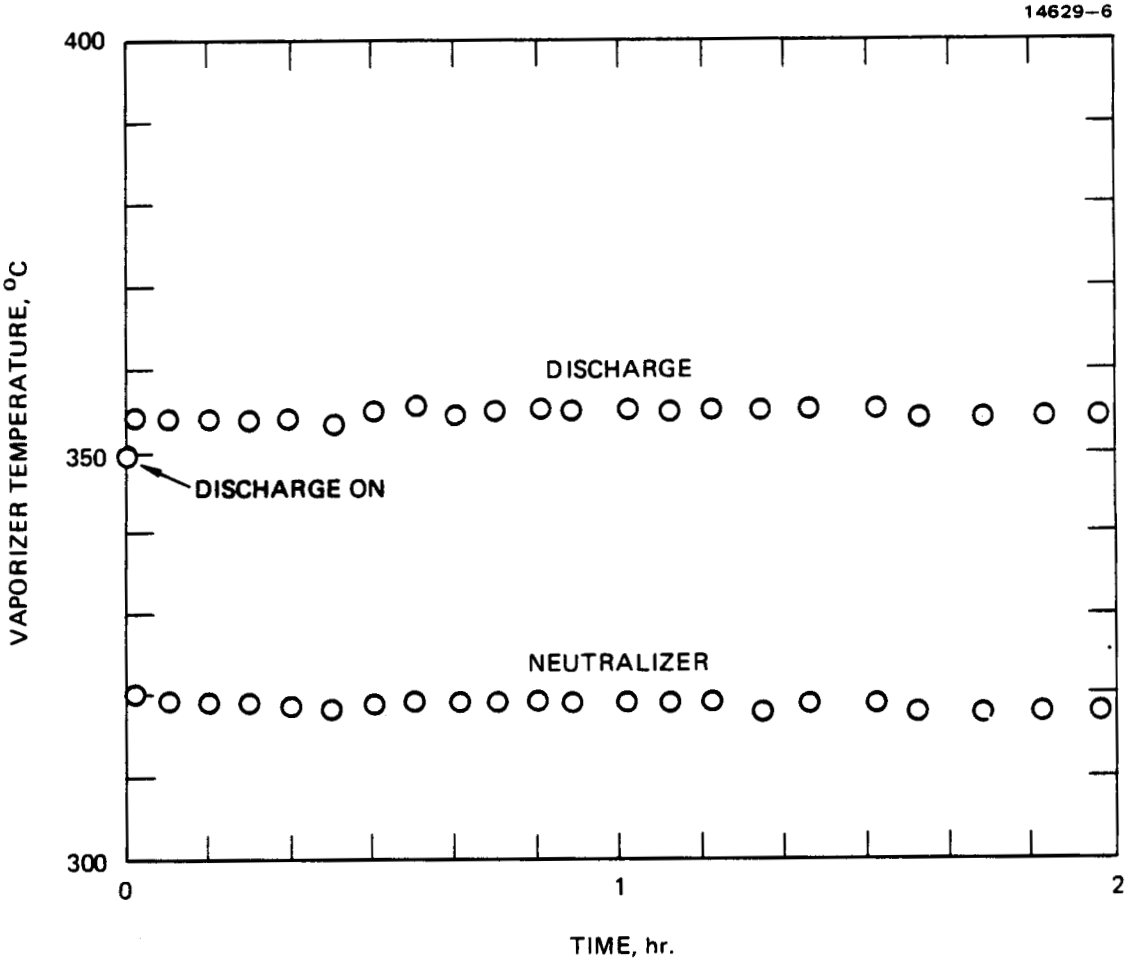

FIGURE 4-4. Temporal variation in vaporizer temperature of the XIAPS thruster after issuing an ON command to the SPPU.

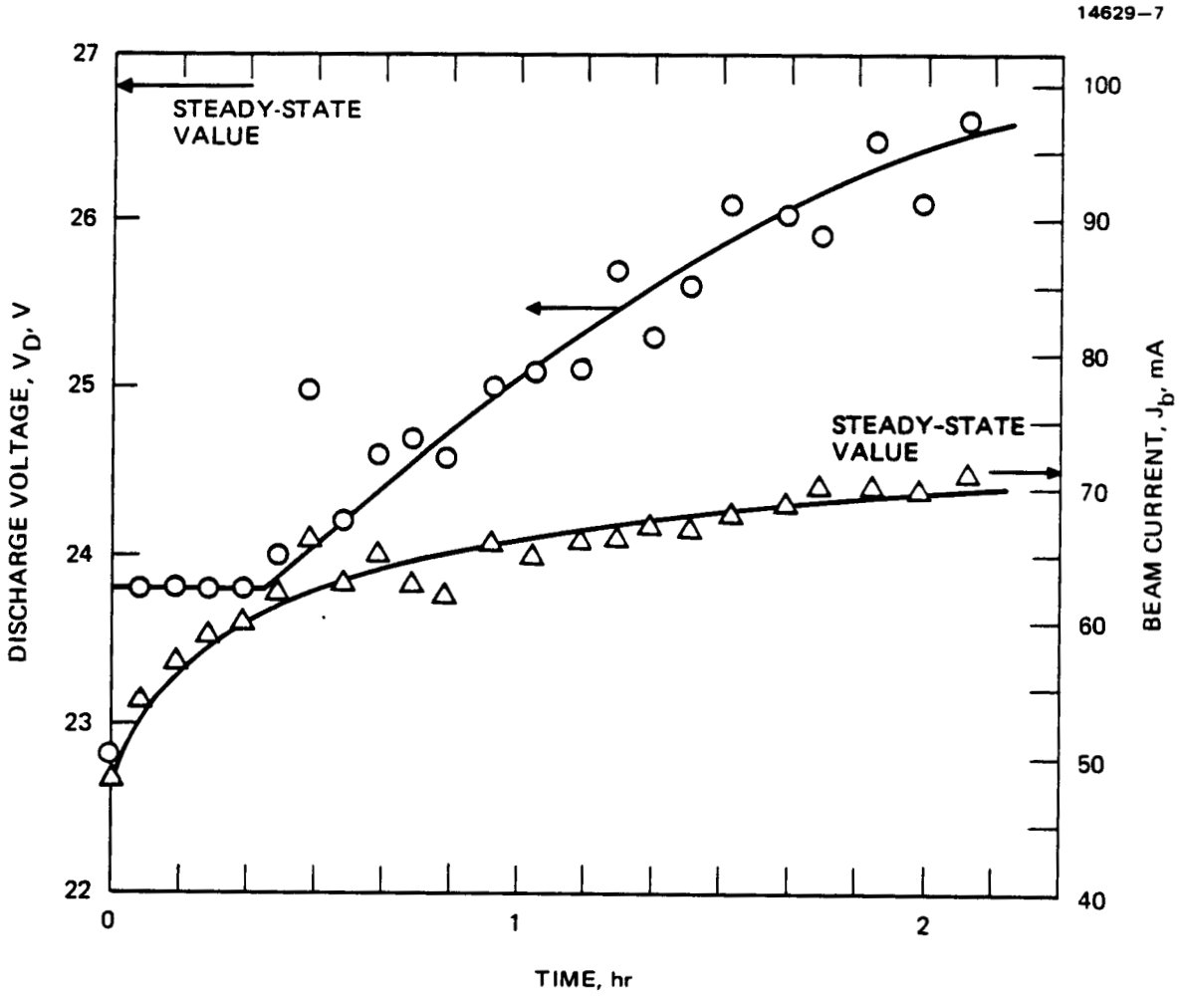

FIGURE 4-5. Temporal variation in beam current and discharge voltage of the XIAPS thruster after issuing an ON command to the SPPU.

data is attributed to frequent screen and accel overcurrent and subsequent recycling (which we believe could be reduced or possibly eliminated as a result of optimizing the recycle algorithm and circuity in the present SPPU).

In preliminary tests[4-1] in which RTD's were used to sense the vaporizer temperature, the reference was set to about 10°C lower than the value (355°C) that our steady-state test results indicate to be the optimum (maximizes beam current). This had the effect of enabling the beam current to reach its setpoint (J_b = 72 mA) shortly after startup, but eventually the beam current dropped to the steady-state value corresponding to the reduced temperature of T_{dv} = 345°C (about J_b = 40 mA). We interpret this behavior in the following manner: As the discharge chamber heats up, propellant is liberated from the walls, resulting in a "flooded" condition (the vaporizers are operated at constant temperature). The "effective" propellant flow is greater than that corresponding to the vaporizer temperature, and thruster operation moves to the high-flow side of the maximum indicated in Figures 4-2 and 4-3. As the chamber walls heat up and an equilibrium condition is approached, the effective propellant flow is reduced, and operation moves closer to the maximum in beam current (cf. Figures 4-2 and 4-3). With the previous (RTD) control philosophy, less propellant flow was introduced through the vaporizer, so that the effective flow during the thermal-transient period was lower, resulting in initial operation nearer the optimum-beam-current point. However, in this case the steady-state beam current was substantially below that corresponding to the maximum, since the reduced propellant flow places steady-state operation to the right of the maximum in Figures 4-2 and 4-3.

This argument is supported by the "cold-start" test results of Figure 4-4. With the beam current plotted versus discharge voltage as in Figure 4-6, we see that the initial operation places us on the high-flow side of the maximum-beam-current point, and that the temporal variation corresponds to a reduction

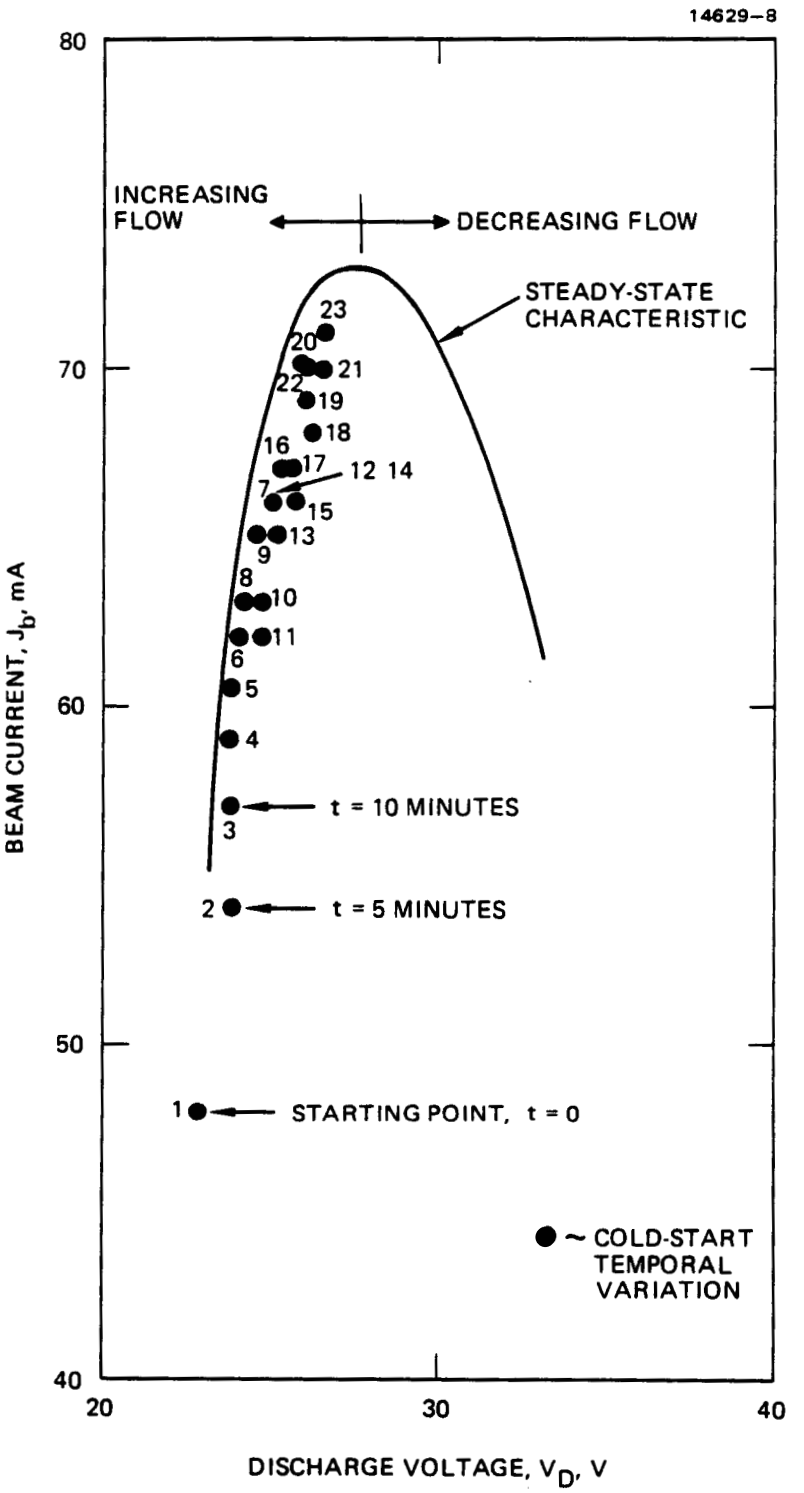

FIGURE 4-6. Comparison of "cold start" temporal behavior of XIAPS thruster with steady-state performance characteristic.

in "effective" propellant flow with a resultant shift toward the optimum operating conditions. This transient-flow effect could presumably be eliminated either by preheating the discharge chamber, or by controlling the vaporizer flow in proportion to an operating parameter such as beam current or discharge voltage (instead of discharge-vaporizer temperature).

Effects similar to the one described above have also been observed in a 30-cm-diameter thruster, when it was brought to full beam current within a few minutes of discharge ignition. In this case, the cathode flow was regulated to maintain constant discharge voltage, and we observed a reduction in vaporizer temperature of about 100°C (from 320°C to about 220°C), followed by a corresponding increase in vaporizer temperature as the thruster-body temperature increased.

4.2 IAPS-EQUIVALENT THRUSTER OPERATION

The 8-cm-diameter thruster S/N 901 was modified to be functionally equivalent to an IAPS flight thruster by incorporating the most-essential modifications that were employed under the IAPS flight program to upgrade the 900-series thrusters to flight specifications. The modifications included replacing the discharge and neutralizer cathodes, the cathode pole piece and baffle, and the ion-extraction assembly.

We conducted a Performance Acceptance Test (PAT) of the S/N 901 retrofit thruster, using the same laboratory-model power processor and test console that was used to test the IAPS flight thrusters. The same procedures used in acceptance testing the flight thrusters were followed for vaporizer calibration, cathode conditioning, and startup. We found that the retrofit thruster performs much like the flight thrusters; a comparison of the operating parameters for the S/N 901 thruster with those representative of the Cyclic Life Test thruster S/N 903 and the flight thrusters S/N 908 and S/N 909 is presented in Table 4-1.

TABLE 4-1. Comparison of the Performance Measurements for the Retrofit Thruster and several Flight-Type Thrusters

THRUSTER S/N	901	901	903	908	909
TEST CONSOLE	LAB	SPPU	LAB	LAB	LAB
DATE	1/84	2/84	12/80	12/80	11/80
PARAMETER/VALUE					
V_D, V	42.1	39.0	39.7	39.5	39.5
I_D, mA	369	428	386	439	428
V_{DK}, V	14.3	14.4	12.7	13.5	13.9
I_{DK}, mA	61	95	60	60	60
V_δ, V	27.0	24.6	27.0	26.0	25.6
V_{DH}, V	3.89	4.1	2.31	2.46	2.42
I_{DH}, A	1.85	1.95	1.16	1.16	1.16
V_{DV}, V	4.50	5.5	4.52	4.49	4.35
I_{DV}, A	1.58	1.92	1.64	1.66	1.62
V_{NK}, V	16.4	16.6	15.6	15.8	15.8
I_{NK}, mA	501	430	500	500	500
V_{NH}, V	2.78	2.63	2.85	2.98	2.92
I_{NH}, A	1.31	1.24	1.30	1.30	1.30
V_{NV}, V	2.20	3.6	2.30	2.41	2.64
I_{NV}, A	.66	1.08	.72	.77	.81
V_S, V	1176	1200	1200	1200	1200
V_B, V	1207	--	1228	1226	1223
I_S, mA	72.0	72.0	72.0	72.0	72.0
V_A, V	-284	-300	-300	-300	-300
I_A, mA	.342	.400	.231	.247	.245
V_C, V	-11.0	--	-11.9	-13.8	-16.0
T_{DV}, °C	290	278	266	294	263
m_{DV}, mA	86.7	--	86.4	95.5	93.9
T_{NV}, °C	284	289	280	280	290
m_{NV}, mA	5.44	--	4.93	6.0	5.8
m_T, mA	92.1	--	91.4	101.5	99.7
η_{Hg}, %	78	--	79	71	72
η_{Dish}, %	83	--	83	75	77
ϵ_i, eV/ion	228	--	223	252	246
P_{TOTAL}, W	131.7	--	128.7	131.4	130.8

The only notable differences in these results are a higher cathode-heater power, (which was necessary in order to sustain the discharge), and for a nominal V_δ the discharge voltage and discharge-keeper voltage are a few volts higher than those typical of the flight thrusters. Performance-documentation results are presented in Figures 4-7 and 4-8, which show measured propellant-utilization efficiency and ion-production cost versus V_δ. These results show that the optimum V_δ lies in the range $26\ V \leq V_\delta \leq 28\ V$.

Having characterized the operation of the retrofit thruster using a conventional power processor, we next operated it using the SPPU, which uses constant-vaporizer-temperature control loops for controlling the mercury flow through the discharge and neutralizer vaporizers. During the startup, predetermined maximum currents are applied to both the discharge and neutralizer cathode heaters and vaporizers. The keeper and discharge voltages are also ON at this time. When the pre-selected vaporizer temperatures are reached, the vaporizer loops operate in proportional control to maintain these temperatures. The thruster remains in this condition until the keepers ignite.

After the neutralizer keeper ignites, the current to the neutralizer-cathode heater drops to a lower setpoint (there are only two setpoints on each cathode-heater supply) while the neutralizer-keeper current remains constant. In a similar manner, the ignition of the discharge keeper is followed by a lowering of the cathode-heater current to the predetermined value, while the discharge-keeper current remains constant. The main discharge can ignite any time after the discharge keeper. The screen and accel voltages are applied only after the discharge and neutralizer keepers have ignited, the discharge has ignited, and the discharge voltage has dropped to less than $V_D = 50\ V$. There is a recycling feature of the SPPU that is triggered by sensing excessive screen or accel currents.[4-1]

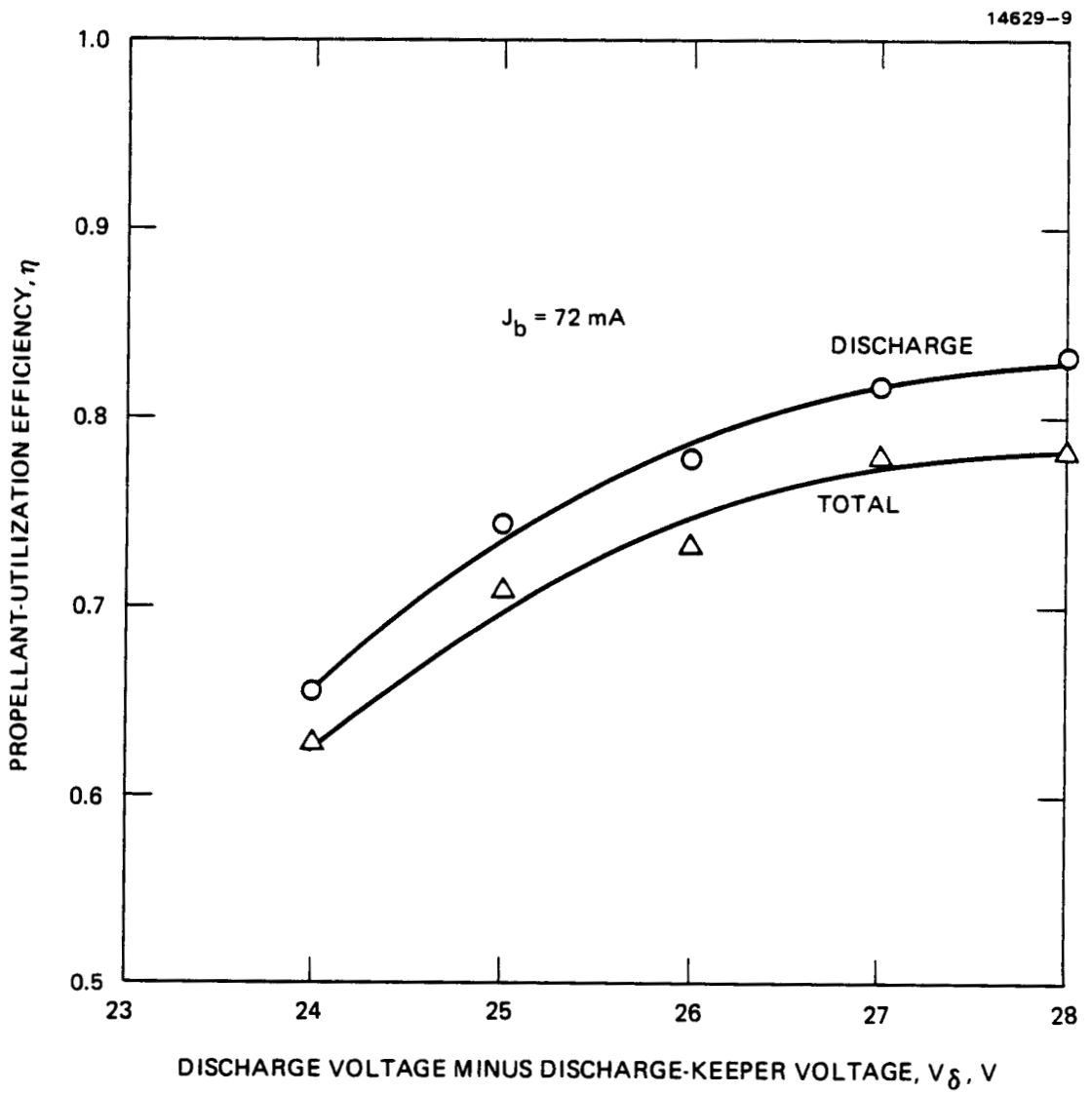

FIGURE 4-7. Performance of thruster S/N 901 operated with the SPPU.

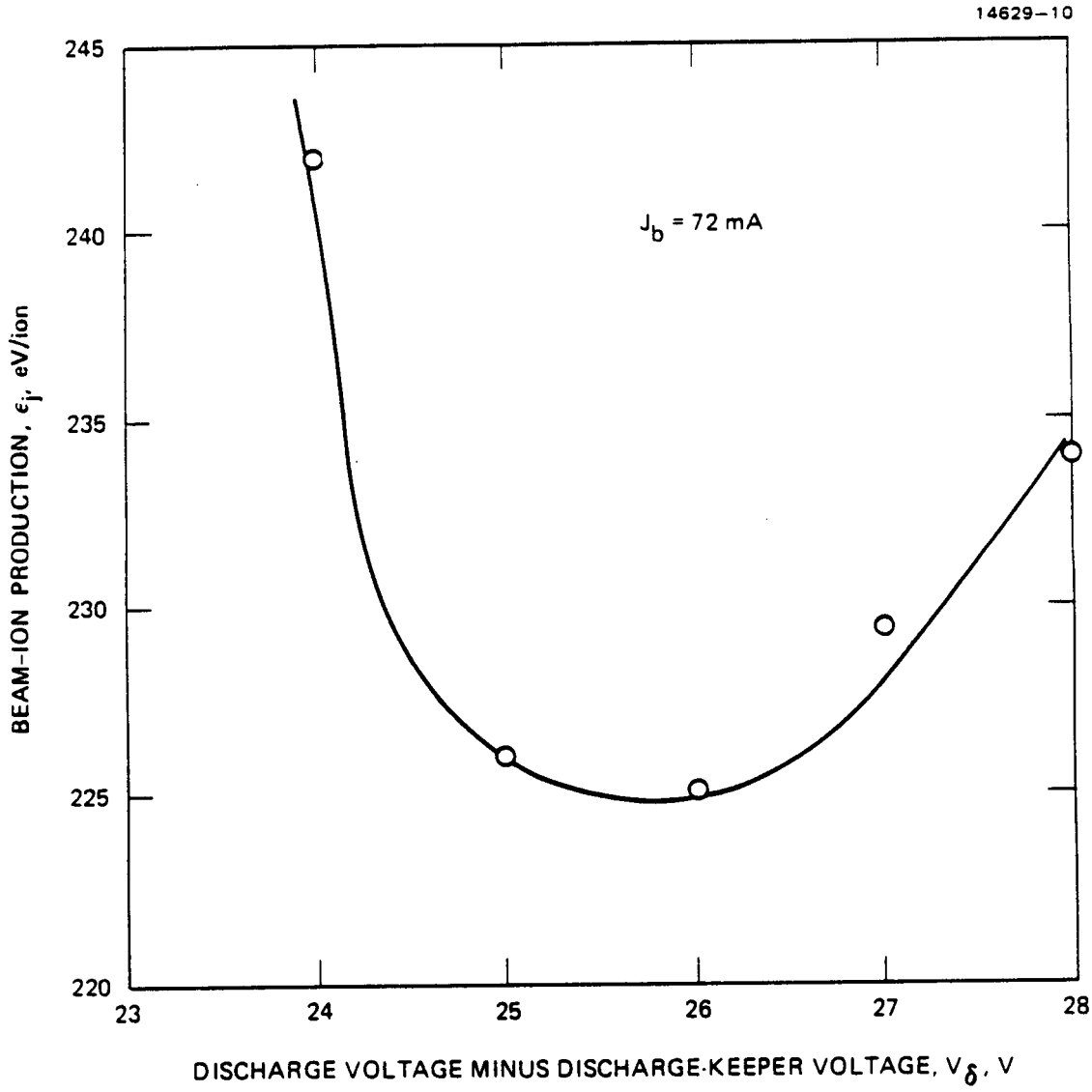

FIGURE 4-8. Variation of beam-ion-production cost with V_δ for thruster S/N 901.

Several demonstrations verified that a beam current of J_b = 72 mA could be obtained with the pre-selected values of discharge current and discharge-vaporizer temperature. Typical electrical measurements are presented in Table 4-1 for comparison with the results obtained while operating the retrofit thruster S/N 901 on a conventional power processor. Flow rates were not measured for the data corresponding to operation on the SPPU, but the vaporizer temperatures were about the same as those recorded for thruster S/N 901 when operated using the laboratory test console.

During the tests conducted with the S/N 901 retrofit thruster, we observed that the SPPU has a tendency to undergo excessive power-supply recycling during thruster startup from ambient temperature or below. Similar results were observed in earlier tests that were conducted using the XIAPS thruster. In these tests, we determined that cold startups are characterized by excessive "effective" propellant flow (the sum of the discharge-vaporizer flow plus the propellant liberated from the walls), or "flooding" of the discharge chamber. In the more recent tests, we could successfully prevent the recycling by either preheating the thruster or by delaying the application of screen and accel voltages. The recycle feature in the SPPU appears to be more sensitive than that used in the IAPS power electronics, and it may have to be modified to enable rapid cold-starting without experiencing excessive high-voltage breakdowns between the ion-extraction electrodes.

With the exception noted above, the operation of an "IAPS-equivalent" thruster on the SPPU was quite satisfactory, and it appears that only minor modifications to the SPPU design are desirable. The only area of major concern is the constant-vaporizer-temperature control philosophy, which is based on the assumption that the calibration curves of the vaporizers remain constant throughout the lifetime of the thruster. This may or

may not be true, and if it is not, a different control philosophy will have to be adopted. With only a slight increase in complexity, the SPPU circuitry can be modified to permit active control of the vaporizer power to maintain the desired values of discharge voltage and neutralizer-keeper voltage. Application of the SPPU technology to inert-gas thrusters (in which the vaporizers are replaced by flow impedances) appears to be straightforward.

REFERENCES

4-1. Wessel, F.J. and Hancock, D.J., "Simplified Power Processing for Ion Thruster Subsystems," AIAA Paper No. 83-1394, Seattle, Washington, June 1983.

SECTION 5

TECHNOLOGY READINESS OF THE J-SERIES THRUSTER

Although several mercury-ion-thruster subsystems have been brought to flight status (SERT I, SERT II, IAPS, and RIT 10), there is a pervasive perception by mission designers that mercury-ion-propulsion technology does not have the demonstrated maturity required for a primary system (i.e., mission fails unless system performs to specification). Some of the major system concerns that have been voiced are as follows:

- Reliability documentation is inadequate
  - only limited data are available
  - test results are flawed
  - documentation of test results is insufficient
  - tests performed only on components
  - qualification requirements only vaguely specified
- Interface specifications are not well defined
  - exhaust-plume definition and contamination
  - thrust-vector location
  - control requirements
  - high-voltage effects on spacecraft
  - system-integration procedures undefined or undocumented
- Technology concepts under development are too complex and/or too expensive
  - too many parts
  - too many controls
- Required operating time is too long
  - high reliability mandated
  - long operating or storage life mandated
  - qualification of representative flight system is prohibitively expensive and time consuming

If the concerns of the system engineer that are listed above are to be alleviated by technology development, the following tasks must be addressed:

- A set of design specifications must be formulated for all thruster-subsystem components
  - lifetime
  - performance
  - reliability
  - operating ranges (temperature, power, etc.)
  - interface requirements (structural, thermal, etc.)
  - integration (safety, environment, etc.)
- A rationale must be devised for showing compliance with the design specifications
  - qualification tests
  - demonstration tests and analytical projections
- Thrust-subsystem components must be developed to meet the design specifications

A formal design specification comparable to the ones used for procuring chemical thrusters was not prepared as part of the development of the NASA/Hughes 30-cm-diameter, J-series mercury ion thruster. However, it has been developed to provide a nominal thrust of F = 130 mN at a nominal specific impulse of I_{sp} = 3000 sec, and with a nominal power input of P_{in} = 2.7 kW.[5-1] The design lifetime for this thruster is L = 15,000 hours. In most respects, the technology of the J-series thruster is very mature, and no fundamental problems remain to be solved if the thruster is used in the manner conceived during its development. There are some unresolved issues of lifetime and reliability that have been raised in endurance tests, and these must be resolved before the technology can be considered fully mature. Acceptability of the thruster technology would also be improved by reducing the complexity of the hardware and/or its operation, and by reducing fabrication costs. Specific tasks are identified below to address these issues.

5.1 DISCHARGE-CHAMBER EROSION

Erosion of critical thruster components by ion sputtering is the major life-limiting process identified in the endurance tests performed on 900-series[5-2] and J-series[5-3] 30-cm-diameter thrusters. A secondary effect of this wearout mode is the deposition of the sputtered material. This deposition represents a reliability risk because spalling of the deposits produces metallic flakes that can result in pre-wearout failures (insulators can be short-circuited or ion beamlets can be deflected enough to damage the accelerator grids). Consequently, the major technology issue for the J-series thruster is baffle and pole-piece erosion and subsequent deposition of material onto the cathode keeper and keeper support. Life-test results[5-3] indicate that flakes can form from deposition in this region after relatively short operating times which we estimate may precipitate failures after only 10,000 hours of operation. Potential solutions for this problem are:

- Identify operating conditions that reduce sputtering in the cathode pole-piece/baffle region
- Improve surface characteristics of deposition sites to inhibit spalling
- Modify magnetic circuit to eliminate the pole piece/ baffle.

5.2 INSULATOR MATERIALS

Another issue that is equally important is the specification of materials and design of insulators for the thruster wiring and mounting. In the J-series design, several types of insulating materials are specified; ceramic or vespel stand-off-type insulators and teflon-coated kapton wiring insulation. In the thermal environment of the Mission Profile Life Test,[5-4] several insulation failures occurred. Although the failure mechanisms

have not been uniquely determined, operation of the thruster in higher temperature environments than had been assumed in its design was undeniably a contributing factor in these failures. To have a mature design, the thermal environment must be specified and the ambient conditions obtained in normal thruster operation must be determined, so that insulator materials can be selected appropriate to the thermal environment. For the isolator insulators, the vaporizer-temperature characteristics must also be taken into consideration.

5.3 OPERATING PROCEDURE

The J-series thruster design was developed with the objective of continuous operation for long periods of time and with variable power levels (throttleable) in planetary exploration-type missions. It is more probable that near-term applications will require relatively short-term, cyclic operation at constant power levels for maintaining the orbits of large spacecraft. This type of operation places greater stress on cathode heaters and requires operating algorithms that optimize ON/OFF operation (as contrasted with variable-power operation). Consequently, thruster components must be modified to enable numerous (5000 or more) cyclic operations with fast (<15 minutes) start-up. This approach will also benefit from simplified control concepts and power-processing circuitry.

5.4 CATHODE HEATERS

Two types of cathode heaters have been used in the development of mercury ion thrusters. One type is constructed of coaxial conductors as shown in Figure 5-1. The center conductor is the heating element, and the outer sheath acts as the current return. Several combinations of materials have been used to fabricate these heaters, with the most successful combination being tantalum for both inner and outer conductors, and magnesium

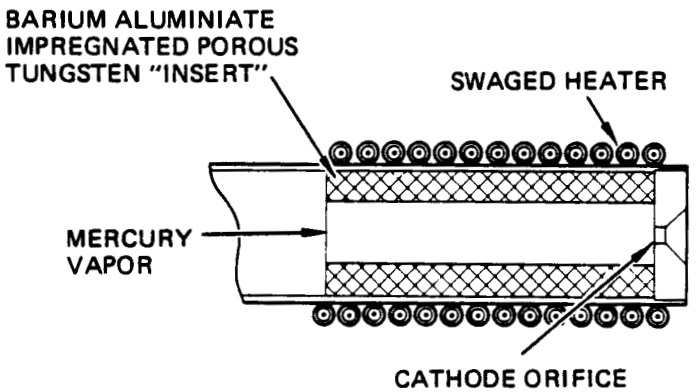

a. HOLLOW CATHODE WITH SWAGED-TYPE COAXIAL HEATER

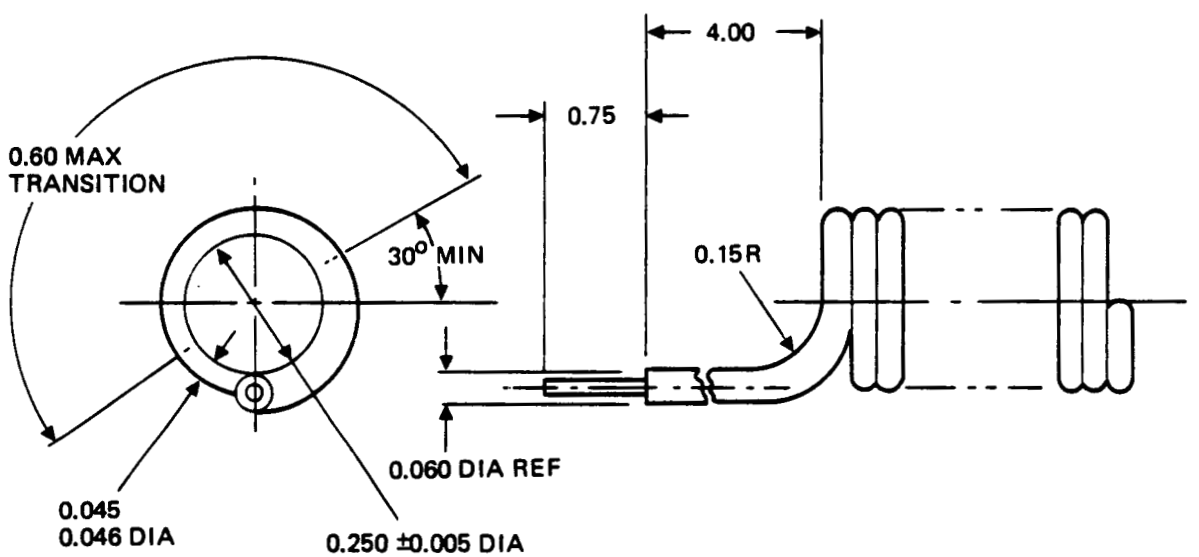

b. COAXIAL HEATER DESIGN

FIGURE 5-1. Swaged-type coaxial heater for 30-cm thruster cathodes.

oxide as the insulating material. The second type of heater is constructed by encapsulating the resistance-heating element in a ceramic insulator as shown in Figure 5-2. For this type of heater, the resistance-heating element has been fabricated using tungsten or tungsten/rhenium alloy, and the heating element has been encapsulated by flame spraying alumina.

For small-diameter cathodes (0.32 cm), the encapsulated heaters have proven to be tractable to fabrication. This type of heater provides better heat transfer from the heating element to the cathode tube, and, therefore, requires less power to achieve the required temperature. On the other hand, the coaxial heater material cannot be wrapped around small-diameter cathodes without excessive deformation that results in elongation and tearing of the outer conductor. The impaired integrity of the coaxial material caused by forming small-diameter coils has produced relatively short heater lifetimes.

Use of alumina-encapsulated heaters for larger diameter cathodes (0.64 cm or greater) is not tractable because the encapsulation tends to crack at normal cathode operating temperatures. Cracks in the encapsulation result in degraded heat transfer from the heating element to the cathode tube, requiring a higher operating temperature for the heating element and resulting in local "hot spots". These hot spots ultimately result in failure of the heater element.

Either of the cathode-heater designs decribed above can provide long operating life with high reliability if the heater-fabrication processes are carefully controlled. In both cases, the required controls have been documented. However, the procedures used by the fabricator involve levels of skill and attention to detail that exceed those required for fabrication of most comparable commercial products. Consequently, the successful procurement of high-reliability cathode heaters will require development of a vendor (or vendors) that can implement the quality procedures for fabricating reliable heaters.

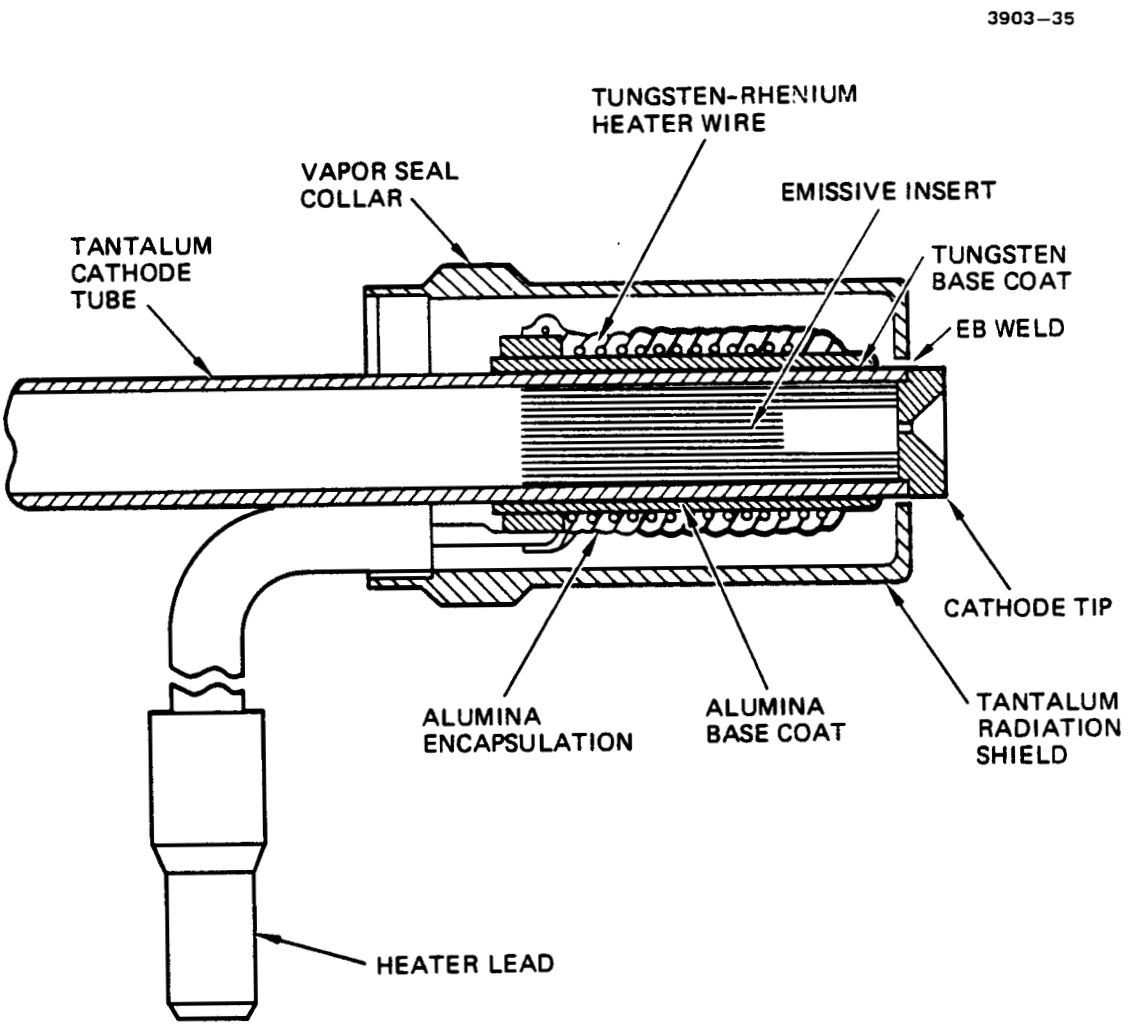

FIGURE 5-2. Encapsulated heater for 8-cm thruster cathodes.

Quality-control procedures for fabricating swaged, coaxial heaters were investigated by NASA-LeRC, and the results have been reported in the literature.[5-5] These procedures have been incorporated in the Hughes IPD's (Inspection and Process Documents) that are a part of the documentation for the LeRC/Hughes 30-cm-diameter, J-series mercury ion thruster. Some of these quality-control requirements are outlined here:

- The tantalum tubing for the outer conductor and the tantalum wire for the heater element must meet specifications on purity and ductility (hardness)
- The tantalum wire for the heater element must be uniform and free from nicks and fractures
- The magnesium-oxide insulator material must meet specifications on purity and moisture content
- The environment for swaging of the heater must be controlled to prevent contamination of the heater materials by any organic or oxidizing materials
- Compaction of the insulator in the swaged heater material must meet a specification on density
- Welding of the inner conductor to the outer conductor must be performed in a manner that will not embrittle the materials at the joint (electron-beam or controlled-atmosphere TIG weld)
- Before coiling the heater, the swaged assembly must pass inspection by both infra-red scan and x-ray to identify any defects in the insulator (voids) or the weld (cracks or excessive melting)
- After the heater is coiled it must pass an operational test of 100 ON-OFF cycles with a resistance change of less than a specified amount.

Thrusters fabricated with heaters made using these quality controls have been tested for many thousands of hours without a heater failure.

Heaters that were purchased for use in technology programs without specifying these controls have had relatively high failure rates. Several of these failed heaters have been

examined to ascertain the cause of failure. In all of the heaters examined, the failure was found to be a consequence of a void in the insulator material. Figure 5-3 shows an example of this type of failure which resulted in the heater element failing as an open circuit. In other failures of this type, the heater element contacted the outer conductor to cause a short circuit. In all of the heaters examined, the insulator void occurred near the transition in the diameter of the coaxial heater material (provided by design to furnish a low-resistance "lead" for the heater element). While this type of defect would have been detected by the quality-control procedures described above, the cost of these quality-control measures increases the cost of a swaged cathode heater by about a factor of ten.

In a flight-hardware fabrication program, the cost of fabricating high-reliability cathode heaters would not be a major consideration since the cost of a cathode heater represents less than 1% of the total thruster cost. The major consideration in obtaining high-reliability cathode heaters is one of logistics rather than technology. Whereas most of the other thruster materials or components are readily available from manufacturers of commercial products, we anticipate that appreciable time may be required to cultivate a vendor (or vendors) for the heater materials and the fabrication of swaged heaters. While several manufacturers have the potential for fabricating high-reliability heaters of this type, it has been, and will probably continue to be, extremely difficult to obtain full vendor cooperation in establishing the rigorous quality-control procedures required in view of the relatively small quantity of heaters that will be purchased (i.e., hundreds, not thousands). Nevertheless, this is considered to be the most certain means of obtaining high-reliability, long-life cathode heaters for large-diameter cathodes.

14629-2

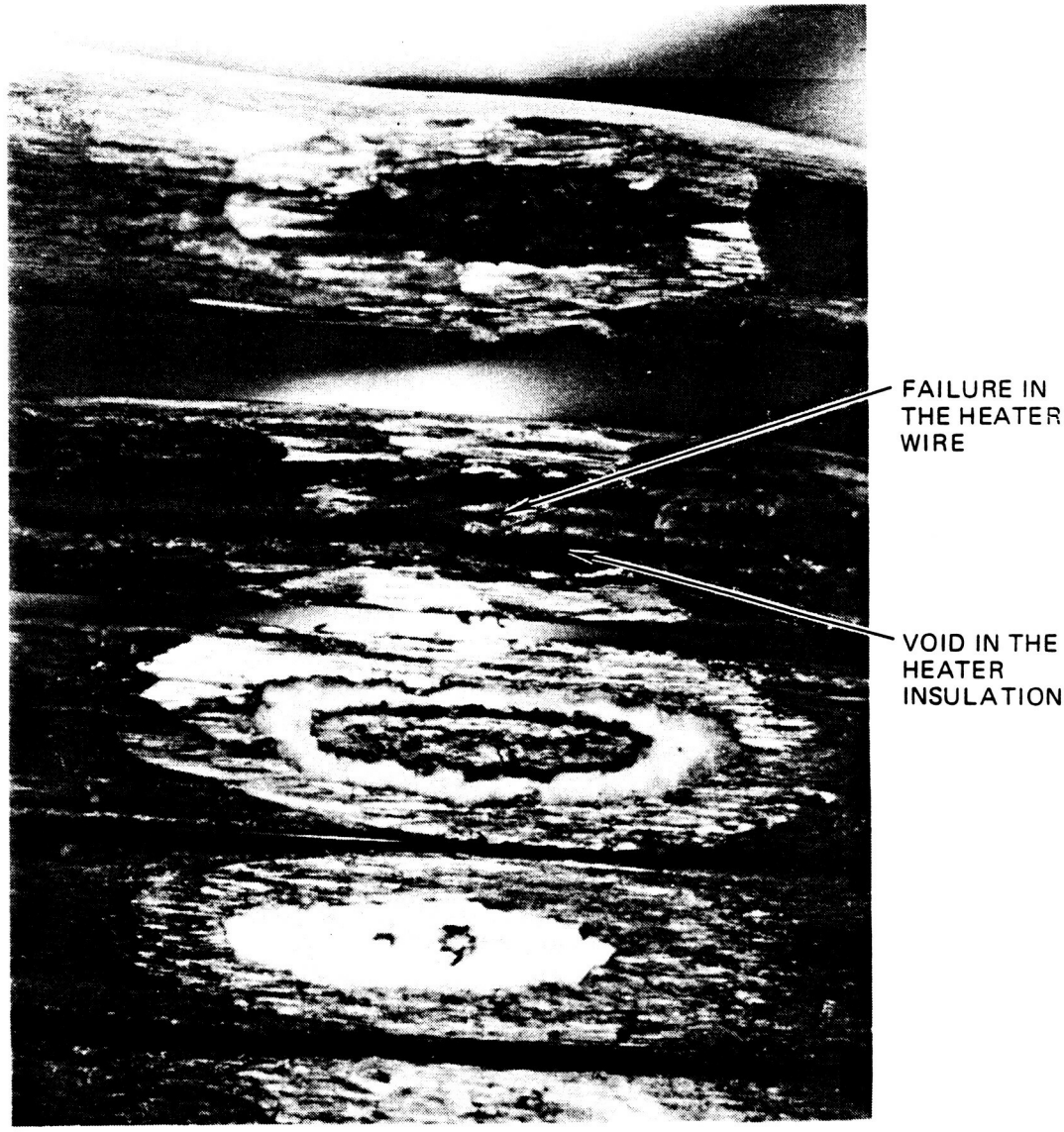

FIGURE 5-3. Example of a failure that is typical in heaters fabricated without rigid quality control.

The encapsulated heaters used on the smaller diameter cathodes are fabricated using similar rigorous quality controls to ensure long life and high reliability. Again, the purity of materials is an essential feature, but skill (craftsmanship) in application of the flame-sprayed alumina to the cathode tube, and then in covering the heater element, is the most critical operation in achieving successful fabrication of encapsulated heaters. The attachment of the heater wire to the cathode tube and to the center conductor of the coaxial lead-in by electron-beam welding is also a critical operation. However, this operation is more readily documented and can become nearly an automatic one.

5.5 ION-OPTICS FABRICATION

A final consideration relates to identifying and specifying steps or procedures performed during the fabrication of ion-optics grids to ensure stable, reproducible operation for the ion-extraction assembly. Examination of grid sets fabricated for J-series thrusters S/N J-2 thru J-10 revealed that the hole patterns of some grids are distorted sufficiently to influence the effective perveance. Tests at NASA's LeRC showed that several hours of continuous operation are required to obtain thermal (and dimensional) equilibrium of the ion-extraction assembly. This type of time constant could result in problems caused by aperture misalignment and out-of-tolerance interelectrode spacing for short-term, cyclic operation. Modifications in grid-fabrication procedures have been proposed to correct the problems described above; however, the effectiveness of these procedures has not been fully evaluated. Experiments to verify the relevance of improved grid-fabrication procedures to J-series mercury-ion-thruster designs must be performed.

Although the J-series ion-extraction-assembly design has proven to be superior, by far, to prior designs, some advances in fabrication and assembly procedures need to be documented to

ensure that future use of this design will produce favorable results. In addition to the procedures already described in the J-series, 30-cm mercury-ion-thruster documentation package, the following list of notes and procedures must be included to obtain reproducible results.

5.5.1 Molybdenum Material Specifications

In the documentation for fabrication of the J-series ion-extraction grids, the material is specified as low-carbon, arc-cast molybdenum. Molybdenum sheet is available in several other forms that vary in purity and ductility, and for which both the cost and delivery time is different. The material properties considered to be necessary for achieving success in hydroforming the ion-extraction grids are low carbon content, and high ductility (small grain size). Table 5-1 compares these properties in a qualitative manner for the available molybdenum types. Each type can be formed without difficulty to the curvature required for the J-series thruster two-grid ion-extraction-assembly design. Extension of the technology to three grids, as required for operation at lower specific impulse (increased thrust-to-power ratio), requires a greater elongation of the material in the decel grid and the properties of the material are more critical. The types of molybdenum listed as "arc-cast" and "standard pressed-and-sintered" in Table 5-1 are not sufficiently ductile to enable the grids to be formed in a manner that minimizes differential stretching between the grids (the forming-fixture configuration is shown in Figure 5-4) without fracture of the decel grid at the point of sharpest curvature.

5.5.2 Application of the Photoresist Pattern

It has been found that the dimensions of the apertures and the aperture patterns of the photoresist applied to the grids by the vendor that performs the chemical milling service may vary from the specifications on a given order, even though the

TABLE 5-1. Available Forms of Molybdenum Sheet

TYPE	CARBON CONTENT	DUCTILITY
arc-cast	< 300 ppm	least
standard pressed-and-sintered	< 50 ppm	moderate
pressed-and-sintered, extra annealed	< 50 ppm	good
low-carbon, arc-cast	< 50 ppm	best

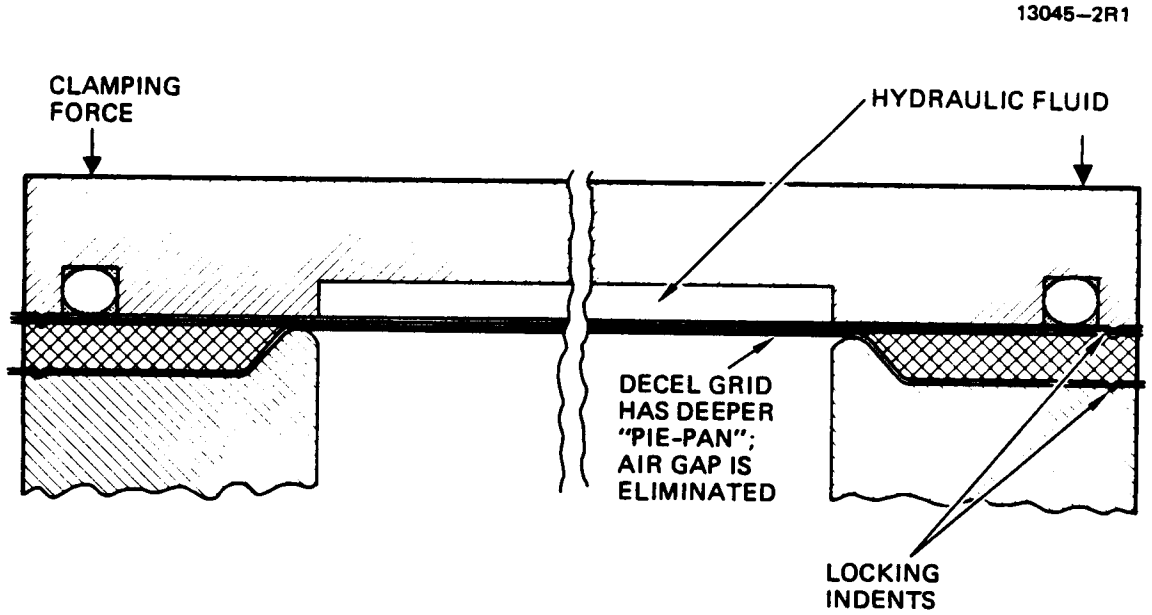

FIGURE 5-4. Modified hydroforming fixcture for three-grid ion optics.

aperture pattern has been provided before in accordance with the specification. Consequently, a detailed inspection of at least one set of grids is recommended before the grids are hydroformed. Specification of the aperture and aperture-pattern dimensions to four significant figures has produced excellent pattern reproducibility.

5.5.3 Electrode Clamping in the Hydroforming Fixture

The fixtures used for hydroforming the grids must provide a means for positively clamping the edges of the grid material. In this manner, there is no possibility that the material could slip during the hydroforming process and permit the hole pattern to become distorted (see Figure 5-4).

5.5.4 Stress Annealing

Ion-extraction grids that are hydroformed using fixtures like the one shown in Figure 5-4 must be stress annealed to relieve the residual stress present at the transition between the spherical and planar surfaces. For the fabrication of the J-series ion-extraction grids, stress-annealing fixtures were designed that tightly hold the hydroformed grids in the desired configuration while they are subjected to annealing temperatures. These annealing fixtures were made of carpenter steel, which has a coefficient of thermal expansion that is sufficiently different from that of molybdenum to cause distortion of the grids by differential expansion if the grids are tightly held by the fixture (no slippage). By providing graphite liners for the stress-annealing fixture (see Figure 3-6) the grids can be tightly clamped so that the graphite liner maintains the spherical shape of the grid during stress annealing, but slips with respect to the differential expansion of the carpenter-steel support. The differential expansion between the graphite and the molybdenum is tolerable at the annealing temperature of 1000°C (measured on the outside of the stress-relieving fixture).

REFERENCES

5-1. Lovell, R.R., et al, "30-Centimeter Ion Thrust Subsystem Design Manual," NASA TM-79191, NASA Lewis Research Center, Cleveland, Ohio, June 1975.

5-2. Collett, C.R. and Bechtel, R.T., "An Endurance Test of a 900 Series 30-cm Engineering Model Thruster," AIAA Paper No. 76-1020, Key Biscayne, Florida, November 1976.

5-3. Bechtel, R.T., Trump, G.E., and James, E.L., "Results of the Mission Profile Life Test," AIAA Paper No. 82-1905, New Orleans, Louisiana, November 1982.

5-4. Trump, G.E., et al, "An Electric Propulsion Long Term Test Facility," AIAA Paper No. 79-2080, Princeton, New Jersey, October 1979.

5-5. Mueller, L.A., "High Reliability Cathode Heaters for Ion Thrusters," AIAA Paper No. 76-1071, Key Biscayne, Florida, November 1976.

SECTION 6

ION-THRUSTER RELIABILITY

Marketing discussions with potential users of ion-propulsion technology invariably touch on the question of reliability; the designer wants to be assured that ion propulsion is at least as reliable as the chemical propulsion which it (typically) replaces. The current practice within Hughes Space and Communication Group is to require a qualification demonstration of at least 1.5 times the mission requirement. Consequently, even with the low-duty-cycle requirement that North-South stationkeeping of geosynchronous communications satellites imposes on a 30-cm-diameter mercury ion thruster, the qualification time is on the order of 10,000 hours. Therefore, in any preliminary planning effort the potential customer needs to be assured that lifetime is not an issue.

We reviewed over sixty references dealing with ion-thruster and component life tests and flight tests, with the objective of compiling data that could be used to demonstrate the reliability of ion-propulsion technology to potential users. In performing the literature survey, we evaluated three categories; thruster endurance tests, component endurance tests, and thruster flight tests. The list of references that were used in the compilation are tabulated at the end of this section. The list is indexed according to test type, component, and related thruster size; with the intent that new or additional test results could easily be added to the data base as they become available.

The compiled data include the accumulated number of operating hours and cycles, and the reasons for termination of testing. Table 6-1 summarizes the results, showing the number of life tests that have been conducted, the total number of operating hours, and the total number of ON-OFF cycles for each of the three categories. The results show an impressive number

TABLE 6-1. Summary of Accumulated Totals of Ion-Propulsion Lifetests

	Ground-Based Thruster Tests	Ground-Based Component Tests	Space Thruster Tests
Tests	28	20	3
Hours	113,300	192,200	2,700
Cycles	8,800	39,260	260

of tests and operating hours have been accumulated under various completed and on-going life tests of ion thrusters and critical components. For example, thruster life tests have accumulated over 113,000 hours, component life tests have accumulated over 192,000 hours, and flight tests have accumulated 2,700 hours.

The bar chart of Figure 6-1 tabulates thruster life tests that are either ongoing or have been completed without a component failure. The figure shows that the demonstrated lifetimes of the 8- and 30-cm-diameter thrusters are 15,000 and 10,000 hours, respectively. Figure 6-2 summarizes life tests that were terminated prematurely. The reasons for the test terminations vary, but in general they are attributed to problems that were not directly related to the failure of specific thruster components. For example, in the 5-cm-diameter thruster life test the ion-optics assembly developed a short resulting from the presence of a metal flake that had spalled from a surface within the discharge chamber. In subsequent revisions to the thruster design, the problem of metal-flake formation has been eliminated through appropriate selection and treatment of discharge-chamber components; such as covering critical surfaces with wire mesh, or cladding them with low-sputter-yield materials. The remaining causes of premature test terminations are attributed to failures that might have been avoided through the use of more-reliable vacuum facilities, or by improved thruster-assembly practices.

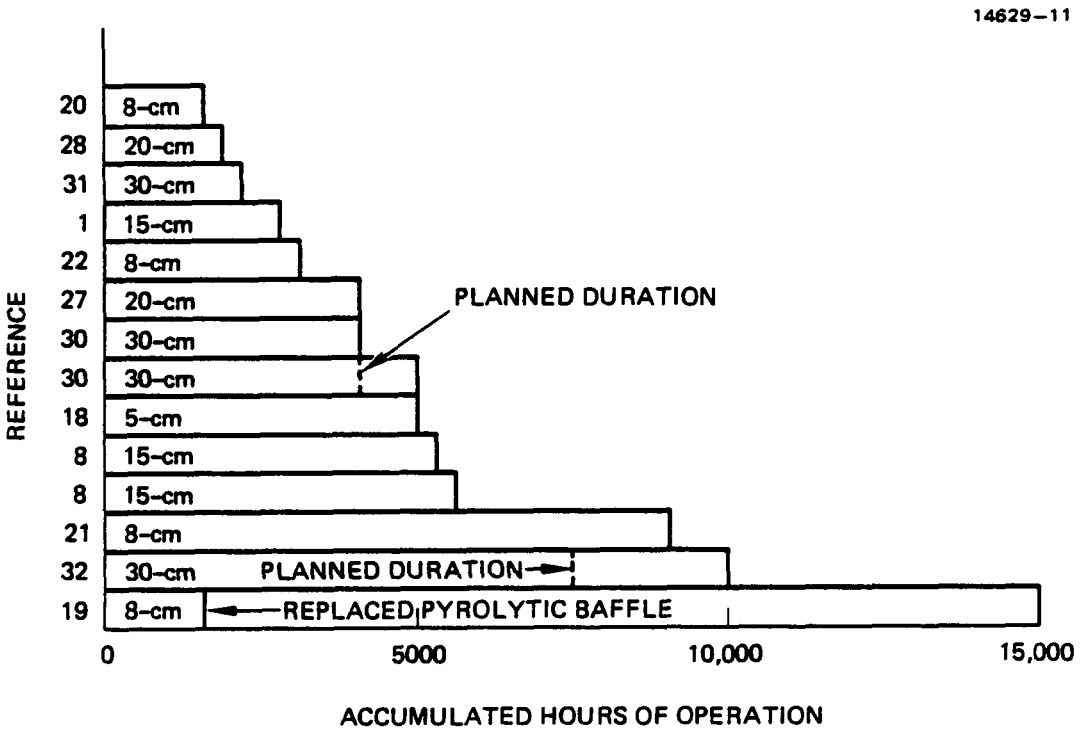

FIGURE 6-1. Ongoing or completed thruster life tests.

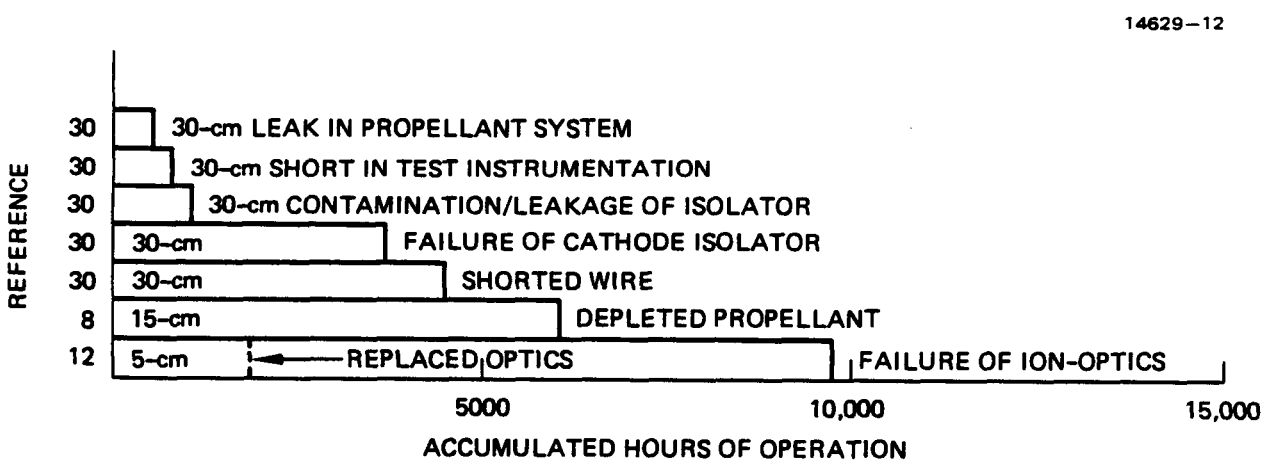

FIGURE 6-2. Thruster life tests that were terminated prematurely.

6.1 FLIGHT-TEST REFERENCES

1. Kerslake, W.R. and Ignaczak, L.R., "SERT II Extended Flight Thruster Experiments," AIAA 81-0665, April 1981.

2. Kerslake, W.R. and Ignaczak, L.R., "SERT II 1979 Extended Flight Thruster System Performance," AIAA 79-2063, October 1979.

3. Kerslake, W.R. and Ignaczak, L.R., "Status of SERT II Spacecraft and Ion Thrusters," NASA TM X-78827 and AIAA 78-622, April 1978.

4. Kerslake, W.R., "Status of SERT II Thrusters and Spacecraft - 1976," NASA TM X-73501 and AIAA 76-1601, November 1976.

5. Kerslake, W.R. and Finke, R.C., "SERT II Thruster Space Restart - 1974," NASA TM X-71651 and AIAA 75-365, March 1975.

6. Cohen, H.A. and Mullen, E.G., "The Sounding Rocket Flight of a Satellite Positive Ion Beam System," AIAA 79-2068, October 1979.

7. Cohen, H.A., Huber, W.B., and Masek, T., "Preparation, Integration and Initial Operations of SPIBS on the P78-2 Satellite," AIAA 79-2069, October 1979.

8. Kerslake, W.R., Goldman, R.G., and Nieberding, W.C., "SERT II: Mission Thruster Performance and In-Flight Thrust Measurements" J. Spacecraft and Rockets, Vol. 8, No. 3, March 1971, pp. 213-224.

9. Ignaczak, L.R., Stevens, N.J., and LeRoy, B.E., "Performance of the SERT II Spacecraft after 4 1/2 Years in Space," NASA TM X-71632, November 1974.

6.2 THRUSTER LIFE-TEST REFERENCES

6.2.1 5-cm-Diameter Thruster

10. Power, J.L., "Sputter Erosion and Deposition in the Discharge Chamber of a Small Mercury Ion Thruster," NASA TM X-71424 and AIAA 73-1109, October 1973.

11. Nakanishi, S. and Finke, R.C., "A 9700-Hour Durability Test of a Five-Centimeter Diameter Ion Thruster," NASA TM X-68284 and AIAA 73-1111, October 1973.

12. Nakanishi, S. and Finke, R.C., "A 9700-Hour Durability Test of a Five-Centimeter Diameter Ion Thruster," J. Spacecraft and Rockets, Vol. 11, No. 8, August 1974, pp.560-566.

13. Hyman, J., "Performance Optimized Small Structurally Integrated Ion Thruster System," NASA CR-121183, Hughes Research Laboratories, May 1973.

14. Lathem, W.C., "5000-Hour Test of a Grid-Translation Beam-Deflection System for a 5-cm Diameter Kaufman Thruster," NASA TM X-68185, January 1973.

15. Power, J.L., "Accelerated Life Test of Sputtering and Anode Deposit Spalling in a Small Mercury Ion Thruster," NASA TM X-3269, September 1975.

16. Nakanishi, S., "Durability Tests of a 5-cm-Diam Ion Thruster System," J. Spacecraft and Rockets, Vol. 11, No. 9, September 1974, pp. 669-671.

17. Nakanishi, S. "Durability Tests of a Five-Centimeter Diameter Ion Thruster System," NASA TM X-68132 and AIAA 72-1151, December 1972.

18. Nakanishi, S. and Finke, R.C., "A 2000-Hour Durability Test of a 5-cm Diameter Mercury Bombardment Ion Thruster," NASA TM X-68155, October 1972.

6.2.2. 8-cm-Diameter Thruster

19. Nakanishi, S., "A 15,000-Hour Cyclic Endurance Test of an 8-Centimeter-Diameter Electron Bombardment Mercury Ion Thruster," NASA TM X-73508 and AIAA 76-1022, November 1976.

20. Mantenieks, M.A. and Wintucky, E.G., "5200 Cycle Test of an 8-cm Diameter Hg Ion Thruster," NASA TM X-78860 and AIAA 78-649, April 1978.

21. Dulgeroff, C.R., Beattie, J.R., Poeschel, R.L., and Hyman, J., "IAPS (8-cm) Ion Thruster Cyclic Endurance Test," IEPC Paper No. 84-37, Tokyo, Japan, May 1984.

22. Rawlin, V.K., Private Communication, November, 1984.

6.2.3 15-cm-Diameter Thruster

23. Anon., "Development and Test of an Ion Engine System Employing Modular Power Conditioning," NASA CR-80515, Hughes Aircraft Company, August 1966.

24. Knauer, W., Poeschel, R.L., King, H.J., and Ward, J.W., "Discharge Chamber Studies for Mercury Bombardment Thrusters," NASA CR-72440, Hughes Research Laboratories, September 1968.

25. Rulis, R.J., "SERT II: Design Requirements for Integrating Electric Propulsion into Spacecraft," J. Spacecraft and Rockets, Vol. 8, No. 3, March 1971, pp. 209-213.

26. Rawlin, V.K. and Kerslake, W.R., "Durability of the SERT II Hollow Cathode and Future Applications of Hollow Cathodes," AIAA 69-304, March 1969.

6.2.4 20-cm-Diameter Thruster

27. King, H.J., Eckhardt, W.O., Ward, J.W., and Knecthli, R.C., "Electron Bombardment Thrusters Using Liquid Mercury Cathodes," J. Spacecraft and Rockets, Vol. 4, No. 5, May 1967, pp. 599-602.

28. Masek, T.D., "SEP Thrust Subsystem Development," JPL TR 32-1579, March 1973.

6.2.5 30-cm-Diameter Thruster

29. James, E.L. and Bechtel, R.T., "Results of the Mission Profile Life Test First Test Segment: Thruster J1," AIAA 81-0716, April 1981.

30. Bechtel, R.T., Trump, G.E., and James, E.L., "Results of the Mission Profile Life Test," AIAA 82-1905, November 1982.

31. Mantenieks, M.A. and Rawlin, V.K., "Sputtering Phenomena of Discharge Chamber Components in a 30-cm Diameter Hg Ion Thruster," NASA TM X-73533 and AIAA 76-988, November 1976.

32. Collett, C.R. and Poeschel, R.L., "A 10,000-Hour Endurance Test of a 700 Series 30-cm Engineering Model Thruster," AIAA 76-1019, November 1976.

33. Collett, C.R. and Bechtel, R.T., "An Endurance Test of a 900 Series 30-cm Engineering Model Ion Thruster," AIAA 76-1020, November 1976.

34. Collett, C.R., "A 7700 Hour Endurance Test of a 30-cm Kaufman Thruster," AIAA 75-366, March 1975.

35. Mantenieks, M.A. and Rawlin, V.K., "Studies of Internal Sputtering in a 30-cm Ion Thruster," NASA TM X-71654 and AIAA 75-400, March 1975.

36. Collett, C.R., "Endurance Testing of a 30-cm Kaufman Thruster," AIAA 73-1085, October 1973.

37. Bechtel, R.T. and James, E.L., "Preliminary Results of the Mission Profile Life Test," AIAA 79-2078, October 1979.

38. King, H.J. and Poeschel, R.L., "A 30-cm Mercury Ion Thruster," J. Spacecraft and Rockets, Vol. 8, No. 4, April 1971, pp. 420-423.

39. King, H.J. and Poeschel, R.L., "An Ion Thruster Module for Primary Propulsion Systems," J. of British Interplanetary Society, Vol. 26, 1973, pp. 203-219.

40. Bechtel, R.T. and Dulgeroff, C.R., "J Series Thruster Thermal Test Results," AIAA 82-1906, November 1982.

6.3 COMPONENT LIFE-TEST REFERENCES

6.3.1 5-cm-Diameter Thruster

41. Wintucky, E.G., "A 20,000-Hour Endurance Test of a Structurally and Thermally Integrated 5-cm Diameter Ion Thruster Main Cathode," NASA TM X-71600 and AIAA 75-368, March 1975.

42. Lathem, W.C., "1000-Hour Test of a Dual Grid, Electrostatic Beam Deflection System on a 5-Centimeter-Diameter Kaufman Thruster, NASA TM X-67907, August 1971.

43. Lathem, W.C., "A Single-Axis Electrostatic Beam Deflection System for a 5-cm Diameter Ion Thruster," NASA TM X-68133, September 1972.

44. Hudson, W.R. and Weigland, A.J., "Hollow Cathodes with BaO Impreganted, Porous Tungsten Inserts and Tips," NASA TM X-71417 and AIAA 73-1142, October 1973.

45. Wintucky, E.G., "High Voltage Pulse Ignition of Mercury Discharge Hollow Cathodes," NASA TM X-71425 and AIAA 73-1140, October 1973.

46. Zuccaro, D., "Mercury Vapor Hollow Cathode Component Studies," AIAA 73-1141, October 1973.

47. Weigand, A.J., "5-cm Diameter Ion Thruster Development Program Summary," NASA TM X-68110, July 1972.

6.3.2 8-cm-Diameter Thruster

48. Wintucky, E.G., "Cycle Life Testing of 8-cm Mercury Ion Thruster Cathodes," NASA TM X-73526 and AIAA 76-986, November 1976.

49. Williamson, W.S., Dulgeroff, C.R., and Williams, R.L., "8-cm Engineering Model Thruster Technology; A Review of Recent Developments," AIAA 79-2103, October 1979.

50. Williamson, W.S., Private Communication, April 1983.

51. Power, J.L. and Hiznay, D.J., "Solutions for Discharge Chamber Sputtering and Anode Deposit Spalling in Small Mercury Ion Thrusters," NASA TM X-71675 and AIAA 75-399, March 1975.

6.3.3 15-cm-Diameter Thruster

52. Rawlin, V.K., "A 13,000-Hour Test of a Mercury Hollow Cathode," NASA TM X-2785, June 1973.

6.3.4 30-cm-Diameter Thruster

53. Mirtich, M.J. and Kerslake, W.R., "Long Lifetime Hollow Cathodes for 30-cm Mercury Ion Thrusters," NASA TM X-73523 and AIAA 76-985, November 1976.

54. Mueller, L.A., "High Reliability Cathode Heaters for Ion Thrusters," NASA TM X-73538 and AIAA 76-1071, November 1976.

55. Mirtich, M.J., "Investigation of Hollow Cathode Performance for 30-cm Thrusters," AIAA 73-1138, October 1973.

56. Mantenieks, M.A., "Investigations of Mercury Isolators," AIAA 73-1088, October 1973.

57. Rawlin, V.K., "Studies of Dished Accelerator Grids for 30-cm Ion Thrusters," AIAA 73-1085, October 1973.

58. Campbell, J.W., Bechtel, R.T., and Brophy, J., "J Series Thruster Isolator Failure Analysis," AIAA 82-1907, November 1982.

6.4 LIFETEST BIBLIOGRAPHY

59. Krulle, G., Zeyfang, E., and Birner, W., "Recent Tests Performed for the Design Verification of RIT-10 Engineering Models," AIAA 79-2102, October 1979.

60. Pinks, W. and Krulle, G., "Performance Mapping and Lifetime Investigations of Thruster Components with Reference to the Development of a RIT-10 Flight-Prototype," AIAA 79-2115, October 1979.

61. Mantenieks, M.A., "Mercury Ion Thruster Component Testing," AIAA 79-2116, October 1979.

62. Bassner, H.F. and Klein, W.U., "Orbit Control of the German TV-Satellite by the RITA-Subsystem," AIAA 81-0663, April 1981.

63. Hudson, W. and Vondra, R.J., "Electric Propulsion Research and Technology in the U.S.," AIAA 82-1867, November 1982.

64. Nakamura, Y., "Electric Propulsion Programs in Japan," AIAA 82-1868, November 1982.

SECTION 7
CONCLUSIONS

Significant progress in advancing the understanding of mercury-ion-thruster systems and technology has been achieved under this program. Major accomplishments include the following key results:

- Major simplification and weight reduction of the ring-cusp discharge chamber.
- Improved performance of the optimized ring-cusp configuration; the baseline beam-ion-production cost of the optimized configuration was reduced to $\epsilon_i \simeq 130$ eV/ion. At a discharge propellant-utilization efficiency of 95%, the beam-ion-production cost was reduced to about 155 eV/ion, representing a reduction of about 40 eV/ion over the corresponding value for the J-series thruster.
- Comprehensive Langmuir-probe surveys were conducted in the J-series thruster for the first time.
- Development of a volume-averaging scheme to analyze Langmuir probe data provided valuable insight into identifying the dominant plasma processes prevailing in the ring-cusp and J-series thrusters. Good correlation of the average Maxwellian-electron temperature with thruster performance was achieved. The outstanding performance characteristics of the ring-cusp thruster were correlated with a higher Maxwellian-electron temperature than that which exists in the J-series thruster.
- The technology of fabricating ion-extraction electrodes was advanced by improving materials-selection criteria, hydroforming and stress-relieving tooling, and fabrication procedures.
- An assessment of the technology readiness of the J-series thruster was completed; the major remaining technology issue is the baffle and pole-piece erosion with subsequent deposition of material onto the cathode keeper and its supporting structure.
- A simplified power processor was used to successfully operate an 8-cm thruster that is functionally equivalent to the Ion Auxiliary Propulsion System (IAPS) thrusters.

APPENDIX A

VACUUM TEST FACILITY

Testing under this contract was performed in the 3-m-diameter vacuum chamber illustrated in Figure A-1. This chamber is pumped by a combination of two liquid-helium cryopumps, an oil-diffusion pump, and a liquid-nitrogen-cooled cryoliner; its ultimate pressure is less than 5×10^{-6} Pa (4×10^{-8} Torr). During thruster testing with mercury propellant, only the diffusion pump and the cryoliner are used. Testing with inert gases such as xenon is accomplished using the cryopumps and the cryoliner, with the diffusion pump isolated from the vacuum chamber using a pneumatic gate valve. The facility pumping speed for xenon is about 50,000 1/s.

A graphite-covered disc located about 5 m from the thruster exit plane is used to collect the thrust beam. Water cooling of this collector allows absorption of over 10 kW of beam power, and the graphite coating minimizes backsputtering.

The vacuum chamber is equipped with a wide variety of diagnostic equipment. A quadrupole residual gas analyzer is used to monitor vacuum-chamber impurities, and an optical monochromator is used to monitor line intensities of excited atoms produced in the discharge chamber. An ExB probe is used to measure the singly and doubly charged fraction of beam ions and to measure off-axis thrust loss. Other diagnostic equipment includes near- and far-field Faraday probes for measuring the current density profile in the ion beam and for measuring beam-divergence angles. Discharge-chamber plasma properties are obtained using a computer-controlled Langmuir probe and data-acquisition system.

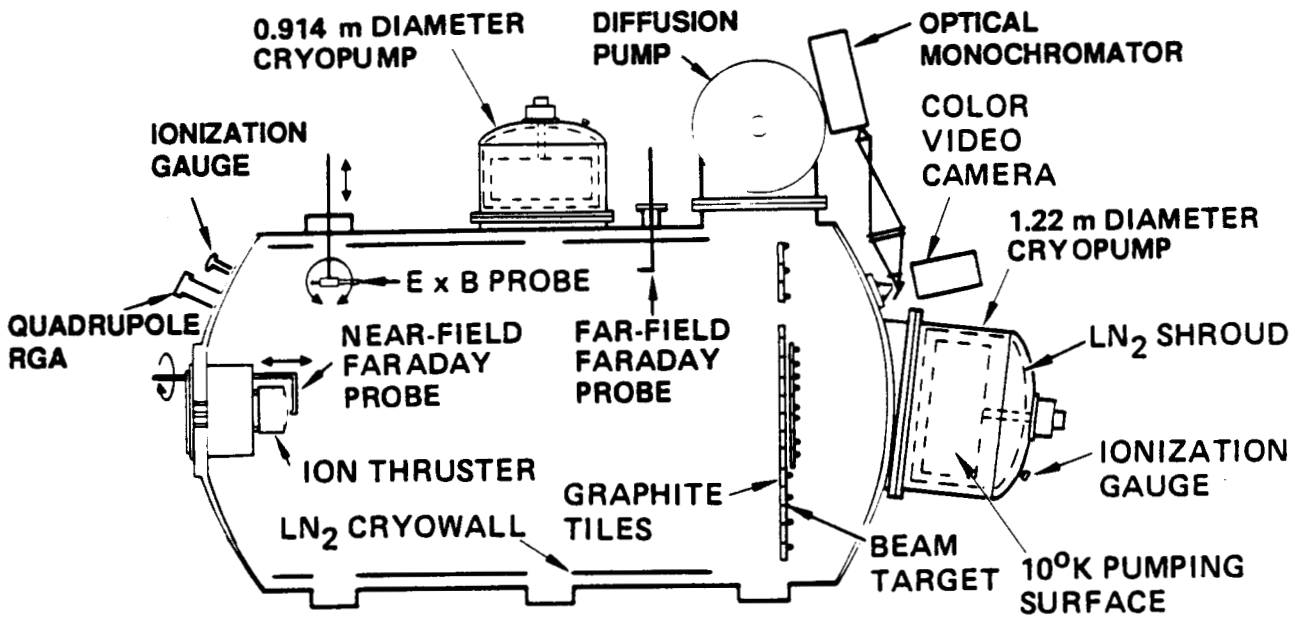

FIGURE A-1. Schematic of 3-m-diameter vacuum test facility.

Thruster performance is calculated using measured electrical parameters, flow rates, and the correction factors derived from ExB probe measurements. Equations used in the performance calculations and definitions of the thruster electrical parameters are presented in a previous publication.[A-1]

REFERENCES

A-1. Beattie, J.R., "Extended Performance Technology Study - 30-cm Thruster", NASA CR-168259, Hughes Research Laboratories, Malibu, California, June 1983.

APPENDIX B

RING-CUSP THRUSTER OPTIMIZATION

The final ring-cusp thruster configuration, whose performance and operating characteristics were described in Section 2, evolved as a result of a systematic investigation aimed at simplifying the original Sovey design, while at the same time maintaining its high level of performance. Figure B-1 summarizes the different thruster configurations that were evaluated. A descriptive summary of each design modification is presented in the sections below. For clarity, Table B-1 lists the various thruster configurations and the baseline beam-ion-production cost measured for each configuration.

B.1 CONFIGURATION NO. 1

This configuration is similar to the original argon-thruster design of Sovey, with the exception that the discharge chamber was scaled in length from 24 cm to 20 cm to compensate for the higher atomic mass (longer residence time) of mercury atoms.

B.2 CONFIGURATION NO. 2

This initial modification to the original ring-cusp thruster (Configuration No. 1) involved the removal of the cathode pole piece and cathode magnet ring. A comparison of the magnetic field with and without the cathode-magnet assembly indicated its effectiveness in "pushing" the magnetic-field contour lines downstream toward the ion-extraction assembly and producing a gradient in the magnetic field near the cathode orifice.

Thruster operation with the cathode-magnet assembly removed resulted in no observed damage to the "unprotected" cathode, however the performance was poorer than that achieved with Configuration No. 1. The cause of the performance loss was

14860-41

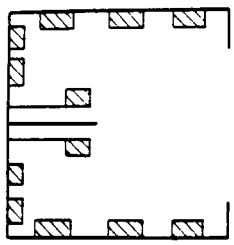

CONFIGURATION NO. 1

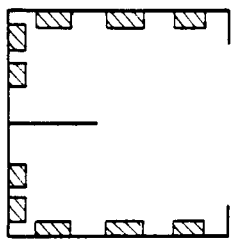

CONFIGURATION NO. 2

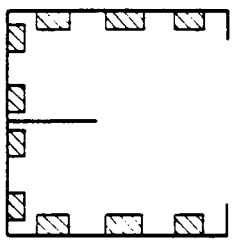

CONFIGURATION NO. 3

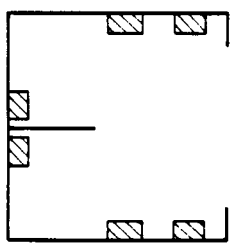

CONFIGURATION NO. 4

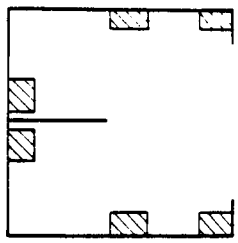

CONFIGURATION NO. 5

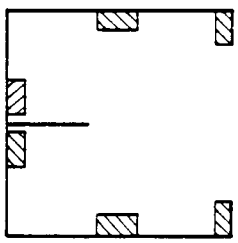

CONFIGURATION NO. 6

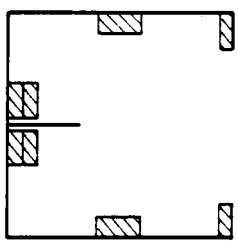

CONFIGURATION NO. 7

FIGURE B-1. Summary of different thruster configurations evaluated.

TABLE B-1. Tabulation of Baseline Beam-Ion-Production Cost for Different Thruster Configurations.

THRUSTER CONFIGURATION NO.	BASELINE BEAM-ION-PRODUCTION COST ε_i (eV/ion)
1	140
2	153
3	138
4	140
5	145
6	134
7	130

attributed to increased ion loss to the endwall. This speculation was supported by the observation that the net-electron current collected by the inner ring of magnets on the endwall increased by a factor of 50 with the cathode-magnet assembly removed.

B.3 CONFIGURATION NO. 3

In this configuration, the inner ring of magnets located on the endwall surface of the discharge chamber was rearranged to produce a higher axial magnetic field. The inner ring of magnets was reconfigured to a smaller-diameter ring surrounding the cathode. Magnetic-field measurements showed that this magnet configuration increased the axial magnetic field to a value that approached that obtained with the cathode-magnet assembly, but without the relatively large cathode-potential surface and mass associated with the original magnet assembly.

Thruster performance was improved relative to the previous configuration, verifying that with the cathode-magnet assembly removed a performance gain could be achieved with a reduced-mass configuration by simple rearrangemenet of the endwall magnets.

B.4 CONFIGURATION NO. 4

The two corner-magnet rings were removed in this configuration, giving rise to an additional simplification and mass savings. Previous thruster measurements indicated that the location of the ion-production region was downstream of the cathode, toward the ion-extraction assembly. On the basis of this result, the two corner-magnet rings were removed.

Thruster performance was essentially unchanged from the previous configuration, verifying that the two corner-magnet rings were sufficiently far removed from the ion-production region to have an influence.

B.5 CONFIGURATION NO. 5

In this configuration, the position of the downstream magnet ring was changed so that it was located next to the anode pole piece. The intent was to confine the magnetic field closer to the chamber boundary in the region near the ion-extraction assembly. Magnetic-field measurements within the discharge chamber indicated a weaker field strength near the screen electrode, and there was a significant degradation in thruster performance compared to the previous configuration. Electrode-current measurements indicated that the performance degradation was due to a net-ion loss to the sidewall/endwall (most likely the pole piece) surface.

B.6 CONFIGURATION NO. 6

The downstream magnet ring was rotated by 90°. In light of the previous result of degraded thruster performance, it was speculated that magnetically shielding the anode pole piece with a "rotated" magnet ring might reduce the net-ion loss to the

anode pole piece if this was the cause of the performance loss in the previous configuration. Magnetic-field measurements indicated improved field confinement near the pole piece.

There was a significant improvement in both thruster performance and beam-profile uniformity. Electrode-current measurements indicated a very small net-ion loss to the sidewall/endwall surface.

B.7 CONFIGURATION NO. 7

A second layer of magnets was added to the endwall-magnet ring. The intent was to "push" the ion-production region further downstream toward the ion-extraction assembly, thereby improving thruster performance. Measurements of the magnetic-field distribution indicated that the magnetic-field contour lines were located further downstream. In addition, the contour lines were better confined along the chamber boundary. Thruster performance and beam uniformity were improved.

The optimum position of the midstream magnet ring, and the minimum wall thickness required for optimum thruster performance, were studied under a related program[B-1].

REFERENCES

B-1. Beattie, J.R., and Matossian, J.N., "Inert Gas Thruster Technology", Final Report NAS 3-23860, Hughes Research Laboratories, Malibu, California.

APPENDIX C

HYBRID THRUSTER

One of the goals of this program was to improve the understanding of mercury-ion-thruster systems with consideration toward improving the technology and reliability of the state-of-the-art J-series thruster. The cathode-lifetime results obtained for the ring-cusp thruster (cf. Section 2) were promising and suggested that a potential solution to the erosion and deposition problem that exists in the cathode-pole-piece enclosure of the J-series thruster might be to eliminate this structure altogether. Therefore, we explored the feasibility of incorporating the attributes of the ring-cusp design into the J-series thruster.

Thruster S/N 301-J, which is electrically equivalent to a J-series thruster, was modified to produce a hybrid ring-cusp configuration by removing the conventional cathode pole piece and baffle, and by installing a single ring of $SmCo_5$ magnets around the sidewall and a double ring of $SmCo_5$ magnets around the cathode on the endwall. The resulting configuration is shown in Figure C-1. For comparison, the J-series chamber configuration is also shown. Magnetic-field measurements revealed that the resulting contour lines had the attributes of the ring-cusp design. In addition, the resultant configuration had approximately the same mass as the baseline J-series design.

However, thruster performance with this configuration was poor ($\epsilon_i \geq 350$ eV/ion). Figure C-2 presents an iron-filings map, showing that the field lines emanating from the cathode orifice intersect the screen grid near the center. This is believed to have the effect of confining the electrons emitted by the cathode to the central-core region of the discharge chamber, much like in early axial-field discharge chambers. The poor thruster performance is believed to be a result of electrons reaching the bulk of the discharge-chamber volume only as a result of energy-

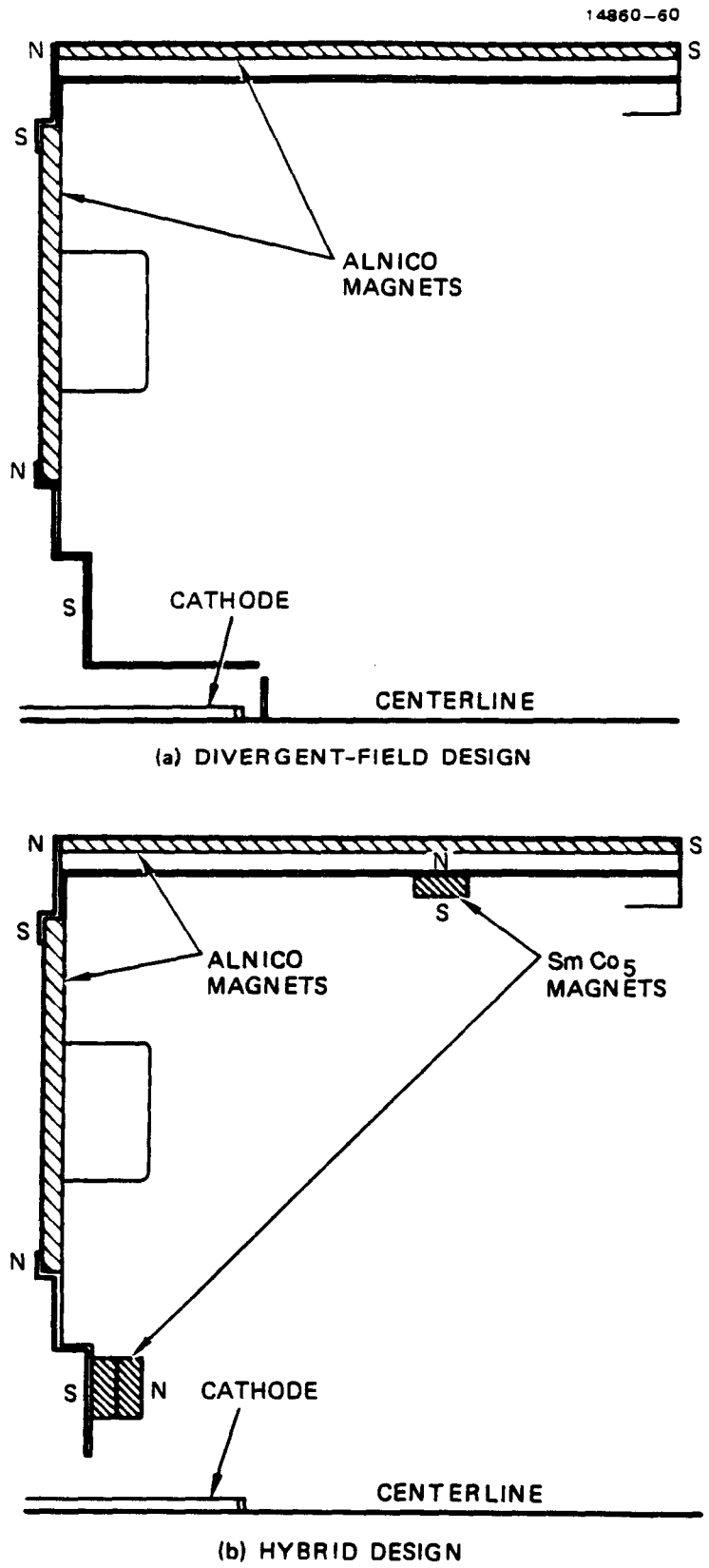

FIGURE C-1. Schematic of divergent-field and hybrid discharge chamber.

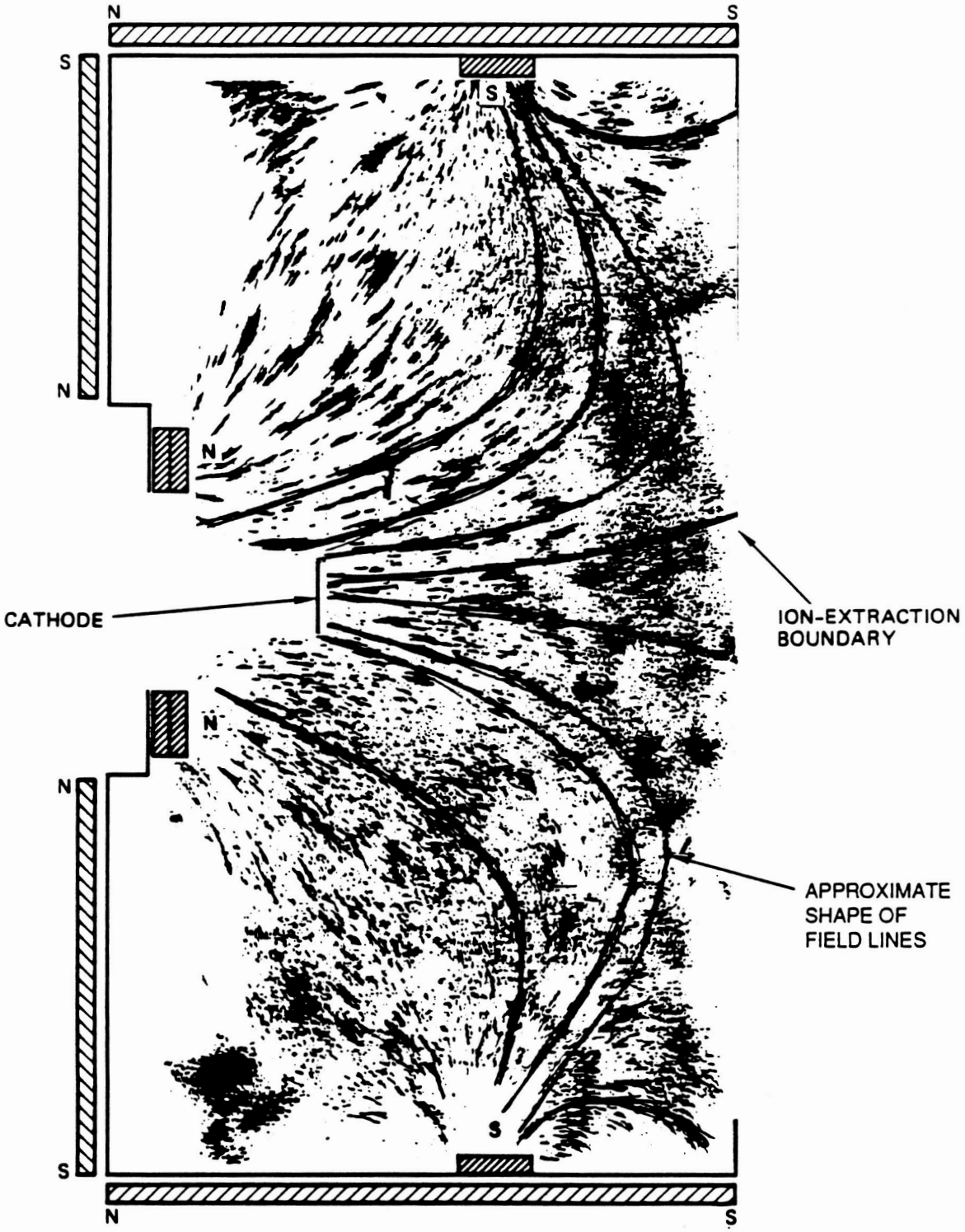

FIGURE C-2. Iron filings map of hybrid thruster discharge chamber.

depleting collisions. This argument is supported by the observation (that was made after the test) that the upstream side of the screen grid had a bright-appearing region that extended over the center part of the grid (a diameter of about 7 to 10 cm), suggesting the existence of an intense plasma in this region.

A Langmuir-probe survey revealed that the plasma in the hybrid thruster was characterized by low electron temperature and plasma potential. The results also indicated that the plasma was confined to the region near the chamber axis, confirming our speculation based on the iron-filings map and the appearance of the screen grid.

ATTACHMENT 1

DISTRIBUTION LIST

	Copies
National Aeronautics and Space Administration Washington, DC 20546 Attn:	1
RP/Mr. Earl E. VanLandingham, MS B600	1
RP/Mr. James R. Stone	1
National Aeronautics and Space Administration Lewis Research Center 21000 Brookpark Road Cleveland, OH 44135 Attn:	
Technology Utilization Office, MS 7-3	1
Report Control Office, MS 60-1	1
Library, MS 60-3	2
Dr. M. Goldstein, Chief Scientist, MS 5-9	1
Mr. David Byers, MS 500-219	1
Mr. Vince Rawlin, MS 500-219	82
Mr. Bruce Banks, MS 302-1	1
National Aeronautics and Space Administration Marshall Space Flight Center Huntsville, AL 35812 Attn:	
Mr. Robert Bechtel	1
Mr. Robert H. Champion	1
NASA Scientific and Technical Information Facility P.O. Box 8757 Baltimore, MD 21240 Attn:	
Accessioning Dept.	1
Dept. of the Navy Office of Naval Research University of New Mexico Bandolier Hall West Albuquerque, NM 87131 Attn:	
G. Max Irving	1
Research and Technology Division Wright Patterson AFB, OH 454331 Attn:	
(ADTN) Mr. Everett Bailey	1

	Copies
Procurement Executive, Ministry of Defense Royal Aircraft Establishment Farnborough, Hants GU14 6TD ENGLAND Attn:	
Dr. D. G. Fearn	1
United Kingdom Atomic Energy Authority Culham Laboratory Abingdon, Oxfordshire OX143DB ENGLAND Attn:	
Dr. P. J. Harbour	1
Dr. A. R. Martin (Rm F4/135)	1
Intelsat M.S. 33 3400 International Dr. N.W. Washington, D.C. 20008-3098 Attn:	
Mr. Rolland Schreib	1
Air Force Astronautics Lab Edwards AFB, CA 93523 Attn:	
LKDH/Lt. Robert D. Meya, MS 24	1
LKDH/Lt. Phil Roberts, MS 24	1
Mr. J. Chris Andrews, MS 24	1
Giessen University 1st Institute of Physics Giessen, West Germany Attn:	
Professor H. W. Loeb	1
Jet Propulsion Laboratory 4800 Oak Grove Laboratory Pasadena, CA 91102 Attn:	
Technical Library	1
Dr. Dave King	1
Mr. Bill Deininger	1
Mr. Charles Garner	1
TRW Inc. TRW Systems One Space Park Redondo Beach, CA 90278 Attn:	
Mr. Sid Zafran	1

	Copies
Scionics, Inc. 18801 Muncaster Rd. Derwood, MD 20855 Attn:	
Dr. Bernard Free	1
COMSAT Laboratories P. O. Box 115 Clarksburg, MD 20734 Attn:	
Technical Library	1
Electro-Optical Systems, Inc. 300 North Halstead Pasadena, CA 91107 Attn:	
Mr. E. James	1
Mr. W. Ramsey	1
National Aeronautics and Space Administration Goddard Space Flight Center Greenbelt, MD 20771 Attn:	
Dr. David H. Suddreth	1
National Aeronautics and Space Administration Ames Research Center Moffett Field, CA 94035 Attn:	
Technical Library	1
National Aeronautics and Space Administration Langley Research Center Langley Field Station Hampton, VA 23365 Attn:	
Technical Library	1
Hughes Research Laboratories 3011 Malibu Canyon Road Malibu, CA 90265 Attn:	
Dr. Jay Hyman, MS RL 57	1
Dr. J. R. Beattie, MS RL 57	1
Dr. J. N. Matossian, MS RL 57	1
Dr. W. S. Williamson MS RL 57	1

	Copies
Princeton University Princeton, NJ 08540 Attn:	
Dean R. G. Jahn	1
Dr. Arnold Kelly	1
Boeing Aerospace Co. P. O. Box 3999 Seattle, WA 98124 Attn:	
Mr. Donald Grim, MS 8K31	1
Lockheed Missiles and Space Co. Sunnyvale, CA 94088 Attn:	
Dr. William L. Owens Dept. 57-24	1
Rocket Research Co. P. O. Box 97009 Redmond, WA 98073-9709 Attn:	
Mr. William W. Smith	1
Mr. Paul Lichon	1
Rocket Research Co. York Center Redmond, WA 98052 Attn:	
Mr. R. J. Cassidy	1
Sandia Laboratories P. O. Box 5800 Albuquerque, NM 87185 Attn:	
Mr. Ralph R. Peters, Mail Code 4537	1
Mr. Dean Rovang, Mail Code 1251	1
Ion Tech Inc. 2330 E. Prospect Road Fort Collins, CO 80525 Attn:	
Dr. Dan Siegfried	1
Tuskegee Institute School of Engineering Tuskegee Institute, AL 36088 Attn:	
Dr. Pradosh Ray	1

	Copies
Mr. Lee Parker 252 Lexington Road Concord, MA 01741	1
Colorado State University Fort Collins, CO 80523 Attn:	
Dr. R. S. Robinson	1
Dr. P. J. Wilbur	1
OSD/SDIO/IST Pentagon 1E118 Washington, DC 20301-7100 Attn:	
Dr. Leonard H. Caveny	1
Sverdrup Technology 16530 Commerce Ct. Middleburg Heights, OH 44130 Attn:	
Mr. James Gilland	1
Michigan State University East Lansing, MI 48824 Attn:	
Dr. J. Asmussen	1
Dr. M. C. Hawley	1
The Aerospace Corporation Space Sciences Laboratory P. O. Box 92957 Los Angeles, CA 90009 Attn:	
Technical Library	1
Mr. Jay Penn	1
Dr. Kevin Rudolph M.S. S-8071 Martin Marietta Aerospace P. O. Box 179 Denver, CO 80201	1
Dr. Finkelstein Physics Department Georgia Institute of Technology Atlanta, GA 30332	1
Dr. Rod Burton G-T Devices, Inc. 5705 A General Washington Dr. Alexandria, VA 22312	1

	Copies
Mr. Curtis Haynes Teletronix Inc. MS 50-431 P. O. Box 500 Beaverton, OR 97077	1
W. J. Schaefer Assoc. Inc. 1901 North Fort Meyer Dr., Suite No. 800 Arlington, VA 22209 Attn:	
Dr. Herbert Cohen	1
Dr. Robert Vondra	1
Electric Propulsion Laboratory, Inc. St. Rt. 2, Box 3406A Tehachapi, CA 93561 Attn:	
Dr. Graeme Aston	1
Dr. John R. Brophy	1
Westinghouse R&D Center 1310 Beulah Rd. Pittsburgh, PA 15235 Attn:	
J. F. Perkins	1